Determination of Liquid Scintillator Purity for the Jiangmen Underground Neutrino Observatory

Paul Christian Hackspacher
Born in Arad, Romania

October 31, 2020

Dissertation Submitted for the Award of the Title
Doctor of Natural Sciences
to the Faculty of Physics, Mathematics and Computer Science

Johannes Gutenberg University Mainz

"This quote is often falsely attributed to Mark Twain."

MARK TWAIN

Abstract

The Jiangmen Underground Neutrino Observatory (JUNO) is a neutrino experiment currently under construction in southern China. Its primary goal is the determination of the neutrino mass ordering by a spectral analysis of the reactor neutrino flux from two nearby nuclear power plants at a distance of 53 km using a 20 kt liquid scintillator (LS) detector.

As the neutrinos are identified indirectly through measurement of scintillation light within the LS, it is imperative for the liquid to be as clean as possible and its properties sufficiently known. This thesis deals with both, optical and radioactive characteristics, and describes methods of determining scattering parameters and radioactive contamination of the LS.

The first part of the thesis investigates Rayleigh scattering in the LS by means of a laboratory setup that illuminates samples with polarized light of selectable wavelengths while two photomultiplier tubes (PMTs) measure both, the throughgoing intensity and the emissions at 90° perpendicular to the beam path. Comparing the two allows to identify the so-called Rayleigh length of the respective sample. Rayleigh scattering is the dominant process determining the transparency of the LS to the scintillation light. The setup was calibrated using various samples with known scattering behaviour before conducting LS investigations. The resulting Rayleigh lengths of $(26.1 \pm 1.2_{\text{stat}} \pm 2.6_{\text{sys}})$ m for a pure LAB sample and $(22.4 \pm 0.7_{\text{stat}} \pm 2.2_{\text{sys}})$ m for a sample of SHiP scintillator at 430 nm are in agreement with expectations around 28 m and show the anticipated λ^4-dependence in the region above, but deviate for lower wavelengths. This discrepancy was verified with a spectrometer and suggests either contamination of the samples in question, divergent behaviour in proximity of the LS absorption/emission region or both and thus needs to be studied further.

In the second part of the thesis, a radioactivity pre-detector for JUNO is envisioned and developed. The Online Scintillator Internal Radioactivity Investigation System (OSIRIS) will determine the radioactive contamination of the LS by a rate analysis of ^{214}Bi-^{214}Po-coincidence-signals compared to the accepted background rate. A Monte Carlo simulation was created in `Geant4` to study the feasibility of such a device and investigate various designs with regards to their efficiency. Several concept stages are briefly shown and the final simulation is described, along with data production, processing and analysis methods. The simulation data shows that a nested arrangement of cylindrical tanks with a 3 m LS volume, a $\sim$ 5 m buffer housing 100 8" PMTs and an 8 m water shield is able to determine radioactive contaminations up to $2.22 \cdot 10^{-10}$ Bq/kg within 24 hours using a 50 cm fiducial volume cut. This is sufficient to verify the baseline purity requirements for solar neutrino investigation in JUNO ($1.24 \cdot 10^{-9}$ Bq/kg) as well as the requirements for the mass ordering search ($1.24 \cdot 10^{-8}$ Bq/kg).

Contents

Note on Citations

Whenever an information was procured from external sources or further information can be obtained elsewhere it is marked as such by a citation. The placement of the citation provides context on which part of the text it refers to. If the citation is directly attached to a word, it refers to that word or couple of words that precede it. If the citation is directly attached to a punctuation mark, such as a full stop or comma, it refers to the entire preceding sentence or clause. Furthermore, if it is attached to a colon preceding an equation, the equation is included as well. If the citation stands at the end of a paragraph, there is a distinction whether or not it is directly attached to the final full stop or separated by a space: In the former case it only refers to the final sentence of the paragraph, while in the latter case, it refers to the entire paragraph. This convention also extends to subscripts and labels of tables and figures, where it also includes the contents of said table/figure if separated by a space.

Chapter 0

Introduction

Neutrino physics is a very exciting and rewarding field of study, as there are not only open questions regarding the so-called ghost particles themselves – masses, mixing angles, Majorana character, etc. – but they also act as a doorway to many other interesting research topics: Multi-messenger astronomy aims to combine light, neutrino and gravitational wave signals into a multi-faceted source of information on supernovae, gamma ray bursts, active galactic nuclei or other astronomical objects and events. Neutrinos can act as probes from secluded regions in space, like the interiors of the sun and the earth. Investigation of a CP-violating phase in the neutrino sector might shed light on the matter/antimatter-asymmetry in the universe while exploration of possible sterile neutrinos could give hints on the composition of dark matter in the cosmos.

However, neutrino observation is still a challenging endeavour, given their low interaction probability. Huge detectors with meticulously tuned sensors are built to achieve this goal. Various approaches using different technologies are implemented, each with its own distinct advantages and disadvantages. One of these is the Jiangmen Underground Neutrino Observatory (JUNO) in southern China which utilizes light emission from liquid scintillators (LS) to expose weak nuclear reactions of neutrinos with the detector materials. JUNO contains a $\varnothing = 35.4\,\mathrm{m}$ large acrylic sphere filled with 20 kt of LS, surrounded by an equal amount of ultrapure water within a $\varnothing = 43.5\,\mathrm{m}$ cylindrical tank. With these dimensions, JUNO has stringent purity requirements for its constituent liquids. Transparency needs to be high and radioactive contamination low, as cleanliness is paramount for reduction of background event rates and reliable signal reconstruction.

Towards this goal, the work at hand investigates means to examine the JUNO LS purity, both on a small and large scale. In the hardware part of this thesis, a laboratory experiment has been realized to determine Rayleigh scattering behaviour of LS fluids, relevant for understanding and reproducing the travel path of light signals within the JUNO detector. At the same time, a Monte Carlo simulation was created to investigate the feasibility of a radiopurity monitor for the JUNO filling system, constituting the software part of the thesis. The Online Scintillator Internal Radioactivity Investigation System (OSIRIS) is meant to be inserted in the JUNO filling line and act as a failsafe system. As such, it can issue a warning signal when the radioactivity of the LS surpasses the required limits so the detector filling may be stopped and the LS further purified before the central detector is contaminated.

Chapter 1 gives an overall introduction on the present knowledge of neutrino physics, discussing their role in the standard model (SM) of particle physics but also behaviours that go beyond the SM, such as mixing and oscillation phenomena. The corresponding formalisms will be addressed as well as some theories on neutrino masses, which are required for oscillations. Furthermore, the chapter gives an overview on the currently known values of neutrino parameters and also briefly touches on sterile neutrinos and a possible Majorana character.

Chapter 2 will explore JUNO, from the detector dimensions and materials to the neutrino detection channels. The radioactive backgrounds will be discussed, serving as a motivation for the aforementioned radiopurity monitor OSIRIS. The chapter ends with an overview of the JUNO physics programs.

The general concept of liquid scintillators is presented in chapter 3. It explains the underlying physical principles and also describes issues with self-absorption and how wavelength shifters can be used to counteract this effect. This topic also leads into the scattering properties that will be analyzed in the subsequent chapter. Finally, the different chemical constituents of the liquids used in this thesis are listed alongside their most relevant properties.

Chapter 4 deals with the scattering experiment. It presents the physics of Rayleigh scattering and details the concept of the laboratory setup. Each component is described, as well as the procedures to calibrate them. The analysis procedure and error estimation is discussed before reviewing the results obtained from calibration samples with known and LS samples with unknown Rayleigh scattering lengths.

The OSIRIS detector is the topic of chapter 5. The motivation and concept is presented before highlighting the development process of the Monte Carlo simulation and its most important milestones. The last iteration of the simulation is then described in detail, followed by the procedures for data production, processing and analysis, alongside the outcome of the feasibility study.

Chapter 6, finally, presents a brief summary of the thesis goals and conclusions. The results of the Rayleigh scattering experiment are recapitulated and a small outlook on possible next steps and improvements is given. Similarly, the OSIRIS simulation is revisited and its findings summed up. As OSIRIS has become an official subsystem of JUNO after the investigations from this thesis were conducted, an update will be given on the developments since then and the current status of the project.

Chapter 1

Neutrinos

Neutrinos have a long-standing history of being the cause for many a mystery in the field of particle physics. Even their very introduction into physics as a whole was more of an desperate necessity rather than an actual discovery: What would end up becoming the neutrino was initially hypothesized by Wolfgang Pauli in 1930 as an additional particle inhabiting the atomic nucleus, carrying away part of the energy during beta decay, thus explaining the continuous energy spectrum of the electron, which had physicists puzzled at the beginning of the 20th century.

In an analogy to the monoenergetic alpha decay spectrum, scientists expected the beta decay spectrum to be equally discrete. Yet in 1914, James Chadwick measured a continuous energy distribution using a magnetic spectrometer and a Geiger counter.[1] This discovery was confirmed and refined over the next two decades, much to the dismay of the scientific community, which was still uncertain how to reconcile this factum with the contemporary understanding of the structure and internal processes within atomic nuclei at the time. This discrepancy even went so far that Niels Bohr suggested in 1929/1930 that energy conservation could be violated on an individual case basis and only held true in a statistical sense.[2]

Enter Wolfgang Pauli: To explain this conundrum, on December 4th 1930 he penned his famous letter to the nuclear physics conference held at the same time in Tübingen, theorizing an additional, never before detected particle which he dubbed the "Neutron"[sic], in accordance with the naming convention of the other "two" nuclear constituents[1], the electron and the proton. He predicted this particle to possess spin-$1/2$ and thus follow the exclusion principle in order to resolve some lingering issues with the nuclear magnetic moment due to the "constituent" electrons. He also postulated it to have mass comparable to the electron but no larger than 0.01 of the proton mass, thus not propagating at the speed of light.[4] While conceiving new particles to explain or even invent new phenomena seems to be the go-to-solution in modern particle physics, such an idea was unheard of back in the day, and even Pauli seemed to think this line of thought to be preposterous, with him later referring to his postulation of "a particle that cannot be detected" as "a terrible thing".[5]

Of course Pauli's predicted "neutron" did not end up being the modern neutron from nuclear physics, which – coincidentally – would also be discovered by Chadwick in 1932,

[1] At this time, the "nuclear electron" model was still prevalent, postulating that the charge of half of the protons in the nucleus is compensated by electrons, in order to explain why nuclei are severely heavier than just the sum of the protons that make up its charge.[3]

when examining electrically neutral radiation from beryllium after irradiation with alpha particles: $^{9}\mathrm{Be}+\alpha \rightarrow ^{12}\mathrm{C}+n$ [6, 7, 8] – a discovery that would yield him the Nobel Prize in the year 1935. This new particle was later found to be a nuclear constituent and possess a mass roughly equal to that of the proton, leading to Enrico Fermi renaming Pauli's as-of-then still hypothetical particle the "neutrino". The neutrino would also end up possessing some different properties compared to how it was initially envisioned, specifically with regards to its mass, even though Pauli was already spot-on with it being a fermion.

Still, the neutrino remained a hypothetical particle for the duration of the 1930s, 1940s and most of the 1950s, until a first indication at Hanford in 1953 and then the final discovery of the electron antineutrino at the Savannah River Plant in 1956 as part of "Project Poltergeist",[9] for which Clyde L. Cowan and Frederick Reines ended up receiving the 1995 Nobel Prize in Physics. This discovery was made by the means of a neutrino-induced nuclear conversion, the so called Inverse Beta Decay (IBD),

$$\bar{\nu}_e + p \rightarrow e^+ + n, \tag{1.1}$$

a detection channel which would open up a window to more elaborate neutrino analyses in the future. Not long thereafter, the muon neutrino was identified as its own particle in 1962 at the Brookhaven National Laboratory, thus solidifying the concept of lepton flavor across particle physics.[10] This discovery was honored with the Nobel Prize for Leon Max Lederman, Melvin Schwartz and Jack Steinberger in 1988. Lastly, the final neutrino flavor, associated with the tauon, would end up being discovered by the DONUT experiment at Fermilab in 2000.[11]

But just as physicists started to think they understood the elusive ghost particles, the neutrino came up with the next enigma: In 1964, the Homestake experiment set out to measure the neutrino flux of the sun, which by now was known to generate electron-type neutrinos as a byproduct of its fusion processes. The detection was successful – but they saw only $\sim$ 1/3rd of the expected amount of neutrinos. Confirmed by other experiments such as KamiokaNDE, SAGE and GALLEX, this deficit once again perplexed the scientific community and persisted throughout the latter half of the 20th century, know as the "solar neutrino problem".[12] Concurrently, a similar issue arose for the atmospheric neutrinos, which are produced by cosmic radiation interacting with the earth's atmosphere and therefore expected to have a certain flavor ratio of 2:1 between the muon and electron type – yet experiments such as IMB, Fréjus or NUSEX detected significantly less.[13]

The first piece to the puzzle was provided in 1998 when Super-Kamiokande measured the atmospheric neutrino flux for both electron and muon flavour, and established a disappearance of muon neutrinos, if they passed through the earth before detection.[14] They also confirmed the solar neutrino problem, which was then investigated in-depth by the Sudbury Neutrino Observatory (SNO) starting 1999, discovering a reduced solar neutrino flux for the individual electron neutrino, but consistent with predictions when combining all flavors.[15] Both of these experiments combined indicated a mechanicsm for flavor change, but even then, there were still multiple possible solutions that fit the data, such as neutrino decay, Lorentz-symmetry violation and many more. In the end, the Kamioka Liquid Scintillator Antineutrino Detector (KamLAND) had the final say on the matter, when they measured both the energy- and distance-dependency of the flavor transitions by probing the neutrino spectra of various nuclear reactors.[16] The data of all three experiments painted a picture that showed neutrinos possess mass, albeit very small, leading to quantum-mechanical effects that facilitate flavor transitions due to different

mass and flavor eigenstates (c.f. section 1.3). This results in phenomena such as flavor oscillations, responsible for the atmospheric neutrino deficit and adiabatic conversions driven by the Mikheyev–Smirnov–Wolfenstein effect, causing the solar neutrino deficit.[17] The discovery of the solar and atmospheric neutrino deficits themselves was awarded with the 2002 Nobel Prize in Physics for Homestake's Raymond Davis, Jr. and KamiokaNDE's Masatoshi Koshiba, while the 2015 Nobel Prize honored Takaaki Kajita (KamiokaNDE, Super-K) and Arthur B. McDonald (SNO) for its solution.

Today, the claim that the neutrino "cannot be detected" could hardly be further from the truth. Although challenging, countless detectors have not only identified but even probed the spectra, quantum numbers and myriads of other properties of neutrinos, giving rise to its very own branch of particle physics. Neutrinos are being used as messengers to probe conditions within the sun[18, 19], draw conclusion on supernovae such as the famous SN1987A[20] and in the wake of gravitational wave detection, neutrinos play a significant part in the rise of multi-messenger astronomy[21].

That is not to say that all properties of neutrinos have been fully understood and all riddles solved: Not only have not all parameters involved in neutrino oscillations been measured yet, even the fact that neutrinos have mass in the first place raises questions about the standard model formulation, in which neutrinos are incapable of acquiring mass in the same way that other particles do. This deficit has given rise to multiple extensions to the standard model, none of which could be verified as of now. Moreover, many of these theories predict additional phenomena related to neutrinos such as Majorana-character, a new type of coupling or Lepton-number violation, all of whose validities have yet to be tested.

This chapter aims to give a brief overview of the current state of knowledge on neutrino properties, specifically in relation to flavor oscillations, describe some of the experiments associated to these findings and provide a short outlook on currently unanswered issues in the field of neutrino physics and how they might be solved in the future.

1.1 Standard Model Neutrinos

The Standard Model (SM) of particle physics is a local Yang-Mills gauge theory characterized by the symmetry group

$$G_{\mathrm{SM}} = SU(3)_C \times SU(2)_L \times U(1)_Y \tag{1.2}$$

comprising the three gauge fields of color charge (C), weak isospin (L) and weak hypercharge (Y). As such it is Lorentz-invariant and – since its Lagrangian is of dimension 4 – renormalizable. It governs the behavior of the eponymous standard model particles; six quarks divided into three generations, charged leptons from three families and their accompanying neutrinos as well as the respective antiparticles to all aforementioned fermions. It also includes the scalar Higgs boson and several gauge bosons: The photon, eight gluons as well as the $\mathrm{W}^{\pm}$ and Z bosons. Neutrinos specifically are named after their charged counterparts: The electron neutrino, the muon neutrino and the tauon neutrino. An overview of the leptons and bosons with their respective gauge group representations and the charge and hypercharge quantum numbers can be found in table 1.1.

Note that the chirally right-handed neutrino does not exist in the SM, since the weak interaction only couples to chirally left-handed particles whereas right-handed charged

leptons can still couple to the electromagnetic force, so their inclusion in the standard model gives rise to a Yukawa-term in the Lagrangian

$$\mathcal{L}_{\text{Yukawa}} = -y\overline{\psi_L}\phi\psi_R + \text{h.c.} \tag{1.3}$$

1st Gen.	2nd Gen.	3rd Gen.	$SU(3)_C$	$SU(2)_L$	Y_{W}	Q
$\begin{pmatrix} u \\ d \end{pmatrix}_L$	$\begin{pmatrix} c \\ s \end{pmatrix}_L$	$\begin{pmatrix} t \\ b \end{pmatrix}_L$	$\mathbf{3}$	$\mathbf{2}$	$1/3$	$\begin{matrix} 2/3 \\ -1/3 \end{matrix}$
u_R	c_R	t_R	$\overline{\mathbf{3}}$	$\mathbf{1}$	$4/3$	$2/3$
d_R	s_R	b_R	$\overline{\mathbf{3}}$	$\mathbf{1}$	$-2/3$	$-1/3$
$\begin{pmatrix} \nu_e \\ e \end{pmatrix}_L$	$\begin{pmatrix} \nu_\mu \\ \mu \end{pmatrix}_L$	$\begin{pmatrix} \nu_\tau \\ \tau \end{pmatrix}_L$	$\mathbf{1}$	$\mathbf{2}$	-1	$\begin{matrix} 0 \\ -1 \end{matrix}$
e_R	μ_R	τ_R	$\mathbf{1}$	$\mathbf{1}$	-2	-1
Bosons			$SU(3)_C$	$SU(2)_L$	Y_{W}	Q
$H = \begin{pmatrix} H^+ \\ H^0 \end{pmatrix}$			$\mathbf{1}$	$\mathbf{2}$	1	$\begin{matrix} 1 \\ 0 \end{matrix}$
$\begin{pmatrix} W^+ \\ W^- \end{pmatrix}$			$\mathbf{1}$	$\mathbf{2}$	0	$\begin{matrix} +1 \\ -1 \end{matrix}$
$\begin{pmatrix} Z^0 \\ \gamma \end{pmatrix}$			$\mathbf{1}$	$\mathbf{2}$	0	0
g			$\mathbf{8}$	$\mathbf{1}$	0	0

Table 1.1: A list of the particles from the Standard Model, their representations in the assigned gauge groups as well as their respective weak hypercharge and electric charge.[2]

[2]This thesis uses the definition that $Q = T_3 + \frac{1}{2}Y_W$, however in some texts the convention $Q = T_3 + Y_W$ is used instead, thus rescaling the weak hypercharge by a factor of two.

describing the interaction between left- and right-handed lepton fields ψ_L and ψ_R with a scalar field ϕ, in the SM specifically the Higgs field, and which – after spontaneous symmetry-breaking – yields mass terms for the involved leptons. The strength of this interaction depends on the scale of the entries in the Yukawa coupling matrix. However, the lack of right-handed neutrino fields in the SM results in massless neutrinos as there are no right-handed fields to complement this interaction.

Of course, experiments have proven that this is not entirely the case. Evidently, neutrinos do have mass as indicated by flavor oscillations (c.f. chapter 1.3). Thus, neutrino masses have joined the list of observations that prove the standard model to be incomplete, alongside dark matter, dark energy, the baryon asymmetry and – obviously – gravity. Consequently, several extensions to the standard model have arisen in order to rectify this omission, some of which will be shortly addressed in the following section.

1.2 Neutrino Mass Models

The topic of neutrino mass is strongly related to the question of particle identity. Currently, the issue of whether or not the neutrino is its own antiparticle is still unresolved. In the scenario that neutrinos are distinct particles from antineutrinos, they are referred to as Dirac fermions, whereas if both of them can be described by the same field, they are called Majorana fermions. Various mass models give different predictions on the inherent Dirac/Majorana-character of neutrinos.

Probably the most straight-forward way of adding neutrino mass to the standard model is the introduction of right handed Weyl spinors that behave as singlets to all standard model gauge fields. These would be identified as right-handed neutrinos or left-handed antineutrinos. Their inclusion then allows for Yukawa-interactions between left- and right-handed neutrinos with the Higgs field:

$$\mathcal{L}_{\mathrm{D}} = -y^{\alpha i}\overline{L_{L\alpha}}\tilde{H}\nu_{Ri} + \mathrm{h.c.} \tag{1.4}$$

In this notation, L_{Li} refers to the left-handed Dirac doublet that combine the Weyl spinors for left-handed charged leptons and left-handed neutrinos into one object. With $\tilde{H} = i\sigma_2 H^*$ and H being the Higgs field, ν_{Ri} the right-handed neutrinos and $y^{\alpha i}$ the components of the Yukawa coupling matrix, the size of the Dirac masses depends on the coupling strength and the Higgs vacuum expectation value:[22, 23]

$$m_{\mathrm{D}}^{\alpha i} = y^{\alpha i} \cdot v \tag{1.5}$$

Note that one separate right-handed neutrino is required for every left-handed SM neutrino that is supposed to acquire mass, the minimum of which being two (c.f. 1.3). Now, since the sum of all active neutrino masses is constrained to be smaller than 0.17 eV from cosmology[24] or at least up to the limit on the electron neutrino mass of $m(\nu_e) = 2.05\,\mathrm{eV}$ from the Troitsk-experiment[25], and the Higgs vacuum expectation value was measured to be $v = 174\,\mathrm{GeV}$[26], this dictates the Yukawa coupling for neutrinos to be in the order of $\mathcal{O}(10^{-12})$, which is uncharacteristically small compared to Yukawa couplings of charged leptons ($\mathcal{O}(10^{-6}$–$10^{-2})$) or quarks ($\mathcal{O}(10^{-5}$–$1)$)[27]. This implication is often called into question as there is seemingly no reason for neutrino couplings to be so many orders of magnitude smaller than their charged counterparts.

If, on the other hand, one chooses to describe neutrinos and antineutrinos by the same field, this leads to an interaction term in the Lagrangian that couples the left-handed fermion fields to the Higgs field twice:[22, 23]

$$\mathcal{L}_{\mathrm{W}} = -\frac{\lambda^{\alpha\beta}}{2\Lambda}(\overline{L_{L\alpha}}\tilde{H})(\tilde{H}^T L^c_{L\beta}) + \mathrm{h.c.} \tag{1.6}$$

Formula (1.6) is a gauge invariant dimension 5 operator, commonly known as the Weinberg Operator.[28] Its very inclusion explicitly violates lepton number by 2. After electroweak symmetry breaking, the Weinberg operator gives rise to Majorana masses for the SM neutrinos, in the form of

$$\mathcal{L}_{\mathrm{M}} = -\frac{m_{\mathrm{M}}^{\alpha\beta}}{2}\overline{\nu_{L\alpha}}\nu^c_{L\beta} + \mathrm{h.c.}; \qquad m_{\mathrm{M}}^{\alpha\beta} = \frac{\lambda^{\alpha\beta}v^2}{\Lambda}. \tag{1.7}$$

In this case it is suppressed by the factor Λ which denotes a high-energy scale where the new physics responsible for the Majorana masses arise, similarly to how v is representative for the electroweak energy scale.

It should be noted that these two scenarios are not mutually exclusive. One of the most prominent approaches for neutrino mass acquisition, the so called seesaw mechanism, adds right-handed Majorana neutrinos to the SM. The corresponding Lagrangian

$$\mathcal{L}_{\mathrm{SI}} = -y^{\alpha i}\overline{L_{L\alpha}}\tilde{H}\nu_{Ri} - \frac{M_R^{ij}}{2}\overline{\nu^c_{Ri}}\nu_{Rj} + \mathrm{h.c.} \tag{1.8}$$

has the previously seen interaction term between left-handed SM neutrinos and right-handed singlets as well as a Majorana mass term. Specifically, this is called the seesaw type-I. A variation thereof has the new right-handed neutrinos added to the SM being $SU(2)_L$-triplets instead of singlets. This is commonly referred to as the type-III seesaw. Either way, after spontaneous symmetry breaking, this results in a Majorana mass matrix giving mass to both types of neutrinos in the form of

$$\mathcal{L}_{\mathrm{M}} = -\frac{1}{2}\overline{\begin{pmatrix}\nu_L & \nu^c_R\end{pmatrix}}\begin{pmatrix}0 & m_{\mathrm{D}}\\ m_{\mathrm{D}}^T & M_R\end{pmatrix}\begin{pmatrix}\nu^c_L\\ \nu_R\end{pmatrix} \tag{1.9}$$

where m_{D} is the earlier Dirac mass matrix from equation (1.5) and M_R the right-handed neutrino Majorana mass matrix from equation (1.8). In this case the SM neutrinos acquire a mass of the size $m_\nu = -m_{\mathrm{D}}M_R^{-1}m_{\mathrm{D}}^T$. It is evident that the larger the components of M_R, the smaller the overall SM neutrino mass will be. The right-handed neutrinos are therefore meant to compensate for the light SM neutrinos, which is why they are also called heavy neutrinos. This is where the seesaw mechanism inherits its name from. [22, 23]

There exists a third possibility within the standard paradigm of the seesaw mechanism. The so-called type-II seesaw suggests that instead of extending the SM by a lepton triplet, one could rather add a boson triplet Δ for the neutrinos to couple to that serves the same purpose as the Higgs. In a term similar to equations (1.5) and (1.8), the left-handed SM leptons couple to this new Higgs triplet and neutrinos aquire mass after spontaneous symmetry breaking:

$$\mathcal{L}_{\mathrm{SII}} = -\frac{y_\Delta^{\alpha\beta}}{2}\overline{L_{L\alpha}}\Delta i\sigma_2 L^c_{L\beta} - \lambda_\Delta M_\Delta H^T i\sigma_2 \Delta H + \mathrm{h.c.} \Rightarrow M_{\mathrm{SII}}^{\alpha\beta} = \frac{\lambda_\Delta v^2}{M_\Delta}y_\Delta^{\alpha\beta} \tag{1.10}$$

with $y_\Delta^{\alpha\beta}$ and λ_Δ being the coupling strengths between the new Higgs triplet and the left-handed SM leptons or the SM Higgs, respectively. In this case, the Higgs triplet mass M_Δ is compensating for the small SM neutrino masses instead of a right-handed heavy neutrino.

So far, only the three canonical seesaw models have been mentioned. Other possibilities exist, for example combining type I and type II into the type (I+II) seesaw model. In this scenario, equation (1.9) is modified to include an additional mass matrix $M_L = y_\Delta v_\Delta$ which yields[23]

$$\mathcal{L}_{\text{I+II}} = -\frac{1}{2}\overline{\begin{pmatrix}\nu_L & \nu_R^c\end{pmatrix}}\begin{pmatrix}M_L & m_\text{D}\\ m_\text{D}^T & M_R\end{pmatrix}\begin{pmatrix}\nu_L^c\\ \nu_R\end{pmatrix} \tag{1.11}$$

and resulting in modified neutrino masses: $m_\nu = M_L - m_\text{D} M_R^{-1} m_\text{D}^T$. Other possible variations include the inverse seesaw or the scotogenic model.[23] Even alternative non-seesaw-suggestions exist, such as the radiative generation of neutrino masses, for example in the Zee-Babu-model.[29, 30] Suffice it to say, there are many more theories to obtain neutrino masses, all of which would go far beyond the scope of this thesis.

1.3 Neutrino Mixing and Flavor Conversion

Regardless of which of the aforementioned neutrino mass models is realized in nature, the existence of massive neutrinos leads to an interesting quantum mechanical phenomenon: Neutrino mixing. Mixing is based on the premise of neutrinos possessing two distinct sets of eigenstates. Neutrinos are generated in flavor eigenstates while interacting with the weak force but propagate in mass eigenstates due to the effect of gravity. These two types of states behave like two different sets of orthonormal bases in phase space. Instead of having an injective correspondence, each flavor state can be written as a weighted superposition of the three mass states and vice versa:

$$|\nu_\alpha\rangle = \sum_{i=1}^{3} U_{\alpha i}^* \,|\nu_i\rangle \qquad |\nu_i\rangle = \sum_{\alpha=e,\mu,\tau} U_{\alpha i}\,|\nu_\alpha\rangle \tag{1.12}$$

Note that in the case of antineutrinos, the complex conjugate is imposed on the right equation instead of the left.

The object $U_{\alpha i}$ governing this transition is called the Pontecorvo-Maki-Nakagawa-Sakata mixing matrix, or PMNS matrix for short. It behaves similarly to the Cabibbo-Kobayashi-Maskawa (CKM) matrix from the quark sector, that describes flavor-changing weak decays and quantifies phenomena such as oscillations of K^0 into its antiparticle $\overline{K^0}$, violating strangeness conservation by two. Well aware of this transition, Bruno Pontecorvo predicted similar behavior for the neutrinos and suggested this theory be tested in detectors similar to the Cowan-Reines-experiment or the Brookhaven reactor neutrino experiment by Ray Davis Jr.[31] Although he was still referring to neutrino-antineutrino-oscillations at the time, Ziro Maki, Masami Nakagawa and Shoichi Sakata later transposed this idea to the flavor regime, giving the PMNS matrix its complete name.[32] In the three flavor case, it is a unitary 3×3 matrix[3] characterized by three

[3] In some scenarios, the PMNS matrix is no longer unitary, such as in the case of sterile neutrinos (c.f. 1.4), where it is reduced to a submatrix of a larger unitary $N \times N$ matrix[33] or in the seesaw mechanism where mass terms from the right-handed neutrinos affect the mixing matrix[34, 35].

mixing angles θ_{12}, θ_{13} and θ_{23} with the abbreviations $s_{ij} \equiv \sin\theta_{ij}$ and $c_{ij} \equiv \cos\theta_{ij}$, as well as a complex phase δ_{CP} which is nonzero in case of inherent CP-violation in the neutrino sector. Fully written out, the PMNS matrix reads as follows:

$$U = \underbrace{\left.\begin{pmatrix} c_{12}c_{13} & s_{12}c_{13} & s_{13}e^{-i\delta_{CP}} \\ -s_{12}c_{23} - c_{12}s_{13}s_{23}e^{i\delta_{CP}} & c_{12}c_{23} - s_{12}s_{13}s_{23}e^{i\delta_{CP}} & c_{13}s_{23} \\ s_{12}s_{23} - c_{12}s_{13}c_{23}e^{i\delta_{CP}} & -c_{12}s_{23} - s_{12}s_{13}c_{23}e^{i\delta_{CP}} & c_{13}c_{23} \end{pmatrix}\right]\alpha}_{i} \tag{1.13}$$

As previously mentioned, both flavor and mass eigenstates provide two distinct orthonormal bases in phase space, and in accordance with the formalism of three angles and one phase included in the PMNS matrix, the transition between both bases can also be parametrized by three individual rotation matrices, each governed by one of the mixing angles:

$$U = \begin{pmatrix} 1 & 0 & 0 \\ 0 & c_{23} & s_{23} \\ 0 & -s_{23} & c_{23} \end{pmatrix} \begin{pmatrix} c_{13} & 0 & s_{13}e^{-i\delta_{CP}} \\ 0 & 1 & 0 \\ -s_{13}e^{i\delta_{CP}} & 0 & c_{13} \end{pmatrix} \begin{pmatrix} c_{12} & s_{12} & 0 \\ -s_{12} & c_{12} & 0 \\ 0 & 0 & 1 \end{pmatrix} \tag{1.14}$$

If neutrinos are indeed Majorana particles, two additional phases η_1, η_2 contribute to the neutrino mixing. They can be incorporated by factoring in one more matrix into equation (1.14), which is:

$$U_M = \begin{pmatrix} 1 & 0 & 0 \\ 0 & e^{i\frac{\alpha_{12}}{2}} & 0 \\ 0 & 0 & e^{i\frac{\alpha_{13}}{2}} \end{pmatrix}. \tag{1.15}$$

These phases do not contribute to neutrino oscillations, as the PMNS matrix elements enter flavor transition probabilities only in quartic terms (c.f. equations (1.19) and (1.21) in subsection 1.3.1) which cancels out their contributions due to the diagonal nature of the Majorana matrix, but they do have an effect on the so called neutrinoless double beta decay $(\beta\beta)_{0\nu}$.

For isobars with even mass number, two mass parabolas exist, due to the pairing term in the Bethe-Weizsäcker-formula, causing the potential decay product of a single β-decay to be energetically unfavorable, such as for the decay of ^{76}Ge or ^{238}U. However, since the subsequent daughter nuclide has even higher binding energy than both, the initial nucleus can forego the intermediate step and emit two β-particles and two neutrinos simultaneously to transition directly into the energetically favorable state, resulting in a double beta decay $(\beta\beta)_{2\nu}$. In the case that said neutrinos possess Majorana character, this process can take place by exchanging a virtual neutrino that is seemingly emitted in the first decay, then reabsorbed in the second, utilizing the fact that Majorana particles correspond to their own antiparticles.[36] Consequentially, the effective Majorana mass determining the $(\beta\beta)_{0\nu}$-amplitude is given by

$$|\langle m\rangle| = \left|\sum_i^3 U_{ei}^2 m_i\right| = \left|m_1 c_{12}^2 c_{13}^2 + m_2 s^2 12 c_{23}^2 e^{i\alpha_{12}} + m_3 s_{13}^2 e^{i(\alpha_{13}-2\delta_{CP})}\right| \tag{1.16}$$

where the two Majorana phases affect the final value due to vectorial addition.[26] As this process would prove neutrinos to be Majorana particles as well as violate lepton number by two units, $(\beta\beta)_{0\nu}$ is highly sought-after by experiments such as CUORE[37], GERDA[38] or MAJORANA[39].

1.3.1 Vacuum Oscillations

As previously mentioned, while neutrinos are produced in the flavor basis of the weak interaction, they propagate in mass states as a result of interacting with gravitational potentials along the way. Consequentially, the flavor a neutrino possesses at the time of its next weak interaction is not necessarily the same it started out with, which lead to the discovery of neutrino mixing in the first place.

Since the mass states are the eigenstates of the Hamiltonian $\mathcal{H}$, their time evolution follows the Schödinger equation:

$$i\frac{\mathrm{d}}{\mathrm{d}t}\left|\nu_i(t)\right\rangle = \mathcal{H}\left|\nu_i(t)\right\rangle = E_i\left|\nu_i(t)\right\rangle = E_i \cdot e^{-iE_i t}\left|\nu_i\right\rangle \tag{1.17}$$

Using equation (1.12), the time evolution of a neutrino that was produced with a certain flavor α can be described as

$$\left|\nu_\alpha(t)\right\rangle = \sum_{i=1}^{3} U_{\alpha i}^{*} e^{-iE_i t}\left|\nu_i\right\rangle . \tag{1.18}$$

Ergo, the probability of said neutrino of initial flavor α to later weakly interact as a neutrino of flavor β (including the possibility of $\alpha = \beta$ or in other words no flavor change having taken place) is given by

$$P_{\nu_\alpha\to\nu_\beta}(t) = \left|\langle\nu_\beta|\nu_\alpha(t)\rangle\right|^2 = \left|\sum_{i=1}^{3} U_{\alpha i}^{*} U_{\beta i} e^{-iE_i t}\right|^2 = \sum_{i,j=1}^{3} U_{\alpha i}^{*} U_{\beta i} U_{\alpha j} U_{\beta j}^{*} e^{-i(E_i - E_j)t} \tag{1.19}$$

Taking into account that neutrinos are ultrarelativistic particles with negligible masses compared to their total energy and momentum, one can approximate $E \simeq p$ to rewrite the exponent in equation (1.18)

$$E_i = \sqrt{p_i^2 + m_i^2} = p_i + \frac{m_i^2}{2p} + \mathcal{O}\left(\frac{m_i^4}{p_i^3}\right) \simeq E_i + \frac{m_i^2}{2E} \tag{1.20}$$

using the Taylor expansion of the square root and neglecting terms of higher orders. Assuming that all mass eigenstates of the same neutrino possess the same total energy $E_i = E_j$, the respective first terms cancel each other out when inserting equation (1.20) into (1.19), and the resulting exponent only depends on the squares of the masses. Additionally considering the ultrarelativistic limit, the travel time can be replaced with the propagation distance as $L \simeq t$ in natural units. Expanding the sum in equation (1.19) and using the unitarity of the neutrino mixing matrix yields the total oscillation probability

$$\begin{aligned} P_{\nu_\alpha\to\nu_\beta}(L) = \delta_{\alpha\beta} &- 4\sum_{i>j} \mathfrak{Re}(U_{\alpha i}^{*} U_{\beta i} U_{\alpha j} U_{\beta j}^{*}) \sin^2\left(\frac{\Delta m_{ij}^2 L}{4E}\right) \\ &+ 2\sum_{i>j} \mathfrak{Im}(U_{\alpha i}^{*} U_{\beta i} U_{\alpha j} U_{\beta j}^{*}) \sin\left(\frac{\Delta m_{ij}^2 L}{2E}\right) \end{aligned} \tag{1.21}$$

where the definition of the mass squared differences $\Delta m^2_{ij} \equiv m^2_i - m^2_j$ has been introduced. In the case of antineutrinos, the formula largely remains the same, but the last term receives a negative sign due to the moved complex conjugate from equation (1.12) when translating flavor states to mass states.

Using the PMNS matrix elements from equation (1.13), it is possible to calculate specific transition probabilities. The survival probability of an electron flavor neutrino as a function of propagation distance, for example, is given by

$$\begin{aligned} P_{\nu_e \to \nu_e}(L) = 1 &- \sin^2(2\theta_{12}) c^4_{13} \sin^2\left(\frac{\Delta m^2_{21} L}{4E}\right) \\ &- \sin^2(2\theta_{13}) c^2_{12} \sin^2\left(\frac{\Delta m^2_{31} L}{4E}\right) \\ &- \sin^2(2\theta_{13}) s^2_{12} \sin^2\left(\frac{\Delta m^2_{32} L}{4E}\right) \end{aligned} \tag{1.22}$$

using the same abbreviations as before. Note that the survival probability is a superposition of three individual oscillations, each with its respective frequency given by the mass squared differences Δm^2_{ij} and their amplitudes by the PMNS matrix elements and the respective mixing angles. The equivalent process electron antineutrinos is the transition being investigated by JUNO in order to determine the neutrino mass ordering (c.f. subsection 1.3.3) and will be expanded upon in subsection 2.4.1.

Since vacuum oscillations repeat themselves periodically it is possible to define the characteristic oscillation length that the neutrino needs to propagate to complete one oscillation period. It is given by

$$L^{\text{osc}}_{ij} = \frac{4E\pi}{\Delta m^2_{ij}} = \frac{2.480(E/\text{MeV})}{(\Delta m^2_{ij}/\text{eV}^2)}\text{m} \tag{1.23}$$

after compensating for omitted factors due to natural units. Mind that oscillation lengths are defined for each mass squared difference Δm^2_{ij} separately that superimpose onto one another, and the neutrino doesn't necessarily return to its initial flavor after traveling one oscillation length.

The previous method of deriving the neutrino oscillation probability uses a plane-wave approximation for the neutrino states. This assumption is generally not justified, given that as physical particles, neutrinos propagate in locally condensed wave packages without one sharp defined momentum. The advantage of the wave package approach is that one omits the assumptions of equal energy and momenta as well as equal propagation time and distance, yet still obtains the same oscillation probability after integrating over all momenta and averaging travel times for one specific propagation distance. This approach is described in-depth in [40] and results in

$$P_{\nu_\alpha \to \nu_\beta}(L) = \sum_{i,j=1}^{3} U^*_{\alpha i} U_{\beta i} U_{\alpha j} U^*_{\beta j} \exp\left[-2\pi i \frac{L}{L^{\text{osc}}_{ij}} - \left(\frac{L}{L^{\text{coh}}_{ij}}\right)^2\right]. \tag{1.24}$$

The result corresponds to formula (1.19), when using the oscillation length from (1.23), but has one additional parameter: The coherence length L^{coh}_{ij} is the propagation distance within which the individual mass state packages of the neutrino still overlap. Specifically,

it is given by:[40]

$$L_{ij}^{\text{coh}} = \frac{4\sqrt{2}E^2}{\left|\Delta m_{ij}^2\right|}\sigma_x \tag{1.25}$$

where σ_x is the size of the wave package in propagation direction. Since oscillations are caused by interference between the mass eigenstates propagating at different speeds, they effectively die down after the neutrino has traveled further than the coherence length and the wave packages have separated. Mathematically speaking, the additional term in the exponent serves as a damping factor for the oscillations.[41]

1.3.2 Matter Effects

The formulae in the previous section were derived primarily for neutrino oscillations in vacuum. However, once neutrinos traverse through matter, several new effects start to appear which need to be taken into consideration. Generally speaking, matter manifests itself as an effective potential for propagating neutrinos, changing their quantum mechanical state and thus their oscillation properties.

As previously mentioned, neutrino mass states are eigenstates of the Hamiltonian (c.f. equation (1.17)). However, the Hamiltonian is not the same in matter as it is in vacuum, due to an additional potential affecting the neutrinos caused by coherent forward elastic scattering with the particles forming the surrounding matter. So instead of the vacuum Hamiltonian $\mathcal{H}_0$, the neutrinos are subject to the matter Hamiltonian $\mathcal{H}_{\text{mat}}(n_P) = \mathcal{H}_0 + V(n_P)$ with $V(n_P)$ being the aforementioned potential which depends on the local matter densities n_P of various types of possible interaction partners of particle type P, such as electrons, protons or neutrons and their constituents. Note that $V(n_P)$ is not a scalar but a matrix, which is diagonal in the flavor basis, due to different charged current (CC) and neutral current (NC) interactions for various neutrino flavors, thus resulting in different potentials for each flavor. [17, 40]

Because of this changed Hamiltonian, the neutrino exhibits a different set of mass eigenstates $|\nu_{im}\rangle$ in matter, denoted by the index m. However, since flavor eigenstates are identical in matter and in vacuum, but the mass eigenstates are not, this also necessitates new mixing angles $\theta_{ij}^m(n_P)$, reflecting the modified transition from the flavor basis to the mass basis and vice versa. Interestingly, the surrounding density may have such a specific profile so that the resulting neutrino oscillations undergo resonant enhancement as the amplitude of the oscillation probability maximizes (c.f. equation (1.22)). There exist three resonances in the three-neutrino-paradigm. [42, 43]

A direct consequence of modified mixing angles that is only tangentially related to neutrino oscillations, but can also result in flavor change is the Mikheyev-Smirnov-Wolfenstein-effect (MSW). For very high-density regimes, like in the core of the sun, the angles change in such a way, that mixing is almost completely suppressed. The neutrinos produced in their electron flavor eigenstates have a nigh direct correspondance to one single mass eigenstate, namely $|\nu_{2m}\rangle$. Reversely, said state is composed almost exclusively of electron flavor. Since neutrino oscillations are caused by interference between different mass eigenstates in the propagating wave package, in the case that only one mass state is produced, no interference takes place and oscillatory flavor transitions are suppressed. If the surrounding medium then has a sufficiently slow density gradient along the neutrino's travel path, the neutrino itself remains undisturbed in its mass state, but the flavor

composition of that state will change, as the effective mixing angles revert back to their vacuum values. The survival and transition probabilities of electron neutrinos from the sun is then directly given by the flavor composition of the second mass eigenstate $|\nu_2\rangle$ and coincides with measurements of the solar neutrino problem from, say, SNO (save for some minor contributions of residual oscillations and ν_e regeneration inside the earth). [17]

This adiabatic conversion is realized when the density at the point of production is significantly larger and the density at the exit point significantly smaller than the resonant density. The resonant region in the sun is defined as the location where the potential for the electron flavor satisfies

$$V_{\mathrm{CC}}(n_e) = \sqrt{2} G_{\mathrm{F}} n_e \stackrel{!}{=} \frac{\Delta m^2_{21} \cos 2\theta_{12}}{2E} \tag{1.26}$$

with G_{F} being the Fermi constant. The sign of the potential determines whether the resonance affects neutrinos or antineutrinos, and with precision measurements of θ_{12}, the MSW effect allowed to establish that Δm^2_{21} possesses an inherent positive sign, meaning that $m^2_2 > m^2_1$. [40, 44, 45]

1.3.3 Mass Ordering

While it was possible to use information obtained from the MSW resonance in the sun to identify the sign of the first mass squared difference Δm^2_{21}, only the absolute value of the analogue atmospheric mass splitting $|\Delta m^2_{31}|$ is currently known. Thus, although confirmed that the second mass eigenstate m_2 is indeed heavier than the first m_1, the third and final state m_3 could still be the heaviest or even the lightest of all three. This leads to the mass ordering (MO) problem, where two different scenarios to arrange the three eigenstates by weight are possible. The so-called normal ordering (NO) follows the regular numbering sequence $m_1 < m_2 < m_3$ whereas the inverted ordering (IO) is given by $m_3 < m_1 < m_2$. The two scenarios are displayed in figure 1.1, with the respective mass squared differences and flavor compositions included.

Identifying the correct ordering is an important goal in particle physics. The sign of Δm^2_{31} is a relevant parameter in and of itself, as it affects the total sum of all three neutrino masses, which therefore determines the sensitivity of $(\beta\beta)_{0\nu}$ experiments[46] while also having impacts on cosmological phenomena[47]. But it's also a significant prior in the search for CP-violation in the neutrino sector, affecting the expected signal, as the wrong hierarchy could mimic effects of the δ_{CP} phase from the PMNS matrix.[48] Lastly, different neutrino mass models predict different MO, so a measurement of $\mathrm{sgn}(\Delta m^2_{31})$ would allow to reject models that are not realized in nature.[49]

Experiments such as T2K[50], NOνA[51] or the upcoming DUNE[52, 53] are set to determine the MO by investigating the differences in oscillation patterns for neutrinos and antineutrinos of dedicated particle beams over long baselines ($\mathcal{O}$(100–1000 km)) due to changes in the matter effects. The PINGU extension for IceCube[54], KM3NeT's ORCA array[55] and Hyper-Kamiokande[56] plan to identify the correct ordering by using similar effects, but use atmospheric neutrinos from cosmic radiation as a source. The JUNO detector on the other hand uses a completely different approach, trying to measure the MO by resolving interference patterns between Δm^2_{31}- and Δm^2_{32}-oscillations that have similar but not identical oscillation lengths. This approach and the design of the detector itself will be covered in-depth in chapter 2.

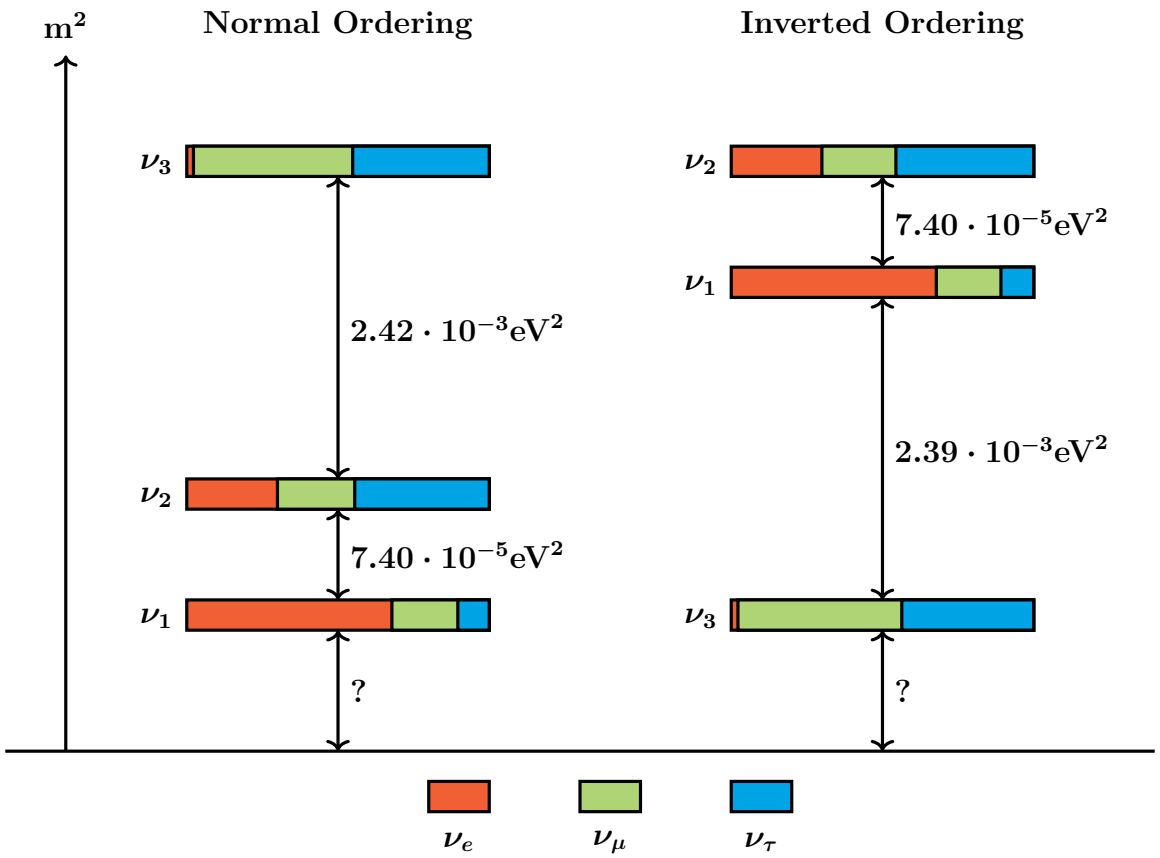

Figure 1.1: The three neutrino mass eigenstates in normal and inverted ordering (not to scale). The mass eigenstates are shown as compositions of the flavor eigenstates ν_e (red), ν_μ (green) and ν_τ (blue). Current global values from table 1.2 were used to calculate $|U_{\alpha i}|^2$ which gives the fraction of each flavor state ν_e, ν_μ, ν_τ contained within the different mass eigenstates ν_1, ν_2, ν_3.

1.4 Sterile Neutrinos

While the number of active neutrino generations – i.e. neutrino flavors that are subject to the weak interaction – are well-known from the decay width of the Z^0 gauge boson,[57] another possible theory of additional neutrinos has arisen in recent years. Ever since the LSND anomaly showed an excess of $\bar{\nu}_\mu \to \bar{\nu}_e$ oscillations compared to three-flavor-expectations,[58] the possibility of a fourth (or more) light neutrino(s) was being considered. This light sterile neutrino would not interact with the weak force and thus not appear in the gauge boson decay, but could potentially be accessed via modified neutrino oscillations. Note that this type of particle does not necessarily correspond to the heavy right handed neutrinos from section 1.2, which are also sterile with respect to the weak force.

Generally speaking, the existence of one or more sterile neutrinos would expand the PMNS matrix from equation (1.13) into a unitary $N \times N$ matrix, with $(N-3)$ sterile neutrinos in addition to the three active neutrino flavors. The original 3×3 PMNS matrix is still contained as a submatrix in the upper left corner, although it is no longer unitary on its own:

$$U' = \begin{pmatrix} U_{e1} & U_{e2} & U_{e3} & \dots & U_{en} \\ U_{\mu 1} & U_{\mu 2} & U_{\mu 3} & \dots & U_{\mu n} \\ U_{\tau 1} & U_{\tau 2} & U_{\tau 3} & \dots & U_{\tau n} \\ \vdots & \vdots & \vdots & \ddots & \vdots \\ U_{s_{(N-3)}1} & U_{s_{(N-3)}2} & U_{s_{(N-3)}3} & \dots & U_{s_{(N-3)}n} \end{pmatrix} \tag{1.27}$$

The generalized formula for calculating oscillation probabilities from equation (1.21) still holds, but additional terms come into play that not only affect active-sterile and sterile-active oscillations but can even influence active-active transitions. However, since the active neutrino sector has been thoroughly examined without showing significant hints for such contributions, the allowed parameter regions for sterile mixing are restricted accordingly. As a consequence, search for sterile neutrino oscillations is usually conducted on short baselines, before active flavor transitions have the chance to arise. Specifically, the current preferred mass squared difference for sterile oscillations in the $(3+1)$ scenario lies in the region of $\Delta m^2_{4i} \simeq \mathcal{O}(1\,\mathrm{eV})$.

At the present time, the sterile neutrino sector is overconstrained, and tension exists between various experiments, specifically between neutrino beam appearance experiments (such as LSND[58] or MiniBooNE[59]) and disappearance experiments (like MINOS/MINOS+[60]) which explore the same parameter space but favor or exclude conflicting regions. Other experiments, such as IceCube, also exclude the favored parameter space from appearance experiments.[61] On the other hand, some small hints have also been given by gallium-based experiments GALLEX and SAGE, leading to the so called gallium anomaly.[62] Similarly, some reactor neutrino disappearance experiments (such as Bugey[63], Gösgen[64], Krasnoyarsk[65], Rovno[66] and SRP[67], see reference [68]) observe a deficit in detected electron antineutrinos – dubbed the Reactor Antineutrino Anomaly (RAA) – at short baselines in the order of $\mathcal{O}(1\,\mathrm{m})$ consistent with the sterile neutrino hypothesis, while other reactor experiments (Daya Bay[69, 70], NEOS[71], DANSS[72]) exclude the favored RAA region and/or prefer different explanations such as flux modulations from fission material variations. All in all, the currently available data is contradictory and the results inconclusive, but it is expected that upcoming short baseline experiments will shed additional light on the issue. A detector such as JUNO could potentially also contribute to solving the inconsistencies (see section 2.4).

1.5 Parameter Values

The current neutrino parameter values from a combined analysis of various solar, atmospheric, reactor and accelerator experiments is given in table 1.2.[73] At the time of this writing, the following conclusions can be derived from the results: θ_{13} is confirmed to be nonzero. Maximal θ_{23}-mixing is unlikely and for both orderings, a $\theta_{23} > 45°$ octant is favored, although still not verified. A nonzero δ_{CP} is hinted at. Lastly, there is a slight preference for NO at roughly $2\,\sigma$, yet the tendency is too weak to fully exclude IO.

	Normal Ordering (best fit)		Inverted Ordering ($\Delta\chi^2 = 4.14$)	
Parameter	bfp $\pm 1\,\sigma$	$3\,\sigma$ range	bfp $\pm 1\,\sigma$	$3\,\sigma$ range
$\sin^2\theta_{12}$	$0.304^{+0.013}_{-0.012}$	$0.269 \to 0.343$	$0.304^{+0.013}_{-0.012}$	$0.269 \to 0.343$
θ_{12} [°]	$33.44^{+0.78}_{-0.75}$	$31.27 \to 35.86$	$33.45^{+0.78}_{-0.75}$	$31.27 \to 35.87$
$\sin^2\theta_{23}$	$0.570^{+0.018}_{-0.024}$	$0.407 \to 0.618$	$0.575^{+0.017}_{-0.021}$	$0.411 \to 0.621$
θ_{23} [°]	$49.0^{+1.1}_{-1.4}$	$39.6 \to 51.8$	$49.3^{+1.0}_{-1.2}$	$39.9 \to 52.0$
$\sin^2\theta_{13}$	$0.02221^{+0.00068}_{-0.00062}$	$0.02034 \to 0.02430$	$0.02240^{+0.00062}_{-0.00062}$	$0.02053 \to 0.02436$
θ_{13} [°]	$8.57^{+0.13}_{-0.12}$	$8.20 \to 8.97$	$8.61^{+0.12}_{-0.12}$	$8.24 \to 8.98$
δ_{CP} [°]	195^{+51}_{-25}	$107 \to 403$	286^{+27}_{-32}	$192 \to 360$
Δm^2_{21} [10^{-5}eV^2]	$7.42^{+0.21}_{-0.20}$	$6.82 \to 8.04$	$7.42^{+0.21}_{-0.20}$	$6.82 \to 8.04$
Δm^2_{3l} [10^{-3}eV^2]	$+2.514^{+0.028}_{-0.027}$	$+2.431 \to +2.598$	$-2.497^{+0.028}_{-0.028}$	$-2.583 \to -2.412$

Table 1.2: Current knowledge on the oscillation parameters and their associated errors. Δm^2_{3l} is given as $\Delta m^2_{31} > 0$ for NO and $\Delta m^2_{32} < 0$ for IO.[73]

Chapter 2

JUNO

The Jiangmen Underground Neutrino Observatory (JUNO) is a 20 kt liquid scintillator (LS) reactor neutrino experiment currently under construction near Jinji town, close to Kaiping city in the eponymous Jiangmen prefecture of the Guangdong province in southern China. Located under the Dashi mountain range, the facility will be placed under $\sim$ 700 m of rock overburden which roughly equates to 1,900 meters of water equivalent (m.w.e.). The experiment itself is primarily designed to determine the neutrino mass ordering (c.f. section 1.3.3) with at least $3\,\sigma$ precision, to which end the location was chosen to be at an exact 53 km distance from two nuclear power plants, Yangjiang to the southwest and Taishan to the southeast, which are expected to provide a total power of 26.6 GW[74] by the time JUNO commences operation. The specifics of the MO mea-

Figure 2.1: The location of the JUNO experimental hall as well as the Yangjiang and Taishan nuclear power plants in relation to each other. The cities of Kaiping, Zhuhai and Macau are marked for reference. The two cyan lines denote the 53 km long neutrino travel paths from the reactor cores to the detector.

surements will be covered in-depth in subsection 2.4.1. However, JUNO also allows for a varied range of other physics investigations to be conducted, including but not limited to improvements of the uncertainty for known oscillation parameters, detection of supernova neutrinos, both from an immediate burst or the diffuse supernova neutrino background (DSNB), investigation of geoneutrinos from the earth's core as well as the search for sterile neutrinos.[75] Details of the additional physics potential will be mentioned in subsection 2.4.3.

2.1 The JUNO Detector

Using LS technology for neutrino tagging, the JUNO detector's main component is the large acrylic sphere encapsulating the 20 kt of scintillating organic fluid that serve as the main detection medium. This liquid is additionally enhanced with wavelength shifters in order to counteract self-absorption and improve transparency and light yield. The acrylic sphere is supported by a large stainless steel lattice shell (SSLS), onto which inward- and outward-facing photomultiplier tubes (PMTs) are mounted in order to detect the scintillation light from neutrino events in the central detector (CD) as well as Cherenkov radiation from the cylindrical water tank in which the central detector volume and its support structure are housed. The high purity water serves both as shielding as well as a veto against external radiation from the surrounding rock. The detector is then capped off with three layers of plastic scintillator decommissioned from the OPERA experiment, covering the area above the central detector and water tank and serving as a top tracker muon veto. A schematic illustration of the JUNO detector can be seen in figure 2.2. The individual components are:

- **The liquid scintillator neutrino target**
  At the heart of the JUNO detector lies the $\varnothing = 35.4\,\mathrm{m}$ wide LS volume. Filled into a 12 cm thick acrylic sphere, the 20 kt detector liquid is made up of highly purified Linear Alkyl Benzene (LAB), a family of organic compounds that exhibit luminescence upon excitation by particles created in neutrino interactions. This scintillator is further enhanced with 2.5 g/L of 2,4-Diphenyloxazole (PPO) and 1 mg/L 1,4-bis(2-Methylstyryl)Benzene (bis-MSB) as wavelength shifters to counteract LS self-absorption. Adding these additional aromatic compounds facilitates an energy transfer from the primary scintillator to the secondary fluorophores, enabling them to emit the scintillation light at higher wavelengths than the LAB normally would and thus shifting the spectrum away from the absorption range of the bulk of the LS material. The low concentration is meant to prevent reabsorption of the scintillation light by the wavelength shifters themselves. Thus, the neutrino detection signal can propagate through the detector largely unobstructed. With such a large detector volume, JUNO requires a high transparency for its LS, with an attenuation length of $\Lambda_{\mathrm{Att}} \geq 20\,\mathrm{m}$, an absorption length of $\Lambda_{\mathrm{Abs}} \geq 60\,\mathrm{m}$ and a scattering length of $\Lambda_{\mathrm{Scat}} \geq 30\,\mathrm{m}$ so that losses in intensity along the light travel path do not significantly impair the signal quality. Furthermore, an LS photon yield of $Y_\gamma \geq 10,000\,\gamma/\mathrm{MeV}$ is expected. The scintillating process, the operation principle of wavelength shifters as well as absorption and scattering effects will be expanded upon in chapter 3. [74]

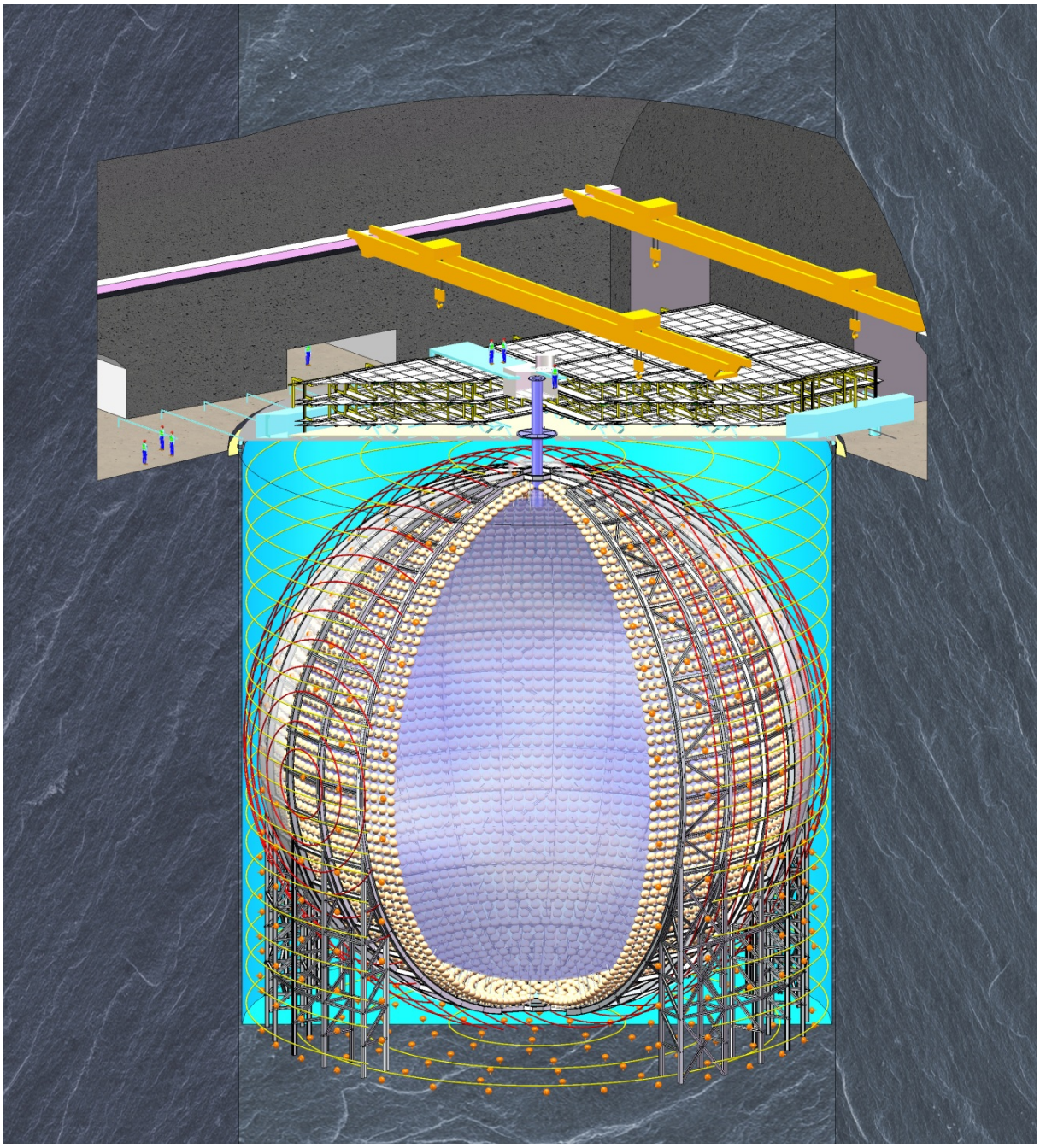

Figure 2.2: A schematic illustration of the JUNO detector. From the center going outwards, the components are: The acrylic sphere filled with liquid scintillator (blue), the inward-facing (beige) and outward-facing (orange) photomultiplier tubes mounted onto the stainless steel lattice shell (silver), the EMF-shielding coils (red and yellow), the water Cherenkov tank (cyan) and the top tracker muon veto (white) on top of the detector.

- **The CD support structure and the photomultiplier tube system**
  The acrylic sphere containing the liquid scintillator is kept in place by a stainless steel support structure. The acrylic itself rests on connecting rods attached to the $\varnothing = 40.1\,\mathrm{m}$ stainless steel lattice shell (SSLS) which in turn is mounted onto a cylindrical truss of 30 pillars attached to the bottom of the outer steel tank. 43,000

inward-facing photomultiplier tubes (PMTs) are attached to the SSLS, divided into 18,000 PMTs of 20" diameter and 25,000 PMTs with 3" in diameter. This amounts to an optical coverage of about 75% in photosensors for the central detector. Taking into account a detection efficiency of 35% for the 20"-PMT system and the aforementioned $10,000\,\gamma$/MeV photon yield of the LS, this is consistent with the energy resolution requirement of $3\%/\sqrt{E[\text{MeV}]}$ for the neutrino MO measurement (c.f. subsection 2.4.1). [74, 75]

- **The water Cherenkov veto**
  The outer water tank serves both as shielding against external radiation such as from the surrounding rock as well as a water Cherenkov veto, with its own PMT system consisting of 2000 20" PMTs, which are also attached to the SSLS, facing outwards. The inner detector is optically separated from the outer water volume, so no signals from either one will affect the other. At a height of $h = 44\,\text{m}$ and with $\varnothing = 43.5\,\text{m}$ in diameter, the tank is filled with 20 kt of ultrapure water, the same amount of LS in the CD. It is also housing a set of solenoid copper coils aligned in such a way as to counteract any effects of the 0.5 Gs earth magnetic field (EMF) that could impact the PMT performance. [74]

- **The top tracker veto**
  The area above the JUNO central detector as well as the water tank will be partially covered by several layers of plastic scintillator plates, obtained from the dismounted OPERA experiment. Each plate comprises four vertical and four horizontal modules for x-y-resolution, which in turn are composed of 64 individual scintillating strips à $6.86\,\text{m} \times 26.3\,\text{mm} \times 10.6\,\text{mm}$. The individual strips are made of Polystyrene with 2% of 1,4-Diphenylbenzene and 0.02% 1,4-bis(5-Phenyloxazol-2-yl)-Benzene (POPOP) as primary and secondary fluours. The strips are coated with a Titanium Dioxide reflective film for improved light collection, and a wavelength-shifting fiber at the center of each strip guides the light to one multi-anode PMT on each end. At 62 plates with a sensitive area of $6.7\,\text{m} \times 6.7\,\text{m}$ stacked in three layers, the JUNO top tracker will cover an area of roughly $940\,\text{m}^2$ above the detector, in order to veto cosmic radiation and its daughter products such as muons or muon-produced neutrons. [74, 76]

2.2 Neutrino Detection Channels

As previously mentioned in chapter 1, when it comes to interaction with other particles, neutrinos are solely subject to the weak force, unaffected by electromagnetism or the strong force. Generally speaking, two distinct reactions are possible: The charged current (CC) interaction is mediated by the exchange of a $W^{\pm}$ boson and transforms the (anti)neutrino into the lepton of its corresponding flavor, while siphoning a negative (or positive) elementary charge off its interaction partner. This reaction has a threshold as the incoming neutrino needs to have sufficient energy to be able to generate the rest mass of the outgoing lepton. The neutral current (NC) interaction on the other hand requires no such energy provision in order to take place, as the neutrino does not convert into a different particle, seeing how the exchanged Z^0 boson only carries energy but no charge.

JUNO's main neutrino detection channel falls into the former category: The so called Inverse Beta Decay[1] (IBD) is a CC interaction that has a neutrino exchange a $W^{\pm}$-boson with a nucleon. The interaction partner depends on the sign of the incoming neutrino's lepton charge: Neutrinos interact with neutrons in order to create negatively charged leptons and a proton while antineutrinos convert into a positively charged lepton by transforming a proton into a neutron.

$$\begin{array}{ccccccc} \nu_l & + & n & \rightarrow & l^- & + & p \\ \bar{\nu}_l & + & p & \rightarrow & l^+ & + & n \end{array} \tag{2.1}$$

For the MO measurement, JUNO relies on the two nearby nuclear power plants which provide a continuous flux of electron antineutrinos, so the signal comprises events following the second line in formula (2.1). The threshold for this reaction is raised to 1.8 MeV, as the neutrino not only needs to carry enough energy to generate the positron rest mass (511 keV), but also needs to provide energy for the mass difference between proton and neutron (1.3 MeV).

The positron then immediately annihilates with a surrounding electron into two gammas, providing a prompt signal after a timespan of a few ps up to ~ 3 ns (depending on the possible production of para- or ortho-positronium before the annihilation). The neutron, ejected from its former nucleus, then thermalizes on the surrounding matter on timescales of $\sim 200\,\mu$s, providing a delayed signal of 2.2 MeV if captured by hydrogen. This energy is determined by the mass defect of the nucleus that absorbs the neutron; capture on carbon for example would yield a delayed energy of 3–5 MeV. It should be noted that the neutron's thermalization time is material-dependent, with the aforementioned number specifically referring to JUNO. The delayed signal is then used to tag IBD events with a delayed coincidence, while the initial neutrino energy is extracted from the energy of the prompt signal.

Using kinematics and neglecting neutron recoil, the neutrino energy can be calculated:

$$\begin{aligned} E_{\bar{\nu}_e} + m_p &= m_n + \overbrace{E_{e^+} + m_{e^+}}^{=E_{\text{prompt}} - m_{e^-}} \\ E_{\bar{\nu}_e} &= \underbrace{m_n - m_p}_{=1.3\,\text{MeV}} - \underbrace{m_{e^-}}_{=511\,\text{keV}} + E_{\text{prompt}} \\ \Rightarrow E_{\bar{\nu}_e} &= E_{\text{prompt}} + 0.8\,\text{MeV} \end{aligned} \tag{2.2}$$

2.3 Radioactive Backgrounds

Energy, timing and also position correlation cuts between prompt and delayed signal are implemented in order to select true neutrino interactions from background events mimicking a neutrino signature. The relevant backgrounds depend on the investigated energy ranges, but generally include accidental coincidences, ^{8}He- and ^{9}Li-decays, fast neutrons and (α, n)-reactions. Also, neutrinos in the same energy range but from different sources are obviously background to each other.

[1] Rarely, the term Inverse Beta Decay is also being used for the electron capture process, where an atom's valence electron is absorbed by a proton in the nucleus, thus producing a neutron and an electron neutrino: $p + e^- \rightarrow n + \nu_e$

Random coincidences occur from natural radiation serving as a prompt event followed by a neutron-like candidate after the characteristic thermalization timescale. The initial event can essentially be provided by any decay from radioisotopes present in the central detector, such as ^{39}Ar, ^{40}K, ^{60}Co, ^{85}Kr, ^{222}Rn, ^{232}Th and ^{238}U amongst other nuclides from their corresponding decay chains or impurities in the detector materials, like dust. The delayed event can then be caused by either one of those very same decays, provided its energy lies in the correct energy range, but additionally also from cosmogenic isotopes or muon-induced neutrons produced in spallation processes.[75] Knowledge about intrinsic radioactivity in the liquid scintillator is thus vital for identifying false coincidences and suppressing background events. To this end, a scintillator radioactivity monitor for JUNO was envisioned and will be covered in-depth in chapter 5, as well as the specific purity requirements in JUNO which serve as the target sensitivity of this detector.

Furthermore, cosmic muons have the possibility to cause correlated backgrounds. For example, interactions with ^{12}C from detector materials, specifically the liquid scintillator, are able to produce ^{8}He or ^{9}Li as daughter isotopes. The initial muon is then correlated in time with the subsequent decay of these nuclides into electrons or neutrons on timescales of several hundreds of milliseconds ($\tau(^{8}\text{He}) = 172\,\text{ms}$, $\tau(^{9}\text{Li}) = 257\,\text{ms}$), thus mimicking an IBD delayed coincidence. [75, 77]

Additionally, high-energy Muons that interact with the materials within the surrounding rock can produce equally high-energetic spallation neutrons. These fast neutrons possess a large interaction length, enabling them to traverse the water pool into the central scintillator volume. A scattering process of such a neutron on a proton would first produce a prompt signal, while its subsequent capture by an atomic nucleus then serves as the delayed signal. [75]

Lastly, some of the isotopes in the aforementioned ^{232}Th and ^{238}U decay chains are α-emitters, which can cause correlated backgrounds via subsequent interactions with the scintillator, specifically ^{13}C. The $^{13}\text{C}(\alpha, n)^{16}\text{O}$ reaction has various possibilities of faking a prompt signal: An alpha capture into an excited state will produce a low-energy neutron, but deexcitation of the oxygen nucleus emits a gamma that can mimic a prompt event. Conversely, if the alpha is captured directly into the ground state, no such gamma will be produced. However, the resulting neutron itself then possesses enough energy to possibly excite a carbon nucleus in the scintillator via inelastic scattering, which in turn will emit a gamma upon deexcitation. Evidently, the delayed signal is then given by the capture of the neutron proper. [75, 78]

2.4 Physics Program

JUNO's cardinal goal is to resolve the open question of the neutrino mass ordering (c.f. section 1.3.3) by investigating the oscillation patterns of two nuclear power plants situated at a medium baseline distance of 53 km to the detector. Additionally, that same neutrino signal can also be investigated to probe various other mixing parameters involved in flavor oscillations (c.f. section 1.5) so as to improve the precision of currently known values. But while primarily reliant on the nearby power plants as a neutrino source for its investigation of the parameter space, JUNO also has an elaborate physics program at the ready in order to investigate neutrino properties from different sources in order to draw conclusions on further-reaching topics.

Given that neutrinos are unaffected by electromagnetism, they can more or less freely propagate through most regions in the universe, such as matter or magnetic fields, that are either opaque to or at least divert other types of messenger. This advantage renders them ideal probes for otherwise inaccessible objects or phenomena. Specifically, in case of an upcoming supernova occurring during its runtime, JUNO intends to examine its neutrino emissions, investigating spectral information and time variation of the different phases. Furthermore, the diffuse supernova neutrino background, an amalgamation of remnant neutrinos from all cosmic supernovae, may be probed as well.

As for more local sources, the Sun provides neutrinos from various fusion processes, which consequentially have different energy distributions, allowing to draw conclusions about the inner workings of the stellar core. Atmospheric neutrinos produced by cosmic rays interacting with the Earth's atmosphere can be measured and may be used as an independent source of information on the MO, as the ones travelling through the Earth undergo MSW-resonance (c.f. section 1.3.2). On the other hand, neutrinos that are directly generated in the Earth's crust or mantle provide valuable information about the chemical composition and dynamic processes under the planet's surface. Finally, the JUNO detector can also be used in order to search for light sterile neutrinos, nucleon decay and partake in indirect searches for dark matter via neutrinos produced in annihilation processes thereof.

2.4.1 Mass Ordering Determination

Contrary to other experiments set out to determine the mass ordering (MO) which usually try to compare different matter effects for neutrinos and antineutrinos, such as T2K[50], NOνA[51], DUNE[52, 53], PINGU[54], ORCA[55] or Hyper-K[56], JUNO pursues a different approach wherein the MO is meant to be determined by a spectral analysis of reactor antineutrinos with a continuous energy distribution between roughly 2–9 MeV. The two reactors in question are located at the Yangjiang nuclear power plant to the southwest of the JUNO detector and the Taishan nuclear power plant to the southeast. All reactors in conjunction are expected to provide 26.6 GW[74] of power by the time JUNO commences operation.

The method in question is based on interplay between Δm^2_{32} and Δm^2_{31} oscillations, that possess similar frequencies and therefore produce interference terms in the oscillation probability. JUNO is situated at a 53 km average distance from the reactor cores, such that the oscillation pattern differs depending on the correct MO (c.f. figure 2.3). In this case, equation (1.22) can be rewritten in such a way to highlight these effects: [75]

$$\begin{aligned} P_{\bar{\nu}_e \to \bar{\nu}_e}(L) = 1 &- \sin^2(2\theta_{12}) c_{13}^4 \sin^2(\Delta_{21}) \\ &- \frac{1}{2}\sin^2(2\theta_{13}) \left[1 - \sqrt{1 - \sin^2(2\theta_{12}\sin^2(\Delta_{21})}\cos\left(2\left|\Delta_{ee}\right| \pm \phi\right)\right]. \end{aligned} \tag{2.3}$$

with the abbreviation $\Delta_{ij} = \Delta m^2_{ij}/4E$. Here the fast oscillation is given by an effective electron mass squared difference

$$\Delta m^2_{ee} = (\cos^2\theta_{12}\Delta m^2_{31} + \sin^2\theta_{12}\Delta m^2_{32}) \tag{2.4}$$

and the oscillation interference is represented by a phase shift that is positive ($+\phi$) for NO and negative ($-\phi$) for IO, with

$$\sin\phi = \frac{c_{12}^2 \sin(2s_{12}^2\Delta_{21}) - s_{12}^2 \sin(2c_{12}^2\Delta_{21})}{\sqrt{1-\sin^2 2\theta_{12}\sin^2\Delta_{21}}}, \quad \cos\phi = \frac{c_{12}^2 \cos(2s_{12}^2\Delta_{21}) + s_{12}^2 \cos(2c_{12}^2\Delta_{21})}{\sqrt{1-\sin^2 2\theta_{12}\sin^2\Delta_{21}}} \tag{2.5}$$

Mind that JUNO investigates antineutrino disappearances whereas equation (1.22) refers to neutrino survivability. In this case both oscillation probabilities are identical, since complex matrix elements only contribute to flavor appearance phenomena (c.f. equation (1.21)) as long as matter effects are sufficiently negligible. However, generally speaking, the respective formulae do not necessarily correspond to one another when switching from neutrinos to antineutrinos or vice versa.

JUNO is going to measure electron antineutrinos at energies between 1.8 MeV and 9 MeV, with the most prominent spectral distortion occurring in the –6 MeV range. The expected spectra as a function of the energy are depicted in figure 2.4. The measured spectrum will be fitted both with the normal as well as the inverted ordering parameters. The true mass ordering will then be discriminated by comparing the χ^2 values of both fits. The quality of the discrimination is given by

$$\Delta\chi^2_{\mathrm{MO}} = |\chi^2_{\mathrm{min}}(\mathrm{NO}) - \chi^2_{\mathrm{min}}(\mathrm{IO})|. \tag{2.6}$$

The optimal sensitivity obtainable with JUNO's $3\%/\sqrt{E[\mathrm{MeV}]}$ and 1% energy uncertainty, after an exposure to 36 GW over six years in the 20 kt LS and assuming an 80% IBD efficiency is estimated to be $\Delta\chi^2_{\mathrm{MO}} \simeq 16$ ($\widehat{=}\, 4\,\sigma$).[74] The averaging of the slightly different core distances to the detector as well as other detector- and reactor-related uncertainties could potentially reduce this value, but a median sensitivity of $\sim 3\,\sigma$ is still achievable.[75]

Furthermore, a complementary analysis is possible, wherein the effective electron mass squared difference from equation (2.4) is compared to additional measurements of the corresponding muon mass squared difference $\Delta m^2_{\mu\mu}$ which complement each other in such a way, that information on the MO can be extracted. It can be shown that:

$$\left|\Delta m^2_{ee}\right| - \left|\Delta m^2_{\mu\mu}\right| = \pm\Delta m^2_{21}\left(\cos(2\theta_{12}) - \sin(2\theta_{12})\sin\theta_{13}\tan\theta_{23}\cos\delta\right) \tag{2.7}$$

where the sign of the right hand side once again depends on the mass ordering, with plus corresponding to NO and minus corresponding to IO. Using this method, the mass ordering sensitivity can be improved up to values of $\Delta\chi^2_{\mathrm{MO}} \simeq 19$ ($4.4\,\sigma$) if the $\Delta m^2_{\mu\mu}$ value is known with a precision of 1%. [75]

2.4.2 Precision Measurement of Oscillation Parameters

Given the detector's distance of 53 km to the Taishan and Yangjiang nuclear power plants, JUNO is in a unique position for neutrino oscillation measurements: Due to the signal shape at this distance for neutrino energies between $\sim$ 2–9 MeV, JUNO will be the first detector capable to observe the slow solar and fast atmospheric oscillation patterns simultaneously. As can be seen in figure 2.4, a dip in neutrinos at 3 MeV is expected to be caused by the θ_{12}-driven solar oscillations, superimposed with a fast-frequency pattern

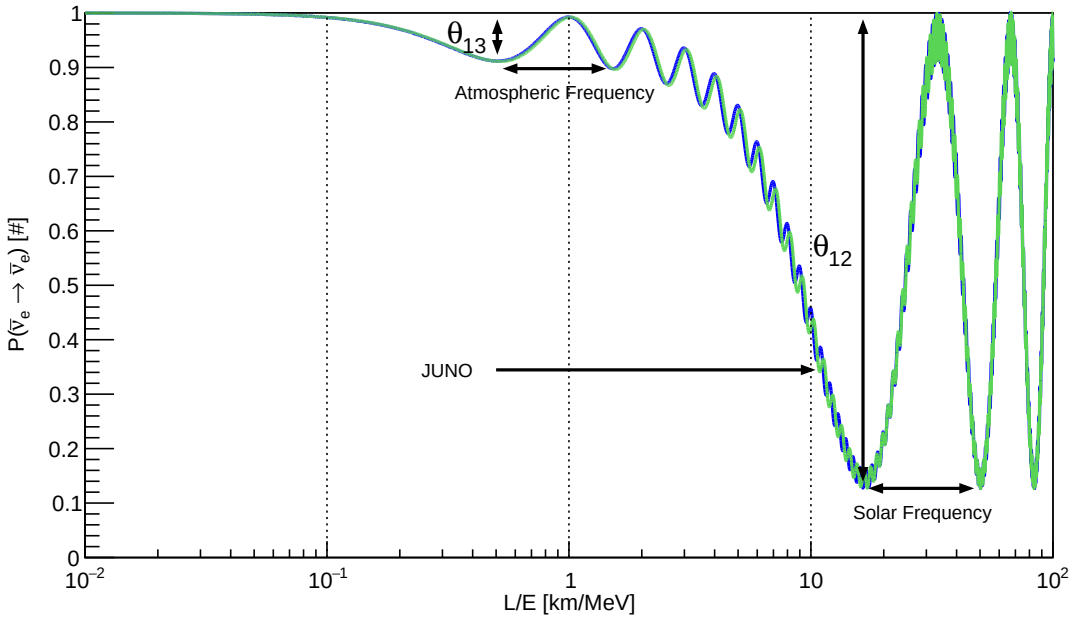

Figure 2.3: The electron antineutrino survival probability versus the ratio of travel path and energy on a logarithmic scale. The fast atmospheric oscillation driven by θ_{13} and the slow solar oscillation driven by θ_{12} are denoted. The approximate position of the JUNO detector (53 km for neutrino energies between 4–6 MeV) is also marked. At this position it is possible to distinguish normal ordering (blue) and inverted ordering (green).

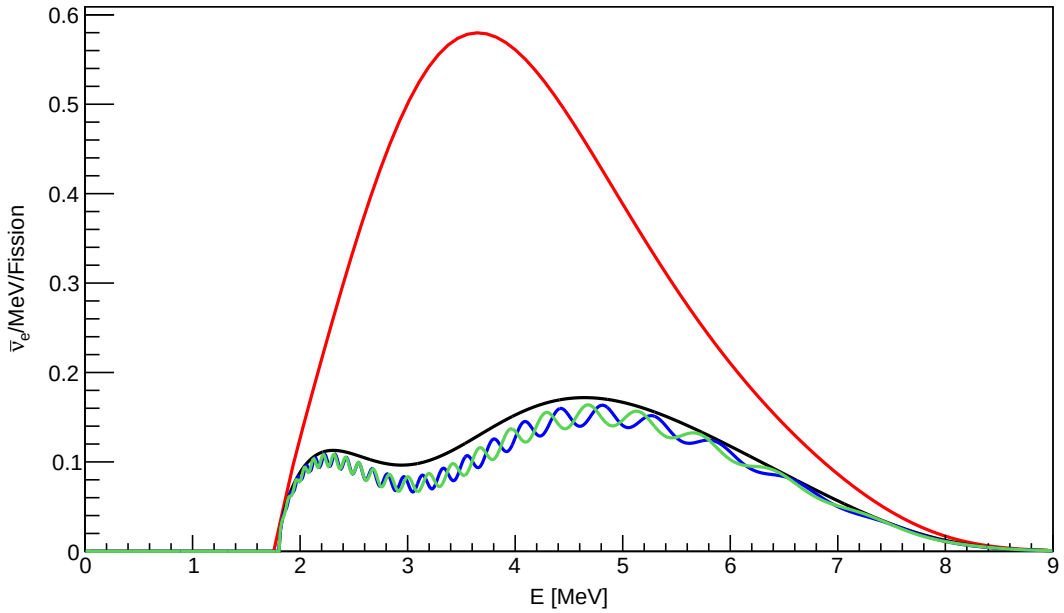

Figure 2.4: The expected electron antineutrino spectra in the case of no oscillations (red), only θ_{12}-oscillation (black) and in the full three-flavor-case for both normal (blue) and inverted ordering (green).

from the θ_{13}-driven atmospheric oscillations. Furthermore, JUNO is going to be the first experiment to observe multiple cycles of said atmospheric oscillations. [75]

As such, JUNO has the ability to probe several neutrino oscillation parameters from both the fast and the slow frequencies. Specifically, the parameters in question are the two mixing angles θ_{12} and θ_{13} as well as the small mass squared difference Δm^2_{21} and the magnitude of the effective electron mass squared difference $|\Delta m^2_{ee}|$ (c.f. subsection 2.4.1).[75] Out of these four, θ_{13} will not be measured to as high a precision as the remaining three, seeing as the distance between detector and neutrino source is not optimized for the solar but rather the atmospheric oscillations.[74] Nevertheless, JUNO intends to determine the other three parameters to sub-percent level precision. Specifically, the values of $\sin^2\theta_{12}$, Δm^2_{12} and $|\Delta m^2_{ee}|$ are expected to be measured with an uncertainty of 0.67%, 0.59% and 0.44% respectively, or better, depending on the impact of the considered systematic uncertainties.[74, 75]

The precision measurement of oscillation parameters can serve as a cross-check for the current understanding of neutrino physics. Precise determination of θ_{12} can confirm or refute the unitarity of the PMNS matrix with a precision of 1.2%, by means of validating or disproving the equation

$$|U_{e1}|^2 + |U_{e1}|^2 + |U_{e1}|^2 = 1 \tag{2.8}$$

thereby shedding further light on the sterile neutrino hypothesis (c.f. section 1.4). Additionally, measurements of Δm^2_{21} and specifically $|\Delta m^2_{ee}|$ have the ability to test the mass sum rule, i.e.

$$\Delta m^2_{21} + \Delta m^2_{31} + \Delta m^2_{32} = 0 \tag{2.9}$$

with an uncertainty of 1.8% which would also point towards new physics if shown to not hold. As mentioned in the previous subsection, the value of $|\Delta m^2_{ee}|$ can then also be used in conjunction with an external measurement of $\left|\Delta m^2_{\mu\mu}\right|$ in a different approach to obtain the neutrino mass ordering. [75]

2.4.3 Further Neutrino Sources

JUNO's extended science program allows it to investigate neutrinos from various sources other than the nuclear reactors providing $\bar{\nu}_e$ for the mass ordering investigation and oscillation parameters precision measurement. This subsection will briefly cover some of the planned neutrino searches and their expected sensitivities.

Supernovae (SNe) have shown themselves in the past to be a high-intensity source of neutrinos and antineutrinos of all flavors and energies. Of particular interest are core collapse supernovae, thermonuclear explosions of stars with masses $M \gtrsim 6\, M_\odot$. These types of events are expected at a rate of 1.9 ± 1.1 SNe per century within the Milky Way.[79] A typical galactic core collapse SN at a distance of $\sim 10\,\text{kpc}$ would lead to about 5000 neutrino events in the JUNO detector, over the course of roughly 10 seconds, across all detection channels. In case of a SN during its runtime, JUNO intends to use these events to collect energy spectra of the different types of neutrinos, thus providing insight into the various stages of a core collapse SN, namely the infall, bounce, accretion and cooling phases. [74, 75]

Similarly, JUNO has the possibility to detect the Diffuse Supernova Neutrino Background (DSNB), which is the combined sum of remnant SN neutrino fluxes across the universe. Given the aforementioned rate for galactic supernovae and taking into account the density of galaxies in the local vicinity, the rate for core collapse SNe lies at $R_{\mathrm{SN}}^{\mathrm{CC}}(z=0) = (1.25 \pm 0.25) \cdot 10^{-4}\,\mathrm{Mpc}^{-3}\mathrm{a}^{-1}$,[80] each producing $\sim 10^{57}$ neutrinos with energies between 5–15 MeV[81]. So far, the DSNB has not yet been detected, and the current upper limit is at $(2.8\text{–}3.1)\,\bar{\nu}_e cm^{-2}s^{-1}$.[82] Detailed measurements of the DSNB could give valuable insight into the average SN neutrino spectra, star formation rate, production of black holes as well as failed SNe. At an expected 1.5–2.9 events per year, spectral analysis will not yet be possible with an detector the size of JUNO, although the general detection is still conceivable, at a significance $> 3\,\sigma$, the exact value depending on the mean spectral energy of the SN neutrinos.[75]

The solar system's central celestial body, the sun, also serves as a neutrino production site. The fusion reactions at its core free up binding energy from the involved nuclei which is then emitted in the form of photons and neutrinos, specifically electron neutrinos. But whereas the photons scatter on the surrounding matter, leading to a diffusion time scale of $t_{\mathrm{d}} = 1.7 \cdot 10^5\,\mathrm{a}$ before they leave the solar outer edge,[83] the neutrinos are able to pass virtually unobstructed. Therefore, solar neutrinos can serve as messengers to study the inner workings of the sun, such as rate and energy distribution of the fusion processes or density distributions (c.f. subsection 1.3.2). The different types of solar neutrinos are named after the respective fusion process they are produced in, which in turn can be sorted into two distinct groups: The so called *pp*-chain contributes 98.4% to the sun's total energy output, while the CNO-cycle accounts for the remaining 1.6%.[84] JUNO could potentially study neutrinos emitted from their constituent reactions and draw conclusions on still sought-after topics, such as the metallicity of the sun (c.f. [85]) and the transition region of the MSW effect, provided a high enough radiopurity of the detector.[74, 75]

Cosmic rays from galactic and extragalactic sources can produce secondary particles after colliding and interacting with the earth's atmosphere. A large part of these secondaries is made up of (anti)neutrinos, generated from production and later decay of atmospheric muons. Depending on their point of origin and the incident angle, these atmospheric neutrinos have different travel paths through the earth before potentially arriving at the JUNO detector and thus are differently affected by matter effects and the MSW resonance. Atmospheric neutrinos can therefore be used as an additional method of investigating the neutrino mass ordering. An optimistic estimate for the MO result assuming 10° angular and $\sigma_{E_{\mathrm{vis}}} = 0.01\sqrt{E_{\mathrm{vis}}/\mathrm{GeV}}$ energy resolution yields $1.8\,\sigma$ after 10 years. Furthermore, atmospheric neutrinos can also serve to investigate CP-violation and measure the atmospheric mixing angle θ_{23}. [74, 75]

The earth itself also serves as a production site for neutrinos as radioisotopes from the Thorium and Uranium chain specifically decay within the planet. Measuring the associated geoneutrino flux and identifying its sources allows to draw conclusions on the chemical composition and layering of the earth's mantle. The nature of earth's internal heat budget can be explored by means of determining the radiogenic heat versus primordial heat via quantifying the emitted geoneutrinos. It is estimated that JUNO will be able to detect roughly 300–500 geoneutrinos per year. [75]

It is further considered to introduce radioactive sources to the vicinity of the JUNO detector in order to search for short baseline oscillations of light sterile neutrinos (c.f. 1.4). Possible isotopes include a ^{144}Ce-^{144}Pr source at the center of or a cyclotron-produced ^{8}Li source close by the detector. Depending on the type and activity of the source, JUNO will be able to determine active-sterile mixing up to a level of 10^{-3} at $5\,\sigma$ C.L. after 5 years on short baselines of $\mathcal{O}(30\,\mathrm{m})$. Additionally, reactor antineutrinos can be used to test a sub-leading effect of active-sterile mixing in the region around $(10^{-5}$–$10^{-2})\,\mathrm{eV}^2$. [74]

With its 20 kt of liquid scintillator, JUNO has a good opportunity to look for nucleon decay processes, specifically proton decay. The chemical composition of the LS results in $1.45 \cdot 10^{33}$ free protons from hydrogen and $5.30 \cdot 10^{33}$ bound protons from carbon. The decay reaction investigated by JUNO is

$$p \;\rightarrow\; K^+ \;+\; \bar{\nu}. \tag{2.10}$$

A proton from hydrogen will decay at rest, resulting in a fixed kaon energy, while a kaon from a carbon decay has a wider range of possible energies in its final state. Either way, the kaon will then subsequently decay with a lifetime of $\tau_{K^+} \simeq 12\,\mathrm{ns}$, allowing for a delayed coincidence tagging. Furthermore, one of the five possible kaon decays with a branching ratio of $R = 84.5\%$ results in a daughter muon that will itself decay into a positron after $2.2\,\mu$s, resulting in a triple coincidence that is a powerful method to reject backgrounds. With the current best limit on this proton decay channel being $\tau(p \rightarrow K^+\bar{\nu}) > 6.6 \cdot 10^{33}\,\mathrm{a}$ as published by the Super-Kamiokande collaboration[86], and considering the number of protons in the JUNO detector as well as backgrounds and detection efficiencies, a non-detection in JUNO could improve the current limit by a factor of three up to a value of $\tau(p \rightarrow K^+\bar{\nu}) > 1.9 \cdot 10^{34}\,\mathrm{a}$. [75]

On a cosmic scale, the existence of dark matter has long been confirmed, from galactic rotation curves, gravitational lensing or the analysis of the cosmic microwave background amongst others. However, detection of dark matter in the lab, both direct and indirect, has so far eluded the scientific community. JUNO has the possibility to investigate dark matter annihilation into SM particles within the sun, i.e. $\chi\chi \rightarrow l\bar{l}$. In particular, JUNO will look for muon neutrino events produced by the dark matter decay channels $\chi\chi \rightarrow \tau^+\tau^-$ and $\chi\chi \rightarrow \nu\bar{\nu}$ while focusing on events with a muon track larger than 5 m inside the detector volume, which allows an angular reconstruction of the track at better than 1°. Under these circumstances, JUNO's $2\,\sigma$ sensitivity after five years reaches $\sigma^{\mathrm{SD}}_{\chi p} = \mathcal{O}(10^{-39}\,\mathrm{cm}^2)$ for the spin-dependent and $\sigma^{\mathrm{SI}}_{\chi p} = \mathcal{O}(10^{-41}\,\mathrm{cm}^2)$ for the spin-independent cross-section at a WIMP mass of $m_\chi = (3$–$20)\,\mathrm{GeV}$. [75]

A detector such as JUNO is a powerful instrument for even more exotic physics searches, that will not be covered in detail here. These include non-standard neutrino interactions, violation of Lorentz invariance as well as CPT invariance, an anomalous neutrino magnetic moment, and other possible scenarios beyond the standard model. Please refer to [75] for more details.

Chapter 3

Scintillators

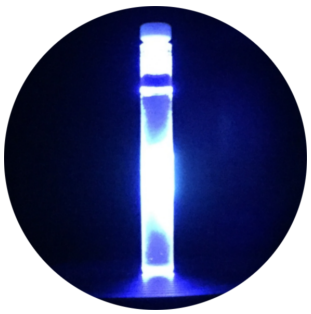

Since neutrinos are uncharged leptons and therefore do not produce any sort of light signal due to their inability to interact with the electromagnetic force (c.f. section 1.1), the general concept for detection involves them interacting with a target material via the weak force, producing daughter particles and then visualizing those in one way or another. Multiple methods are possible for achieving this goal and have led to various fundamentally different types of detectors. This chapter in particular will focus on neutrino detection by the means of liquid scintillators as the active target material, however other methods are also possible:

The original Homestake experiment[12] that first detected solar antineutrinos had them react with liquid chlorine, transforming it into argon, the amount of which would then be manually counted later on. This radiochemical detection procedure was also used in the GALLEX[87] and SAGE[88] experiments. The OPERA experiment[76] used charge-sensitive nuclear emulsion plates to capture the tracks of neutrino reaction daughter particles.

One of the more popular approaches in modern neutrino physics utilizes the Cherenkov effect, wherein a charged particle traveling faster than the phase velocity of light inside the medium – usually water or a similar transparent substance – produces photon emissions in a cone shape, which can be used to draw conclusions on the incident particle. In neutrino detection, this is applied to identify the neutrino-generated electrons, muons and tauons and reconstruct the location, direction and energy of the event. Experiments using this technology include IceCube[89], KamiokaNDE[90] and SNO[91], as well as their various upgrades and successors.

Another common method of visualizing neutrino interactions and the one covered in this thesis is the application of scintillating mediums, specifically liquid scintillators as used in the JUNO experiment, in order to produce luminescence from secondary particles within the detector materials. Other experiments that are based on event detection by induced scintillation light are Borexino[92], Daya Bay[93], KamLAND[94], MINERνA[95], NOνA[96] and RENO[97].

The scintillation process involves excitation of valence electrons of organic molecules – for instance by a charged particle traversing the material – and their subsequent relaxation which produces scintillation light, usually at a characteristic wavelength unique to the scintillator. Detecting the emitted photons allows the reconstruction of the particle position and energy deposition, given sufficient knowledge of the scintillator properties, which in turn makes it possible to infer the properties of the initial particle, such as a

neutrino. The advantages of this technology are a low energy threshold and high photon output which, combined with a well-known energy-to-light-correspondence, allow for a high energy resolution for particle interactions even at small energies. For neutrino detection, the Inverse Beta Decay coincidence channel allows for precise tagging of true events and efficient background rejection.

3.1 The Scintillation Mechanism

While anorganic scintillators usually possess a crystalline structure, organic scintillators such as in the JUNO detector are commonly found in liquid or solid states and mostly consist of Benzene-like ring structures. These rings are formed by means of sp^2-hybridization: In their elemental forms, hydrogen's single valence electron assumes an electron configuration of $1s^1$, while carbon's six valence electrons are distributed as $1s^2\,2s^2\,2p^2$. When both of these elements enter a covalent bond with one another resulting in a Benzene ring, the electron configuration needs to change in order to make all involved electron orbitals energetically equivalent. Therefore, carbon's s- and p-orbitals and hydrogen's sole s-orbital recombine to form three sp^2-hybrid-orbitals and one remaining p-orbital associated with the carbon atom.

The three sp^2-orbitals are aligned in a planar way and form three σ-bonds with 120° angles between each other, two of them connecting to adjacent carbon atoms and the last one attaching the hydrogen atom to the ring. The remaining p-orbital forms a delocalized electron cloud made up of π-bonds above and below the molecular plane. These π-electrons cannot be assigned to one specific atom or location, leading to the resonance structure commonly associated with aromatic compounds. The resulting Benzene ring with its σ- and π-electrons is shown in figure 3.1. [98]

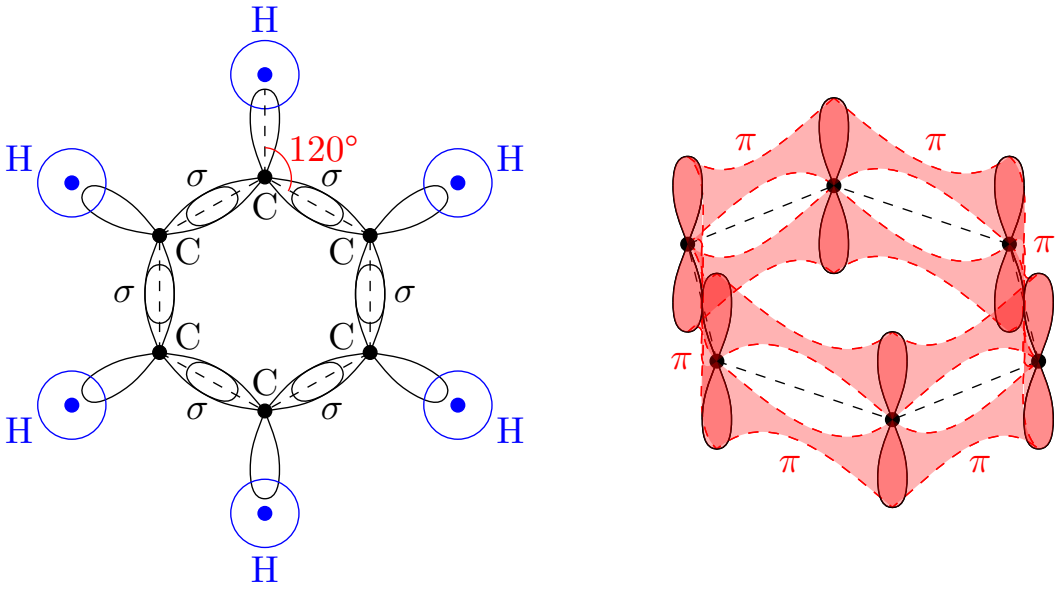

Figure 3.1: Left: A Benzene ring and its σ-bonds seen from the top. Right: The delocalized electron cloud formed by the π-bonds above and below the molecular plane in an isometric perspective. [99]

Scintillation is the process of light emission during the relaxation of valence electrons from molecules that were first excited or ionized by an external energy deposition. The main contribution to said luminescence comes from delocalized π-electrons rather than their σ-bonded counterparts, as the former are more loosely bound compared to the latter, reducing the energy requirement for the initial excitation.

The various possible energy states of molecular valence electrons can be presented in a so-called Jabłoński diagram[100] (c.f. figure 3.2) wherein the ground state S_0 is shown at the bottom, the ionization energy I with the energetic continuum at the top and various discrete states S_i, T_i in between. The nomenclature is motivated by the distinction of two different subsets of states, singlets (S_i) and triplets (T_i). Singlets are defined as those states in which the excited valence electron retains the same spin orientation it had in the ground state, whereas triplet states possess an inverted spin orientation.

Additionally the different electronic excitation levels possess a sub-structure of smaller vibrational levels caused by molecular movement. The energy gap between these vibrational levels is on the order of 0.15 eV while electronic states differ by approximately 3–4 eV (or less, the higher the state).[101] Specifically, the energy difference between the electronic states is such that the emitted photons possess a wavelength in the optical spectrum. It should be noted that according to Kasha's rule, luminescence only stems from the lowest excited electronic states S_1 and T_1 and all other excess energy from both vibrational states or higher-order electronic states dissipates non-radiatively.[102]

While triplet states cannot be populated directly from the ground level, as selection rules for electromagnetic transitions forbid spin-flips, it is possible for an already excited singlet state to convert into a triplet state via intersystem crossing $S_k \to T_k$, which is a non-radiative transition that doesn't violate any selection rules. Additionally, recombination of ionized molecules has a 75% chance of producing a triplet state.[103]

Conversely, while the relaxation of singlet states poses no inherent problem, a direct transition of triplet states to the ground state is equally forbidden. This results in significantly longer timescales for the light emission of triplet state relaxation in the order of $\tau_{\text{ph}} \sim 1\,\mu\text{s}$, dubbed phosphorescence, compared to emissions from singlet states on timescales of $\tau_{\text{fl}} \sim 10\,\text{ns}$, called fluorescence.

Triplet states therefore typically relax by reciprocal interaction with one another, either acquiring enough thermal energy through collisions to reverse the intersystem crossing, allowing for direct fluorescent relaxation, or via interplay with another molecule in the triplet state, yielding one molecule in the ground state S_0 and the other one in an excited singlet state S_1. [104]

3.2 The Wavelength Shifting Process

Although scintillation light is still affected by the Stokes shift, in that its energy does not necessarily correspond to the exact energy gap between the major electronic states due to vibrational sub-levels, it is generally still susceptible to re-absorption because of the overlap between the molecule's continuous emission and absorption spectra. Repeated re-absorption and re-emission of scintillation light however is an undesired effect as it delays the light signal on its way to the photosensors, thereby skewing the timing information while also interfering with the position reconstruction, as the emission direction is not guaranteed to match the initial propagation direction, feigning a false point of origin.

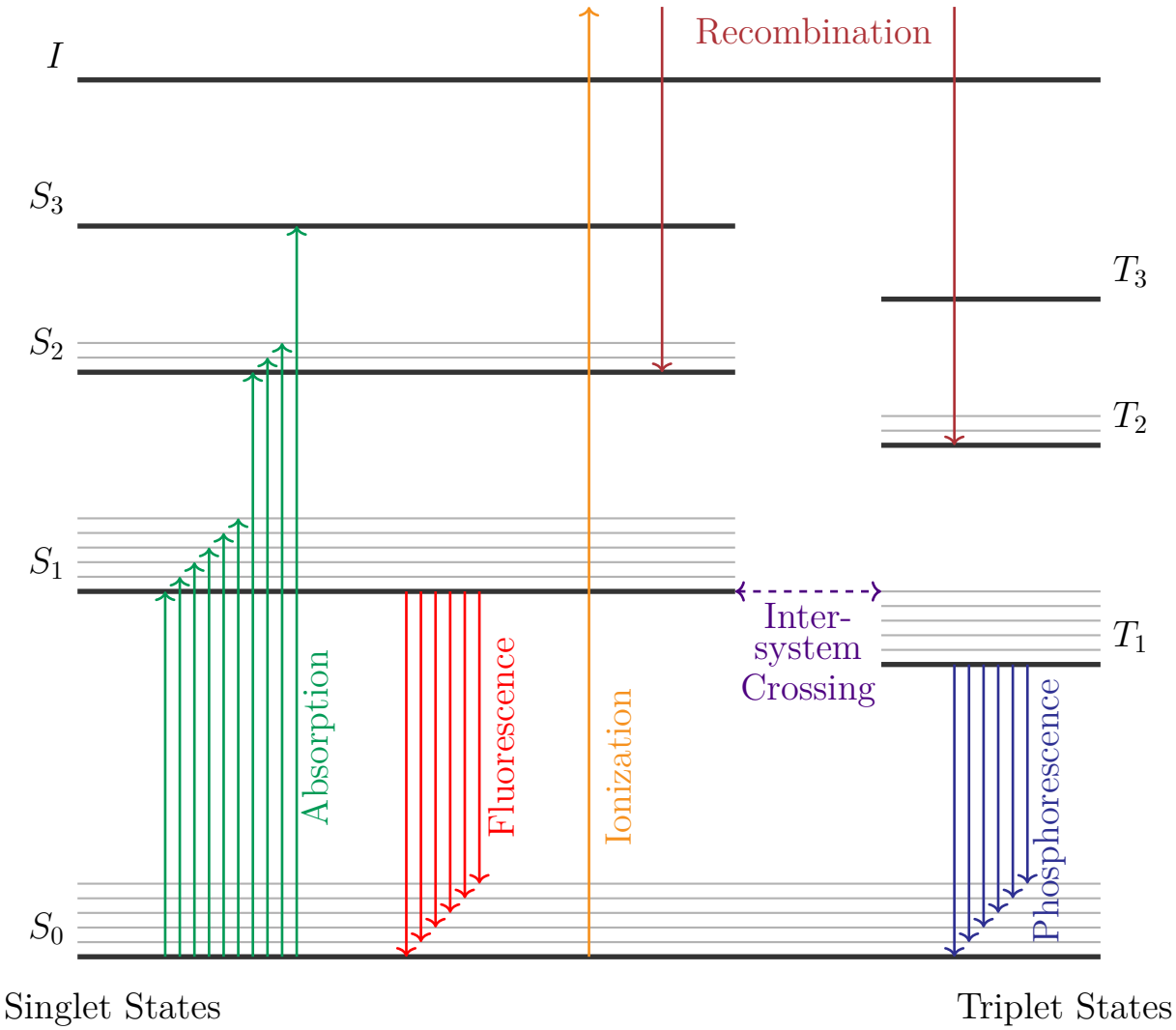

Figure 3.2: Jabłoński diagram of the various molecular energy levels. The thick lines represent the electronic states and the ionization energy on the top, while the thin lines denote the different vibrational states. Also marked are the absorption transitions (green), relaxation due to fluorescence (red) and phosphorescence (blue), ionization (orange) as well as recombination of ionized molecules (brown). Intersystem crossing is represented by the dashed arrow (indigo). Note that while any electronic and vibrational state can be excited, only relaxations from the lowest electronic levels S_1 and T_1 produce luminescence.

In order to counteract such a process, the main scintillator liquid can be enhanced with additional substances that are intended to absorb the initial light emission and shift it further away from the absorption range of the bulk scintillator material. For this reason, these secondary fluorophores are referred to as "wavelength shifters". They are added in such a concentration as to be sufficiently abundant for each primary scintillator molecule to be able to transfer its emission to one wavelength shifter molecule, but sparingly enough so as not to significantly contribute to re-absorption and re-emission effects themselves.

It is also not uncommon to add more than one type of shifter with consecutively further displaced absorption and emission spectra, so that each prior substance emits the light at energies where the subsequent one absorbs. It is thus possible to chain succes-

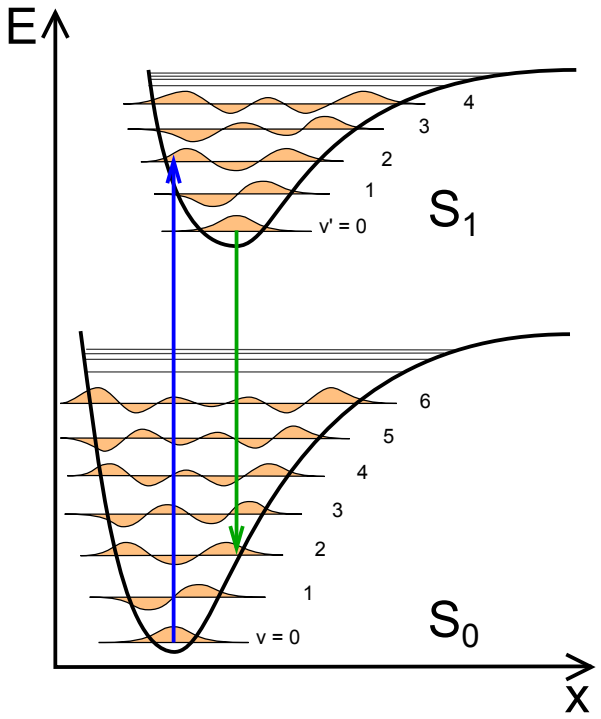

Figure 3.3: Representation of the Franck-Condon-principle within the Morse potential of a two-atomic molecule.[105] The molecule gets excited into an electronic state S_1 and a vibrational state v', the latter of which then immediately decays to $v' = 0$. As the equilibrium position between the atoms is slightly displaced, the electronic state does not relax directly to the ground level S_0, $v = 0$, but to the vibrational state v with the biggest wave-function overlap, thereby releasing a photon with less energy than the initial excitation.

sive shifting processes, thereby moving the wavelength of the signal into a region where the scintillator is virtually transparent. It should be noted that the energy transfer from the primary scintillator to the first wavelength shifter occurs non-radiatively, via FRET (Förster/fluorescence resonance energy transfer, sometimes also Förster transfer)[106] while re-absorption by subsequent shifters is a radiative process.

Wavelength shifters make use of slight changes in the equilibrium states of an excited molecule versus its respective ground level. As mentioned in section 3.1, energetic excitation of valence electrons raises them to a higher level of electronic and vibrational states. While the vibrational energy dissipates immediately by radiationless conversion into phonons, the electronic excitation persists long enough for the molecule itself to be affected. The changed electron configuration shifts the internuclear equilibrium distance of the constituent nuclei making up the larger molecule which in turn also changes the position of the electromagnetic potential the electron is trapped in. [107]

According to the Franck-Condon-principle, electron transitions between excited states are favored, the higher the overlap between the electron's wave function in the two involved states, which is usually a combination of higher electronic and vibrational states due to the shift in the potential location, with the same effect also applying to the relaxation process.[108] A schematic illustration of this principle in the context of a two-atomic Morse potential can be seen in figure 3.3. As vibrational energy dissipates non-radiatively

in both the excited as well as the electronic ground level,[102] a photon absorbed by a wavelength shifter loses energy at least twice, once during electron excitation and then once more during relaxation. After its re-emission, the photon then possesses a higher wavelength than before, determined by the amount of energy lost from its interaction with the wavelength shifter molecule.

Even though a wavelength-shifted photon is able to pass the majority of the scintillator without re-absorption, it is still susceptible to scattering effects which can also affect timing, position and energy reconstruction of signal events. Furthermore, such processes can prolong the travel path of photons through the detector, thus increasing the chance for even more scatterings and once again re-absorption, despite the shifted wavelength. Knowledge on the scattering properties of all scintillator compounds is thus imperative. The various types of scattering processes and their emission profiles with respect to angular and polarization distribution will be covered in chapter 4 along an experimental setup to quantify their relevant parameters.

3.3 Scintillator Constituent Substances

Linear Alkyl Benzene

Linear Alkyl Benzene (LAB) refers to a family of scintillator compounds that possess a similar structure formula but differ in the length of the carbon chain (c.f. table 3.1). It makes up the bulk of the JUNO liquid scintillator. LAB is a liquid at room temperature.

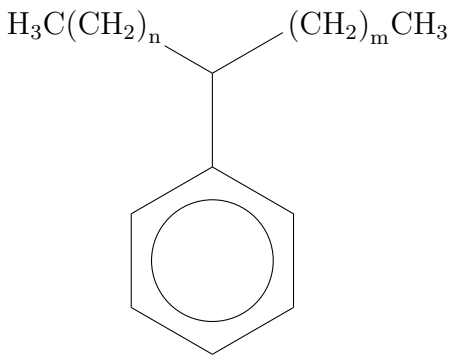

Figure 3.4: Structural formula of LAB. [109]

Name	Linear Alkyl Benzene
Abbreviation	LAB
Molecular formula	$C_9H_{12}(CH_2)_{n+m}$, n + m = 7–10
CAS-number	67774-74-7
EC-number	267-051-0
Density	0.857 kg/l
Absorption maximum	260 nm
Emission maximum	282 nm

Table 3.1: Relevant chemical and physical properties of LAB. [109]

PPO

2,5-Diphenyloxazole is used as the primary wavelength shifter in the JUNO scintillator. PPO is solid at room temperature and usually comes in the form of a greenish powder.[110]

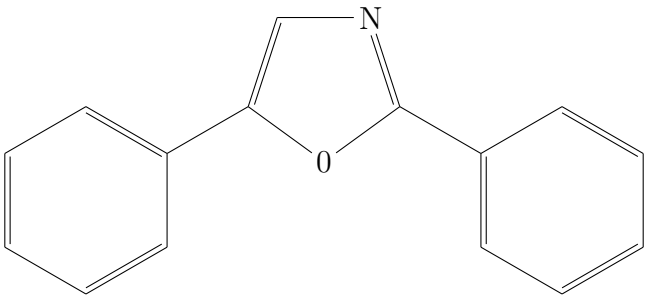

Figure 3.5: Structural formula of PPO. [110]

Name	2,5-Diphenyloxazole
Abbreviation	PPO
Molecular formula	$C_{15}H_{11}NO$
CAS-number	92-71-7
EC-number	202-181-3
Absorption maximum	302 nm
Emission maximum	343 nm

Table 3.2: Relevant chemical and physical properties of PPO. [110]

bis-MSB

1,4-bis(2-Methylstyryl)Benzene is another wavelength shifter that is used as a secondary fluor in conjunction with PPO. bis-MSB is crystalline under standard conditions and possesses a slight yellow tint.[111]

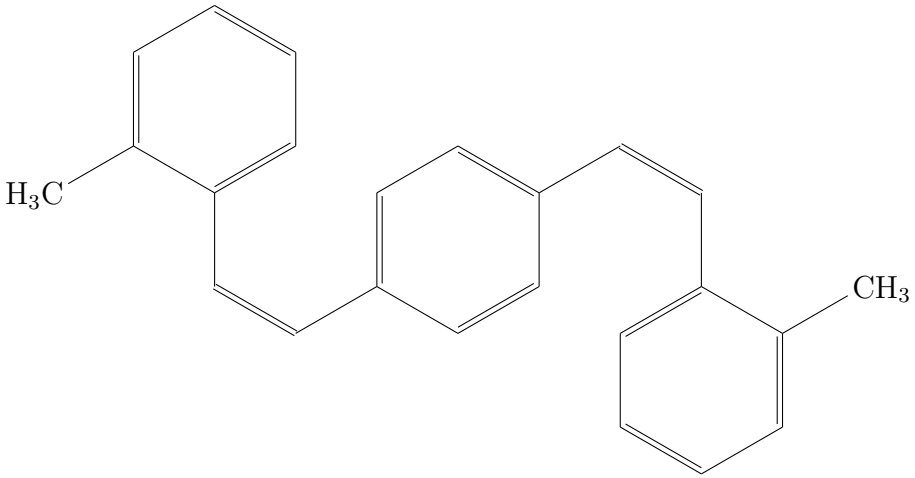

Figure 3.6: Structural formula of bis-MSB. [111]

Name	1,4-bis(2-Methylstyryl)Benzene
Abbreviation	bis-MSB
Molecular formula	$C_{24}H_{22}$
CAS-number	13280-61-0
EC-number	236-285-5
Absorption maximum	345 nm
Emission maximum	420 nm

Table 3.3: Relevant chemical and physical properties of bis-MSB. [111]

Cyclohexane

Not a scintillator itself, as it lacks the Benzene ring, Cyclohexane is a colorless liquid at room temperature whose absorption and emission spectra lie in the near ultraviolet ranges. It is therefore useful as a solvent for scintillators that absorb and emit in the visible range, as it doesn't interfere with the light propagation. In this thesis, it is also used as an index-matching liquid and also calibration sample in the Rayleigh scattering measurement setup (c.f. section 4).

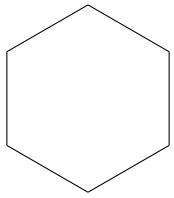

Figure 3.7: Structural formula of Cyclohexane. [112]

Name	Cyclohexane
Molecular formula	C_6H_{12}
Density	0.779 kg/l
CAS-number	110-82-7
EC-number	203-806-2
Absorption maximum	< 150 nm
Emission maximum	201 nm

Table 3.4: Relevant chemical and physical properties of Cyclohexane. [112, 113, 114]

Chapter 4

Rayleigh Scattering

In large-scale liquid scintillator (LS) detectors, the light usually has a travel path in the order of tens of meters before it gets detected by the photomultiplier tubes (PMTs) mounted on the edge of the active detector vessel. In the case of JUNO, this is a $\varnothing = 40.1\,\mathrm{m}$ wide support structure outside of the $\varnothing = 35.4\,\mathrm{m}$ large acrylic sphere carrying the 20 kt of Linear-Alkyl-Benzene-based (LAB) liquid (c.f. section 2.1). A major concern is for enough light to actually reach the photosensors in order to produce a sufficiently strong signal that can then be evaluated. Typical scintillator light yields are roughly $10^4\,\gamma/\mathrm{MeV}$ (photons per MeV), for example the Borexino scintillator composed of PC (1,2,4-Trimethylbenzene or Pseudocumene) and 1.5 g/l PPO (2,5-Diphenyloxazole) was measured to produce $11,500\,\gamma/\mathrm{MeV}(\pm 10\%)$.[115] A similarly high light yield is expected within JUNO, which would translate to $1,200\,\mathrm{p.e./MeV}$ induced within the surrounding PMTs. This number was obtained by scaling Daya Bay calibration measurements with 1 MeV gammas to the JUNO detector size. Losses stem from gaps in the geometrical coverage, PMT sensitivities as well as absorption and scattering effects in the surrounding material.

As mentioned in the previous chapter, the transparency of the LS can be increased by admixing additional fluorophores that re-emit absorbed light outside of the primary component's absorption spectrum, thereby reducing scintillator self-absorption. Furthermore, the wavelength-dependent quantum efficiency (QE) of the PMTs has to be taken into account, as the light needs to be shifted to a wavelength that the photocathode is sensitive to. PMTs used in LS detectors usually have a peak performance at around $\sim 400\,\mathrm{nm}$, with their QE reaching up to 30%, while light in the scintillator propagates at roughly 430 nm. The total emission spectrum for the JUNO mixture can be seen in figure 4.1 while the QE curves of the two types of PMTs used in the JUNO detector (dynode and microchannel plate PMTs) are shown in figure 4.2. Additionally, the collection efficiency and optical coverage of the PMTs affects how much light is actually detected due to photons reflecting off the bulb glass or simply not hitting a PMT. While not in use within JUNO, given the already rather high optical coverage of $> 75\%$, some experiments employ light concentrators such as Winston cones to increase these numbers.

However, the scintillation light does not necessarily follow a straight path on its way from the event vertex to the photosensors, but is severely affected by absorption and scattering effects within the scintillator itself. While wavelength shifters mitigate the re-absorption in the main LS component, they themselves still have a probability of being excited by their own emission light. Furthermore, the propagating light is still susceptible

to scattering effects off of materials within the LS mixture. Losses in collected light impair the correct determination of the initial particle's energy, while scattering both changes the direction of the signal photons as well as their travel time, which affects position and timing reconstruction. It is thus vital to know the relevant parameters in order to reliably evaluate the data collected from the scintillation light by the PMTs.

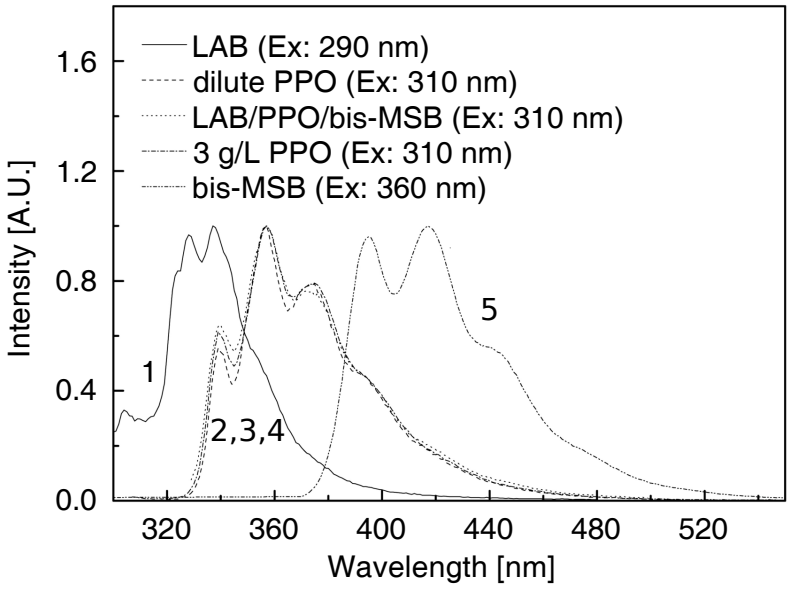

Figure 4.1: Emission spectra of the various compounds (LAB, PPO, bis-MSB) that make up the JUNO scintillator. [116]

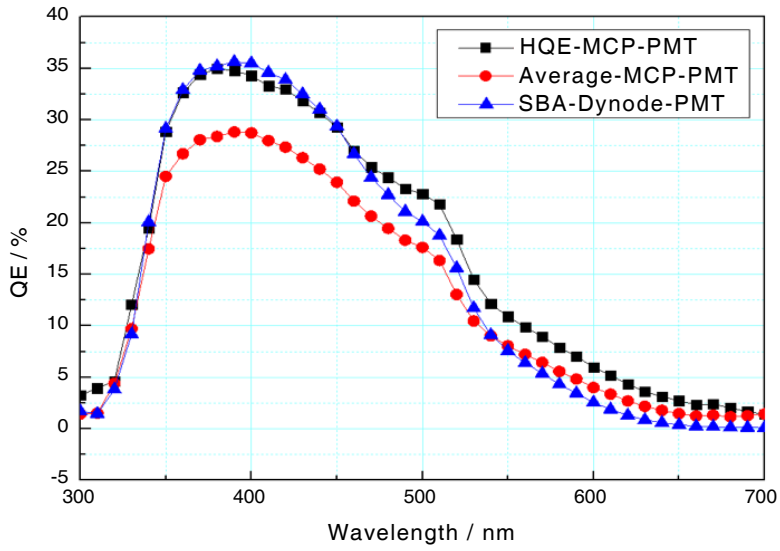

Figure 4.2: Quantum efficiencies of the JUNO High-Quantum-Efficiency and Average Microchannel Plate Photomultiplier Tubes (HQE-MCP-PMT, Average MCP-PMT) and the Super-Bialkali Dynode Photomultiplier Tubes (SBA-Dynode-PMT) between 300 nm and 700 nm. [117]

4.1 Scattering Processes

In general, optics distinguishes between three major categories of electromagnetic scattering: If the size of the particle is significantly smaller than the wavelength of the incident light, the process is categorized as *Rayleigh scattering*. Increasing the particle size to be in the same order of magnitude as the photon wavelength will yield so-called *Mie scattering*. Lastly, scattering of light off objects a lot larger than its wavelength will just follow geometrical optics and can hence be called *geometrical scattering*.

It should be noted that this distinction – specifically between Rayleigh and Mie scattering – is not exact due to overlapping applicability of the two mathematical descriptions and the terminology is also cause of some dispute, both for its historical correctness as well as disagreements in definitions across different fields.[118, 119] However, for the sake of brevity, it will be the nomenclature used from here on out. Furthermore, this thesis will also consider absorption and reemission of light by the surrounding material – specifically scintillator and wavelength shifters – as a type of scattering, since it also changes the incident light's propagation direction.

The impact of scattering on the light propagation is usually quantified by characteristic parameters specific to the medium and the type of process investigated. These parameters are determined via the Beer-Lambert-law, which describes exponential extinction of light within a medium:

$$I(x) = I_0 \cdot \exp\left(-\frac{x}{\Lambda_{\text{Att}}}\right) \tag{4.1}$$

The attenuation length Λ_{Att} gives the distance light can propagate until $1/e$ of the initial intensity is lost. Similarly, specific lengths can be given for each involved process as to how far light can travel until the same relative amount would be lost due to that particular interaction:

$$\frac{1}{\Lambda_{\text{Att}}} = \frac{1}{\Lambda_{\text{Abs}}} + \underbrace{\frac{1}{\Lambda_{\text{ARe}}} + \frac{1}{\Lambda_{\text{Ray}}} + \frac{1}{\Lambda_{\text{Mie}}}}_{1/\Lambda_{\text{Scat}}} \tag{4.2}$$

The indices here denote the different types of attenuation processes, with the last three being classified as scattering. Furthermore, light can also be absorbed and its energy dissipated non-radiatively, quantified by the absorption length Λ_{Abs}. While the attenuation length and the scattering length can be measured directly, the absorption length cannot, wherefore it has to be calculated from formula (4.2) by knowing all other parameters. This is particularly important, as scattered light will still be detected in a detector and thus contribute to the signal, while dissipated light is completely lost and thus skews the information to be obtained for the particle energy. Within JUNO, the goal is an attenuation length of 20 m with a scattering length of 30 m and an absorption length of 60 m at 430 nm.

For light traversing the JUNO detector, geometrical scattering is relevant only on boundary layers such as the acrylic sphere (c.f. section 2.1) but not within the liquid scintillator itself. Similarly, Mie scattering requires targets of sufficient size compared to the $\mathcal{O}(400\,\text{nm})$ light, such as dust particles inside the detector liquid. Assuming the scintillator is sufficiently purified before filling, such a contribution will not occur and

Mie scattering can be neglected as well. This leaves only Rayleigh scattering and absorption/reemission as relevant scattering processes within the JUNO liquid scintillator, with the former being by far the larger contribution. Thus, the second and fourth term in equation (4.2) can be neglected and Λ_{Scat} is directly identified with Λ_{Ray}.

Rayleigh scattering is highly angular-, polarization- and wavelength dependent. In particular, the total intensity of scattered light can be split into the contributions of the component polarized parallel and perpendicular to the respective scattering plane:[120]

$$I(\theta) = I_{\parallel}(\theta) + I_{\perp}(\theta) \tag{4.3}$$

For totally unpolarized incident light, the angular dependency of the individual contributions can be described according to:[120]

$$\begin{aligned} I_{\parallel}(\theta) &= \frac{\cos^2(\theta)}{2} A + \frac{1}{2} B \\ I_{\perp}(\theta) &= \frac{1}{2} A + \frac{1}{2} B \end{aligned} \tag{4.4}$$

Since the incoming light will induce a dipole oscillation in the scattering target, the emitted radiation will have a minimum at 90° if the dipole lies within the scattering plane (i.e. it was excited by the parallel component of the incident light) or be constant over all angles if the dipole is oriented orthogonal to the scattering plane (i.e. excitation by the perpendicular component of the incident light). For an ideal Rayleigh scatterer, this would be an exact $1 + \cos^2\theta$ distribution, however since the molecules of the scintillator have a finite size there is a nonzero scattering contribution at 90° even from the parallel component. The extent of this deviation from the ideal distribution can be described by the depolarization ratio:

$$\delta = \frac{I_{\parallel}(90°)}{I_{\perp}(90°)} = \frac{B}{A + B} \tag{4.5}$$

In liquids specifically, Rayleigh scattering is usually caused by density fluctuations and thus a fluctuation in the polarizability of the material. These fluctuations can be treated as individual Rayleigh scatterers embedded in an otherwise homogeneous medium. Albert Einstein and Marian Smoluchowski (among others) developed a theory to quantify these processes.[121] Their formula was later expanded to include the previously mentioned depolarization by Jean Cabannes[122] which then in turn was corrected by Louis V. King[123]. Still, for reasons lost over time, the final correction inherited the title "Cabannes anisotropy factor"[118] and the resulting equation is now known as the "Einstein-Smoluchowski-Cabannes-formula":[120]

$$\Lambda_{\text{Ray}} = \left\{ \frac{8\pi^3}{3\lambda_0^4} \left[\rho \left(\frac{\mathrm{d}\epsilon}{\mathrm{d}\rho} \right)_T \right]^2 kT\beta_T \left(\frac{6 + 3\delta}{6 - 7\delta} \right) \right\}^{-1} \tag{4.6}$$

Here, δ refers to the aforementioned depolarization ratio, k is the Boltzmann constant, T the temperature and β_T the isothermal compressibility. As λ_0 is the wavelength of the scattered light, it is easy to see that longer wavelengths will be less Rayleigh-scattered, according to the fourth power. The final factor is usually approximated with an empirical

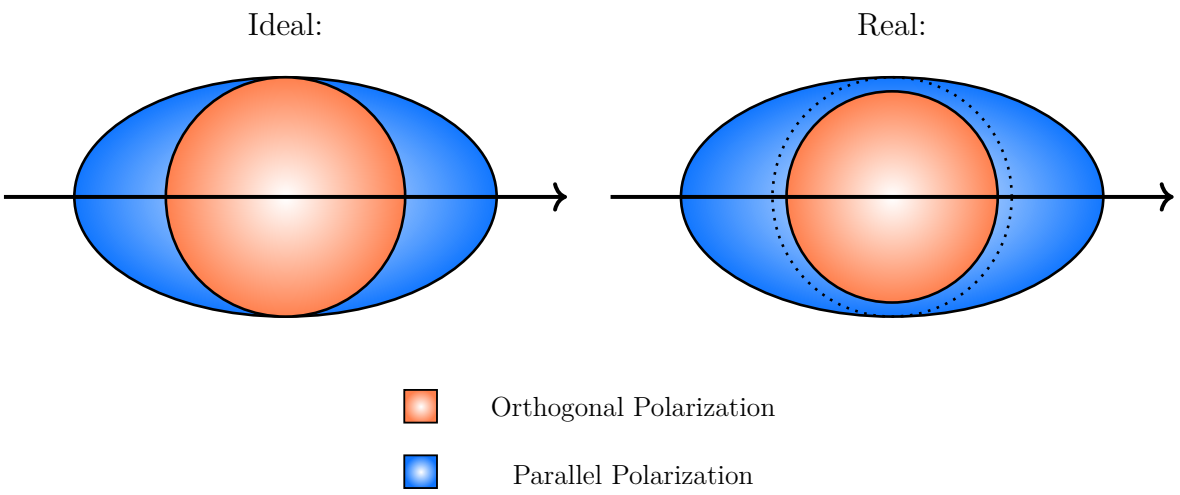

Figure 4.3: Qualitative Rayleigh scattering intensity distribution for an incident beam of light coming from the left, for an ideal ($\delta = 0$, left) and a real scatterer ($\delta \neq 0$, right).

formula containing the refractive index n. Several approximations exist, but the best agreement is reached with the Eykman approximation:[124]

$$\rho \left(\frac{\mathrm{d}\epsilon}{\mathrm{d}\rho} \right)_T \simeq \frac{2n(n+0.4)(n^2-1)}{2n(n+0.4)-(n^2-1)} \tag{4.7}$$

In theory, measuring the depolarization ratio δ and knowing all other properties is sufficient to calculate the Rayleigh scattering length. However, a direct measurement of Λ_{Ray} is also possible and is the approach that will be shown in this thesis.

4.2 Experimental Setup

In order to experimentally determine the Rayleigh scattering length of liquid scintillator samples, a laboratory setup was assembled that would allow for wavelength-, polarization- and angular-dependent measurements. Polarized light of a fixed wavelength is guided through a liquid sample and undergoes Rayleigh scattering within. Two photomultipliers observe the throughgoing intensity as well as the polarization-dependent intensity scattered under a certain angle, in this thesis 90°. A sketch of the experimental design can be seen in figure 4.4.

The entire setup has been placed onto an optical table inside of a temperature-stable dark room. A 100 W quartz-tungsten halogen lamp (Oriel APEX2-QTH) serves as a light source with a continuous spectrum. A monochromator (Oriel Cornerstone 260) is then used to choose a specific wavelength. The emerging light is subsequently collimated using two irises (Thorlabs SM1D12D) with a wire-grid polarizer (Thorlabs WP25M-VIS) in between to select the vertical component. This beam is then focused using an achromatic lens doublet (Thorlabs ACA254-200-A) onto a liquid sample in $\sim 20\,\mathrm{cm}$ distance. The cylindrical cuvette holding the sample is immersed into a larger custom made vat (Hilgenberg, Boro 3.3, $\varnothing = 30\,\mathrm{cm}$, $d = 5\,\mathrm{mm}$) filled with Cyclohexane as an index-matching liquid. On the other side of the vat, the beam passes through a neutral density filter with optical density 5.0 (Thorlabs NE50B-A) that reduces the beam intensity by a known amount to

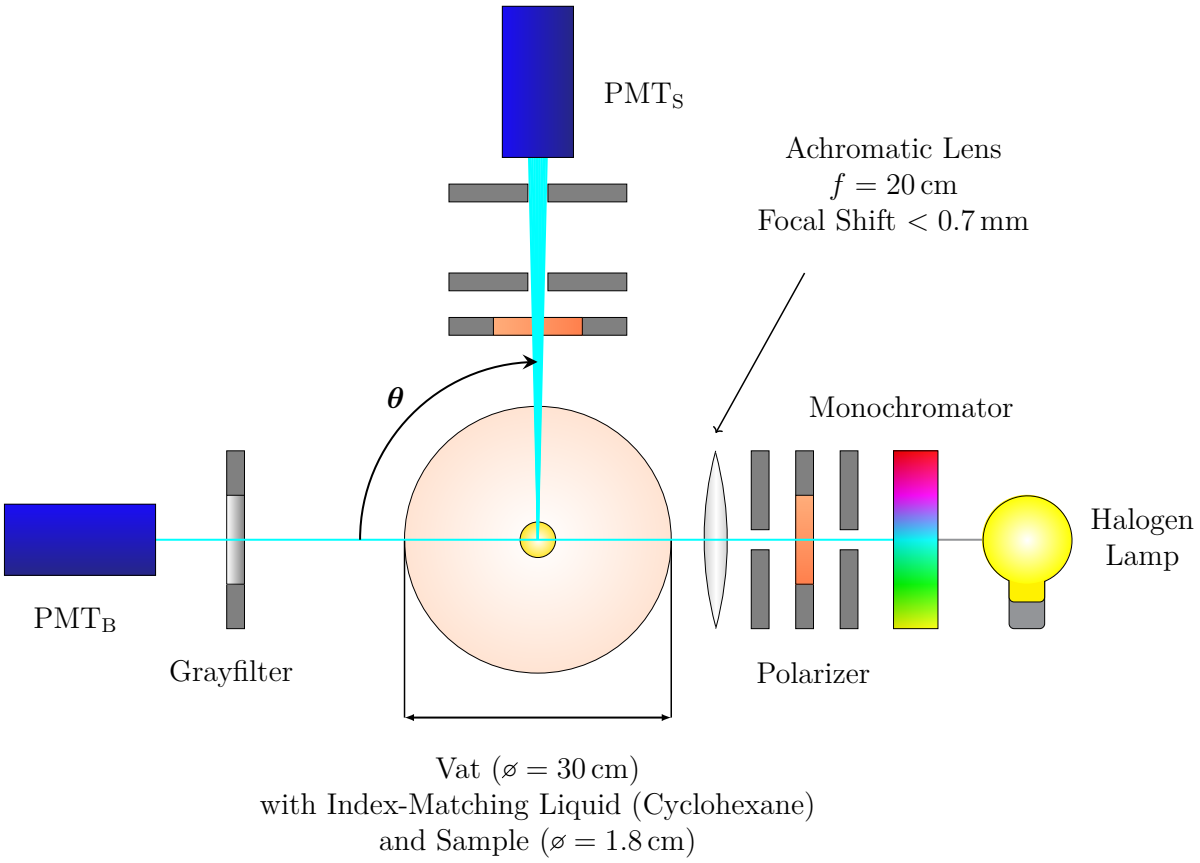

Figure 4.4: Sketch of the Rayleigh scattering setup: Light from a halogen lamp passes through a monochromator and is then collimated, vertically polarized and focused onto a sample within a larger vat filled with index-matching liquid. A photomultiplier shielded by a neutral density filter monitors the beam intensity while a second PMT at 90° measures the scattered light of a certain polarization within a solid angle selected by two optical slits.

protect the adjacent PMT (Hamamatsu R9980 K-ASSY) from overexposure while monitoring the lamp for reference. At 90° perpendicular to the beam path, an identical photomultiplier is placed to measure the scattered light intensity. The solid angle under which it operates is determined by two slits (Thorlabs VA100/M) in front of which another polarizer of the aforementioned type preselects the vertical or horizontal component of the scattered light. A photo of the final setup is shown in figure 4.5.

Of particular interest is the larger vat in which the sample is submerged, which was implemented in order to provide a low surface curvature within the beam's area of impact, thus reducing refraction of the incident light. At the same time only a small sample volume is required rather than filling the whole vat with the sample liquid, since the scatter-PMT only monitors a narrow part of the beam passing through the center of the geometry. Instead, the empty volume in between the vat and the cuvette holding the sample is filled with a liquid whose refractive index matches the surrounding materials as close as possible, thereby minimizing further unwanted reflection or refraction within the setup. This liquid was chosen to be cyclohexane (CHX), both for its agreeable refractive index and its low scattering properties. A list of the involved materials and their refractive indices is shown in table 4.1. A demonstration of the index-matching by comparing the vat filled with water compared to Cyclohexane is shown in figure 4.6.

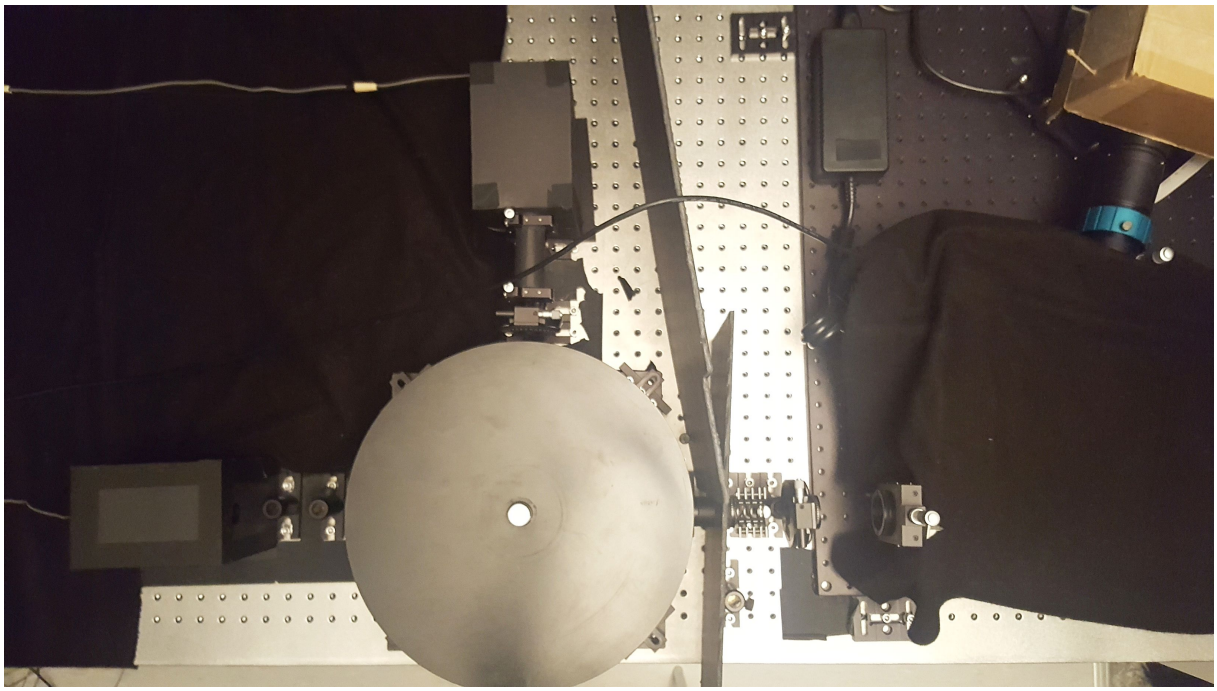

Figure 4.5: A picture of the finalized experimental setup. From right to left: Lamp (top right); monochromator (bottom right); polarizer with pinhole screwed on; lens tube with achromatic doublet and pinhole screwed on (going through the cardboard wall); Cyclohexane-filled vat with black lid and cuvette holding the sample in the middle (white); PMT with grayfilter in front (bottom left, under cardboard box). Above the light path sits another PMT (top center, under cardboard box) with two optical slits and another polarizer (middle center). Large parts of the optical table as well as some instruments were covered with cloth to reduce reflective surfaces.

With both PMTs' data read out simultaneously via an external trigger and a known solid angle imposed by the fixed geometry, the intensity measured by $\mathrm{PMT_S}$ (scat) can be used to extrapolate to the total amount of scattered light over 4π, which then in turn can be compared to the monitored beam intensity provided by $\mathrm{PMT_B}$ (beam) in order to calculate the overall scattering properties of the sample in question. The full process of data-taking including the trigger logic and implemented software will be detailed further in section 4.3, while the analysis procedure is explained in section 4.5.

The setup is designed to be upgradeable specifically with respect to angular coverage. Possible extensions include more PMTs at additional angles and/or a curved rail for moving PMTs to specific angles at non-fixed positions. Such a multi-angle measurement would allow for obtaining Rayleigh parameters from fit values instead of calculations, though this stage of the experiment has not yet been achieved within the scope of this thesis.

n_{H2O}	n_{CHX}	n_{Vat}	n_{Cuv}	n_{LAB}
1.341	1.426	1.473	1.467	1.496

Table 4.1: Refractive indices of the materials used within the setup, as provided by the manufacturers. For reference, the index of water is given as well.

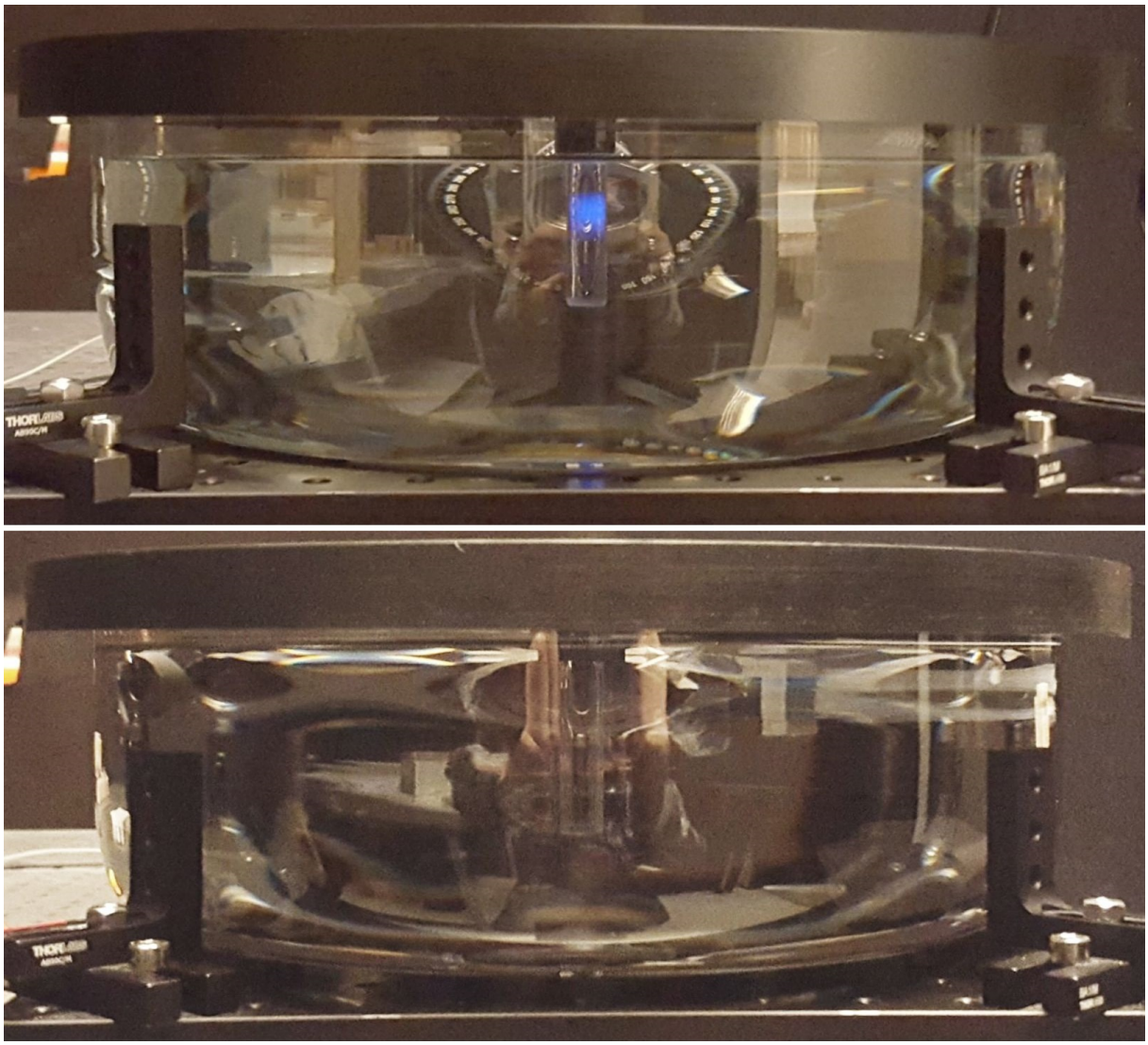

Figure 4.6: A comparison of the vat filled with water (top) versus Cyclohexane (bottom) demonstrating the index-matching effect. Note how the outlines of the cuvette (center) are more sharp in water and blurry in cyclohexane. The top picture also shows the height and diameter of a horizontal light beam crossing the setup from right to left.

4.3 Photomultipliers and Data Acquisition

The optical sensors used in the Rayleigh experiment to measure both the scattered light as well as provide a reference of the beam intensity are photomultiplier tubes (PMTs). A popular device for photon detection in particle and especially neutrino physics, PMTs are capable of converting incident light into an electronic signal that can be visualized and quantified by oscilloscopes or analog-to-digital-converters (ADCs).

A photomultiplier is essentially an evacuated tube with a glass window on one end. Different types of glass can be used which vary with respect to transmittance for various wavelengths, so the ultimate choice of material depends on the intended application. For the Hamamatsu R9980 K-ASSY PMTs used in the Rayleigh experiment, the window is made from borosilicate. The glass is coated from the inside with a vapor-deposited film

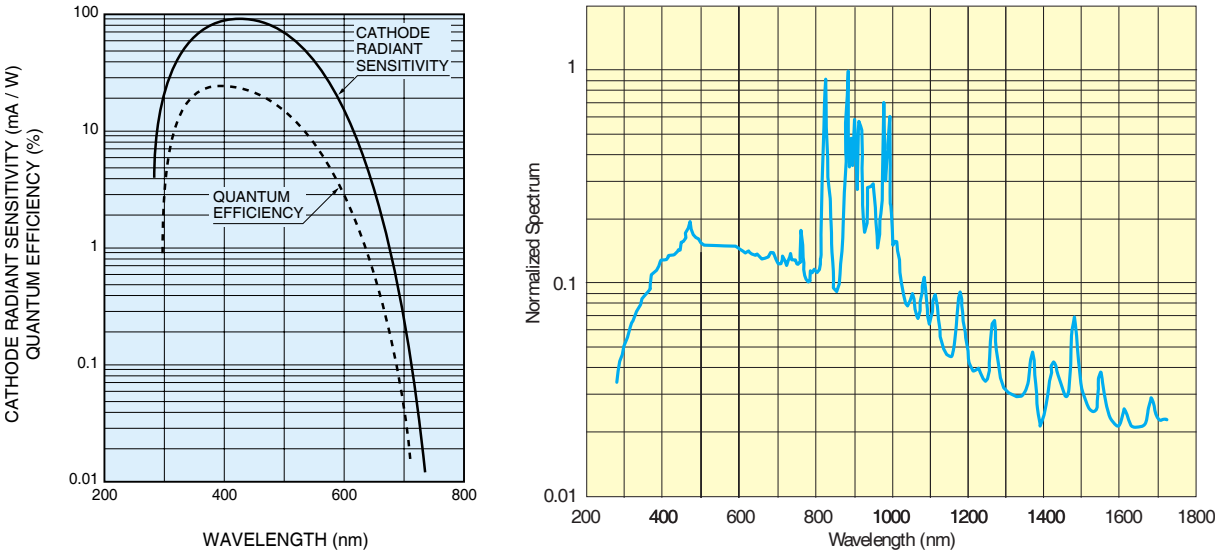

Figure 4.7: The wavelength sensitivity of the PMT (left)[125] and the intensity spectrum of the halogen lamp (right)[126] used in the Rayleigh scattering experiment.

of semiconductor, the so called photocathode. Incoming light excites electrons from the valence band such that they are ejected into the vacuum via the photoelectric effect. Once again, many types of materials are available with various sensitivity ranges, but they are all designed to have a low work function, so that no photons are lost if their energy is too small to raise electrons to the vacuum level. On the other hand, a low energy gap also means that thermionic emission from the semiconductor can cause false signals referred to as "dark current". The PMTs used in this experiment possess a bialkali photocathode (Sb-Rb-Cs, Sb-K-Cs). For reference, the PMT sensitivity is shown next to the halogen lamp spectrum in figure 4.7. The free electrons are then accelerated by an external electric potential difference onto an electron multiplier dynode, where treir accumulated kinetic energy transfers to a dynode electron, releasing it via secondary emission. This process is then repeated over several more dynodes, with each subsequent stage increasing the number of free electrons. Lastly, the showering electrons are then collected at the PMT anode where they produce a voltage signal. The total gain depends on the number of dynode stages as well as the applied voltage. The R9980 possesses ten stages and is herein operated under $-1.5\,\mathrm{kV}$ provided by a high voltage module (iseg DPR 20 605 24 5) which amounts to a total gain of $2 \cdot 10^6$. Note that PMTs are specifically designed for either positive or negative supply voltage, which determines which end is grounded (photocathode or anode, respectively). The Rayleigh scattering PMTs are supplied with a negative high voltage, which produces faster signals but has a higher dark current. Figure 4.8 shows a sketch of a typical photomultiplier in cross-section with the important components marked and labeled. [127, 125]

The analog signals relayed by the photomultipliers are subsequently digitized using a desktop ADC (Caen DT5751) that is connected via USB to a PC running `LabVIEW`-based data acquisition software. While the ADC provides four inputs that can be used independently, it was so far used in Double Edge Sampling (DES) mode, interleaving two adjacent channels to double the sampling rate to $2\,\mathrm{GS/s}$. However, using all four channels is an option for potentially upgrading the Rayleigh experiment with additional PMTs at

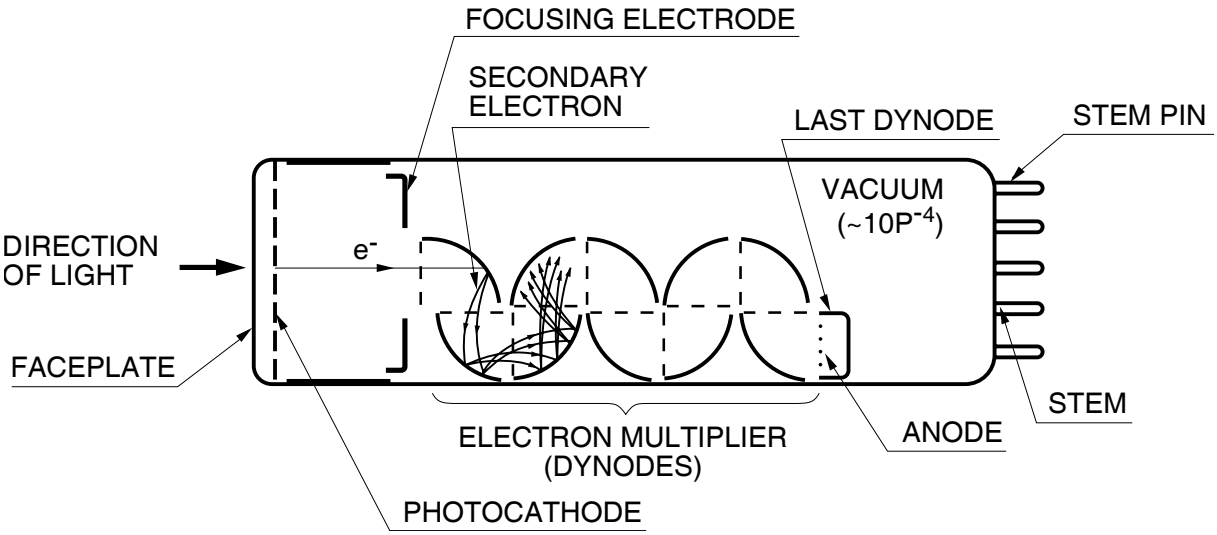

Figure 4.8: A sketch of the internal components of a photomultiplier tube (PMT). An incident photon passes the window (faceplate) and dislodges an electron from the photocathode after being absorbed. The electron is then accelerated in a potential gradient onto several dynodes, causing secondary electrons to be emitted, thus multiplying the signal. The electrons are then collected at the anode where they induce a voltage signal. [127]

different angles. The program itself allows for adjusting the recorded time window as well as trigger properties, which were set to a continuous software trigger. Triggering externally ensures that time windows are recorded independently of the pulse information they contain, showing reliable intensity distributions in both PMTs and removing any bias from data selection.

The `LabVIEW` software was later modified to not only show the recorded data but save it as well. `LabVIEW` itself supports file saving management in ASCII, so the program was expanded to save each time window in its own text file in a predetermined location on the disk drive. A custom name for the files can be chosen and all are placed in a subfolder with that same name, numbered starting from zero. Each individual file contains the relative recorded time values in units of nanoseconds, from 0 ns up to how long the time window was chosen, as well as the respective amplitude of all active channels at that point in time, separated by a tab character.

Soon it was observed that the amount of data recorded for several thousand time windows ended up becoming unwieldy. Furthermore, the text files needed to be converted into binary before the analysis written in `CERN root` could be applied to it, which took a long time. For those reasons, a custom code was written in `C++` and compiled into a Dynamic Link Library (DLL) that `LabVIEW` can recognize and allows saving the data directly in `.root` files, all collected within a tree with separate leaves for each type of information (time and channel amplitudes). This reduced the file size by 66%, however, since the format conversion now occurs during data acquisition instead of post-processing, it increases the time it takes for one file to be created by a factor of four. Because software-triggering waits for each file to be written before issuing a new trigger, this essentially also equates to an increase in measurement time, however considering the time saving gained from handling less data and avoiding a dedicated data-conversion phase, this essentially amounts to a zero-sum. It is still considered a net-gain, since the analysis now requires

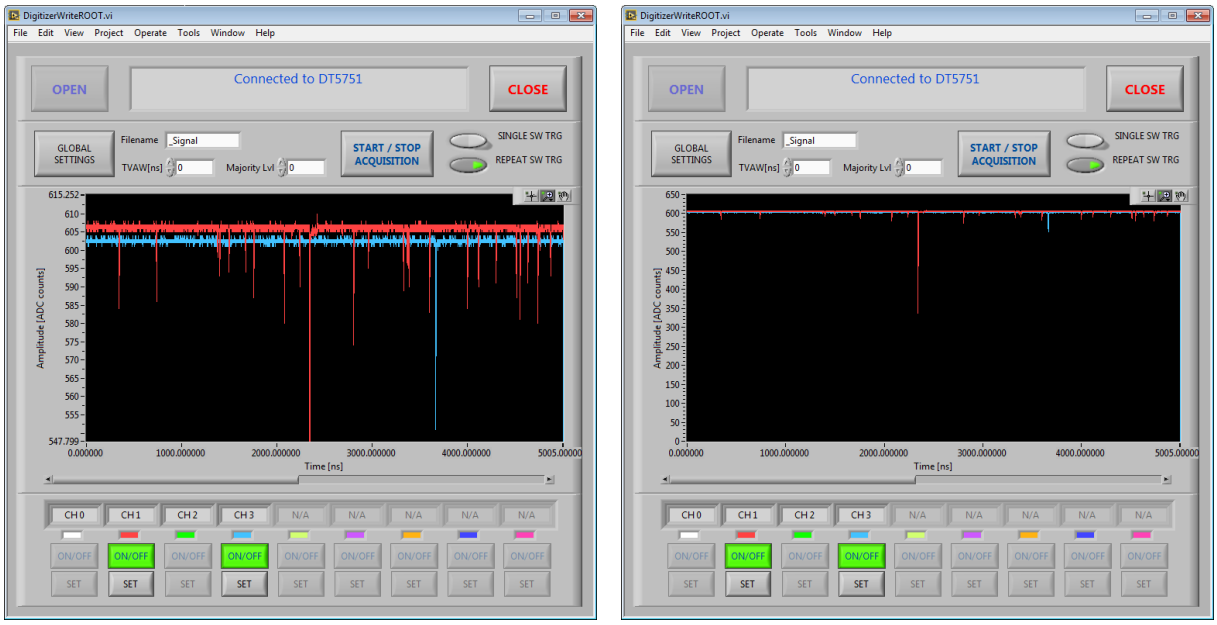

Figure 4.9: Screenshots of the `LabVIEW` software used to record ADC time windows, zoomed in on the pulses (left) and showing the full vertical voltage range (right). The beam-PMT is shown in red, the scat PMT in blue. Note that the big red pulse is a background event (likely an external muon) and all signal events are roughly of the same amplitude ($\mathcal{O}(20)$ ADC counts $\widehat{=}$ $\mathcal{O}(40\,\mathrm{mV})$). Further note that due to slight differences in fabrication, the PMT located in the scat position produces on average higher pulses ($\mathcal{O}(100\,\mathrm{mV})$) than the one used in the beam position. The difference in baseline is inherent to the ADC channels.

less intermediate steps to be performed. Furthermore, the code is also used in other experiments conducted in the lab with significantly lower event rate (Compton-scattering coincidence measurements) which benefit from the streamlined data processing greatly.

For each investigated sample a total of 20,000 individual time windows were recorded with a window length set to $10,010\,\mathrm{ns}$ (the offset is caused by internal settings of the ADC) amounting to a total of $0.2002\,\mathrm{s}$ of recorded illumination for both PMTs. For reference, a single photon pulse has a length of $15\,\mathrm{ns}$.

4.4 Instrument Calibration

In order to guarantee reproducibility of the experimental data and minimize systematical uncertainties of the results, all components of the setup mentioned in the previous sections have been carefully and painstakingly calibrated prior to measuring for maximum reliability during operation. This section will highlight the most important components, the methods used for calibration and the results obtained for precision and uncertainties. Since some previously calibrated components were used in the process of measuring subsequent ones, the order of the following subsections is arranged accordingly. Occasionally, some components that had already been quantified were later cross-checked using different instruments or methods. In these specific cases, both measurements and their respective results will be described.

4.4.1 Lamp and Monochromator

Probably the main component of the Rayleigh scattering setup is the light source. While the actual determination of the scattering length is based on a comparative ratio measurement between both PMTs that does not necessarily require absolute lamp stability, many of the calibrations of other components requires the light intensity to be constant. Therefore, the light source, an Oriel APEX2-QTH quartz-tungsten halogen lamp, was investigated for intensity fluctuations, both on short and long time scales.

The initial set of measurements for lamp stability were conducted with a silicon photodiode sensor (Thorlabs S130C) attached to a digital power meter (Thorlabs PM100D) that measured the light intensity. The sensor has a $\varnothing = 9.5\,\mathrm{mm}$ aperture with a wavelength range from 400 to 1100 nm over a power range between 500 pW and 5 mW at a resolution of 100 pW.

The first observation was that the lamp possesses a warmup-phase during which the light intensity exponentially decreases by about 6% from the moment it is initially turned on (figure 4.10). The lamp reaches its operating intensity after roughly 3000 s, so it was decided to wait with measurements for at least an hour after power-on for the lamp to stabilize. Furthermore, smaller intensity fluctuations of $\sim 3\%$ on timescales of $\mathcal{O}(200\,\mathrm{s})$ can be seen throughout. It is theorized that they are caused by internal fluctuations in the power supply.

Next, the stability over multiple days was investigated. The lamp was turned on each day in the morning and ran for several hours before the intensity was recorded. The measurement was repeated daily over the course of one week, with a weekend in between to check if the lamp degenerates after repeated use and/or regenerates after a hiatus. In the

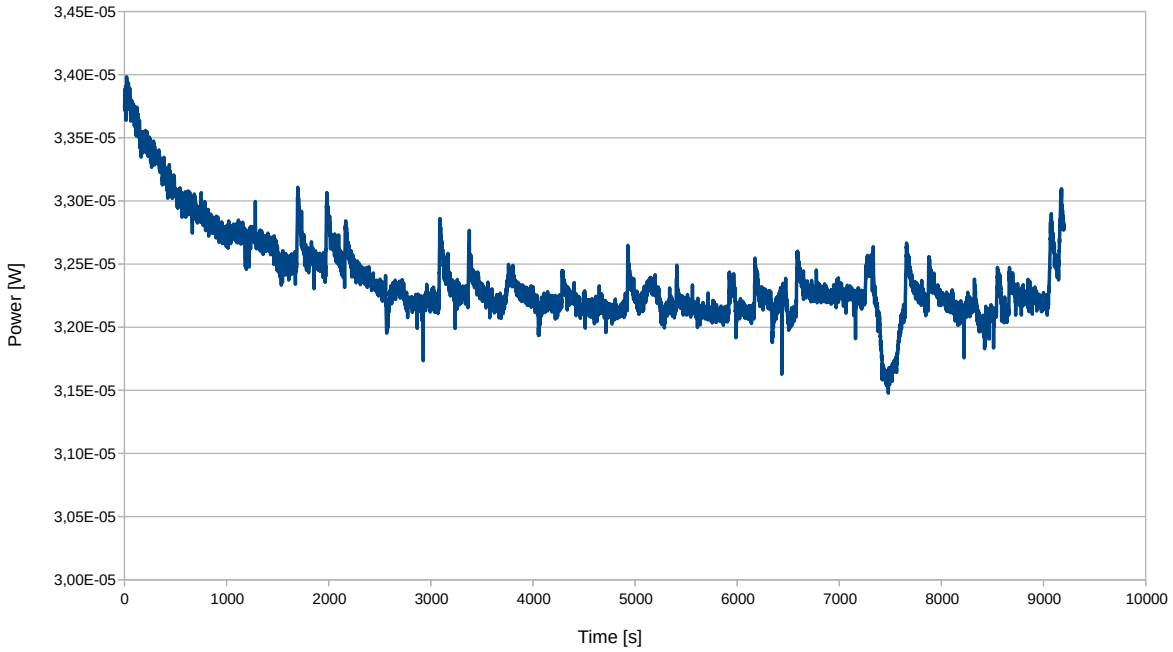

Figure 4.10: The warmup phase of the quartz-tungsten halogen lamp measured with a silicon photodiode. An exponential decrease of intensity over the first hour of operation can be observed, as well as repeated smaller fluctuations in intensity due to internal electronics.

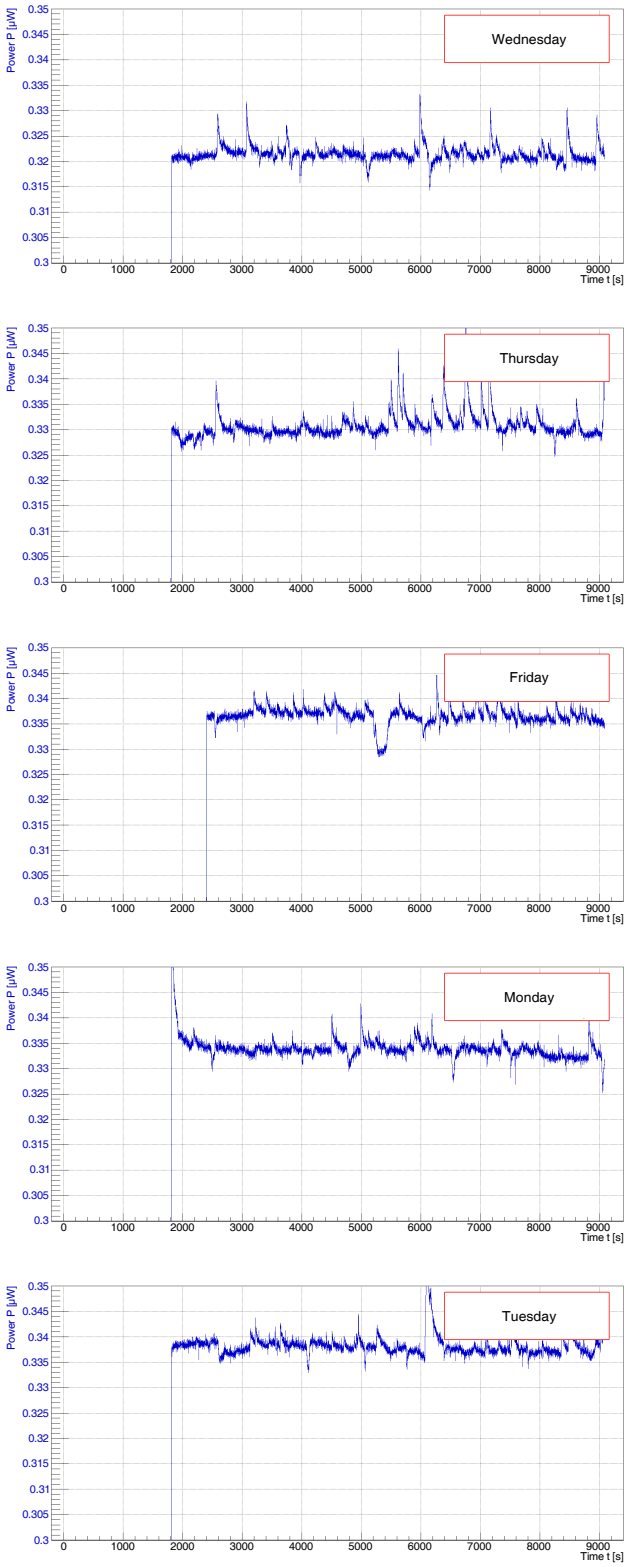

Figure 4.11: Lamp intensities measured over several days, with a weekend in between to check for intensity losses due to repeated usage.

end, no such effect was found, but it was observed that the operating intensity varies from day to day within a 6% margin. The graphs recorded with the power meter are collected in figure 4.11.

Lastly, consecutive long-term stability was examined. However, due to technical limitations with the DAQ software of the power meter, simply measuring the beam intensity over extended periods of time was not realizable with the silicon photodiode. Instead, the calibration was conducted with the Rayleigh scattering experiment proper once its linearity was established (c.f. section 4.4.5). Details of data acquisition were described in section 4.3 while analysis will be in 4.5, but as a short synopsis: Both PMTs record 10 μs time windows after a simultaneous external trigger. As the intensity in both channels is low (either due to faint scattering properties or shielding with a neutral density filter) they are able to discern single photons. The analysis code then counts their number within each window. The data taking ran over night and the counts were summed over and filled into a histogram. Results for a total of 260,000 time windows divided into 260 bins corresponding to $\sim$ 15 hours can be seen in figure 4.12. No significant tendency for a change in lamp intensity was observed and the lamp is considered to be stable. The fluctuations for the beam-PMT are once more on the 6% level, so this was the overall uncertainty applied to the number of single photons from here on out.

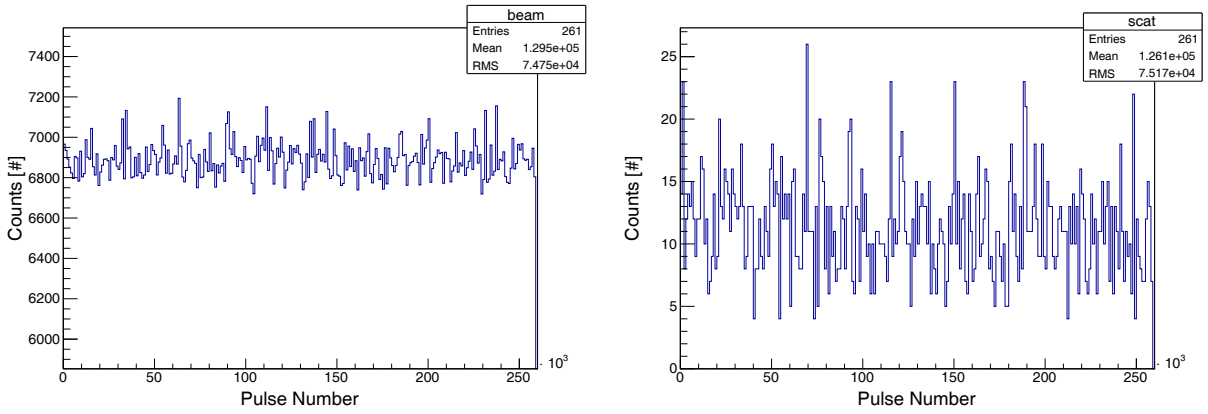

Figure 4.12: The long-term stability measurement of the quartz-tungsten halogen lamp obtained by the Rayleigh scattering setup itself. The data was taken over night during the course of roughly 15 hours. No significant trend for a change in intensity can be observed.

Besides the lamp intensity itself, the monochromator (Oriel Cornerstone 260) spectral precision was determined by coupling the light into a glass fiber cable attached to a portable UV/Vis-spectrometer (OceanOptics USB2000). The resulting wavelength distribution for a selected mean of 550 nm can be seen in figure 4.13, where it is fitted with a Gaussian function. As a conservative estimate, the FWHM of the peak was used instead of the standard deviation to determine the wavelength precision of the monochromator, resulting in an uncertainty of ±2 nm.

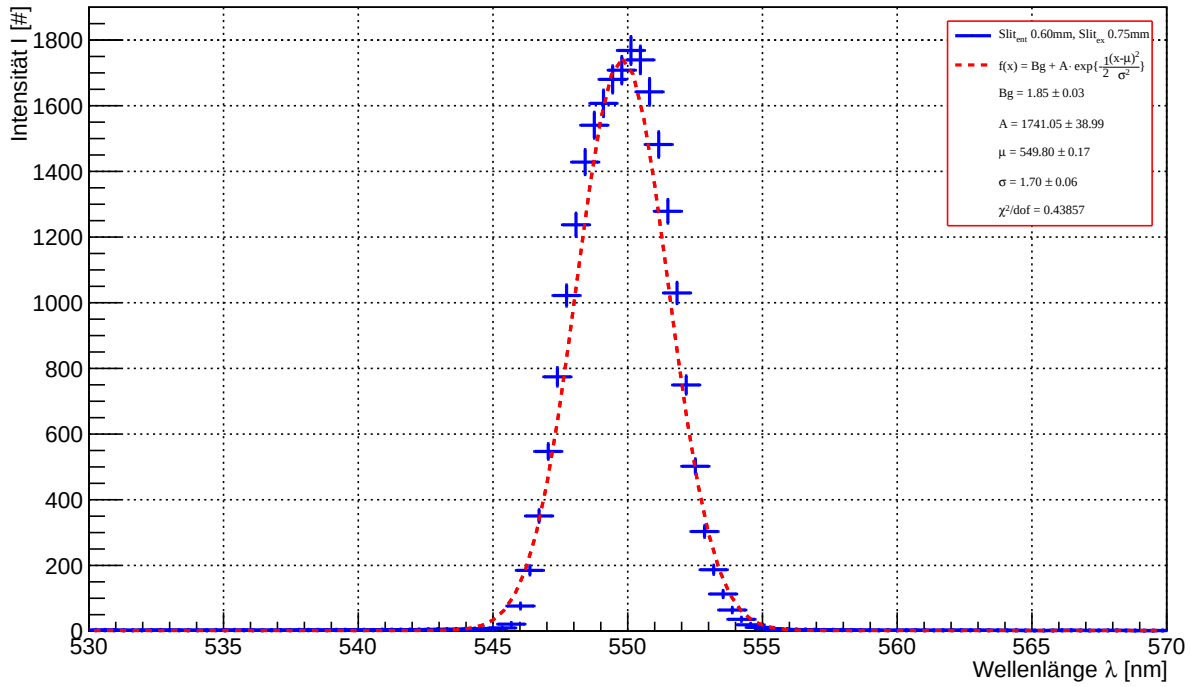

Figure 4.13: The wavelength distribution of the monochromator when set for 550 nm. The wavelength precision of the device is considered to be ±2 nm based on the peak's FWHM.

There is, however, one caveat to the lamp stability measurement: For reasons unknown, the system occasionally does not fully power up after being switched on. In some cases, no beam will be produced at all. Some other times, light intensity does not reach its maximum but rather stops at roughly 50% of its peak value or less. It is presumed that this is caused by misalignment of the monochromator during powerup, so the beam center misses the exit slit fully or partially. Turning both the lamp and the monochromator off and on again to restart the power-up phase solves the issue, but extra care was taken to manually check the beam performance after each start-up so as not to accidentally measure at less than full intensity, since this would reduce statistics of the Rayleigh scattering measurement and impair comparability of measurements across multiple days.

4.4.2 Neutral Density Filters

In the experimental setup (c.f. section 4.2) the beam photomultiplier $\mathrm{PMT_B}$ is placed directly into the light path to monitor the lamp intensity for reference. However, since the photocathode is highly sensitive, it is shielded from overexposure by a neutral density filter. This allows the PMT to operate in the single photon counting range, and the total intensity of the beam can then be inferred by scaling the measured result with the filter transparency. To that end the optical density of the filters, as given in equation (4.8), must be known to a high precision.

$$OD = -\log_{10}\left(\frac{I'}{I_0}\right) \tag{4.8}$$

The opacity of a long dozen neutral density filters was determined using the halogen lamp and the aforementioned photodiode attached to a power meter (Thorlabs S130C, Thorlabs PM100D, c.f. subsection 4.4.1). Since the diode is not spectrally sensitive, the measurement was only conducted at one singular wavelength, namely 430 nm. Each filter was placed into the beam separately, measured for ten minutes and the recorded intensity then compared to a reference measurement without filter. Luckily, while the photodiode cannot distinguish colors it does have a broad sensitivity to light intensity over seven orders of magnitude, so it was possible to measure all filters in one go without needing to adjust the integration time or lamp aperture. The results are displayed in figure 4.14. It should be noted that the 6.0 filter (Thorlabs NE60B-A) turned out to actually absorb less light at 430 nm than the 5.0 filter, presumably because of different production material or coating. However, an attenuation higher than five orders of magnitude was not required for the Rayleigh scattering experiment and thus this filter never used.

The Rayleigh scattering setup specifically utilizes the filter with a nominal density of 5.0 (Thorlabs NE50B-A). This extinction has proven too high to use the available commercial spectrometer (PerkinElmer Lambda 850) for a wavelength-dependent calibration, but it was possible to measure a similar filter with an optical density of 4.0 to a high precision using this device. The spectrometer uses two lamps – one deuterium, the other tungsten – and a chopper to split the light into two beams whose intensity is compared after they passed two samples. In this case, the ND filter was placed in one sample spot while the reference beam was left unobstructed.

The 4.0 filter was subsequently inserted into the Rayleigh scattering setup proper and the attenuated light intensity was measured at several wavelengths between 400 nm and 470 nm at 5 nm intervals. This process was then repeated with the 5.0 neutral density

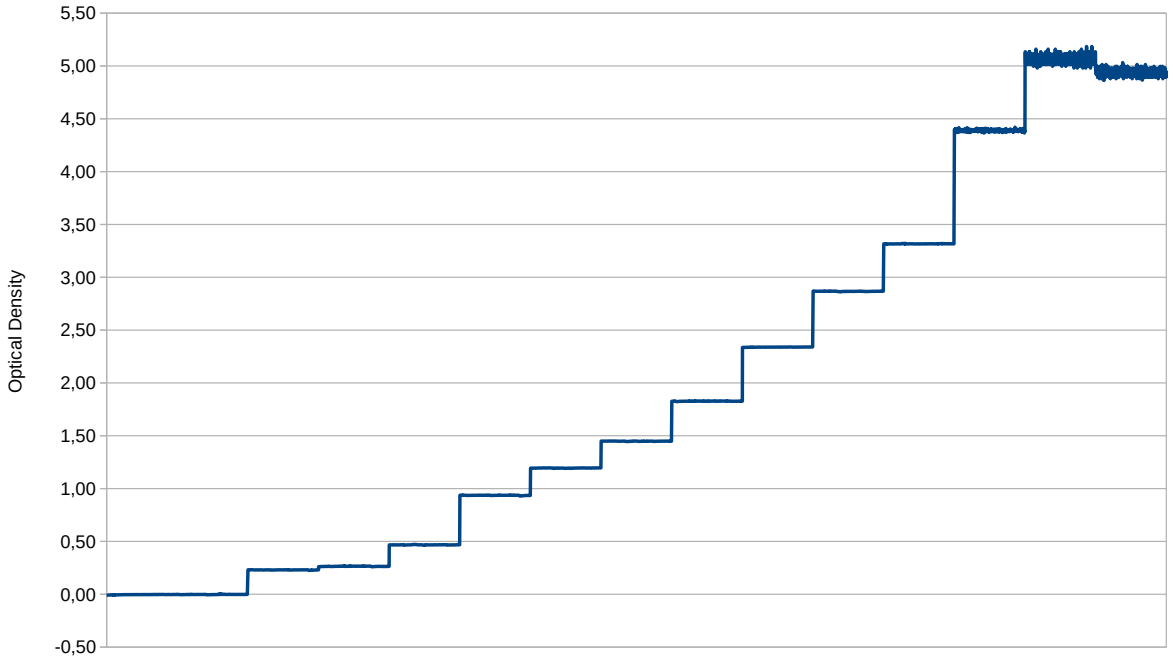

Figure 4.14: Results of the optical density measurement with the power meter for both absorptive (a) and reflective (r) filters. Left to right: Reference, 0.3a, 0.3r, 0.5r, 1.0r, 1.3r, 1.5r, 2.0r, 2.5r, 3.0r, 3.0a, 4.0a, 5.0a, 6.0a.

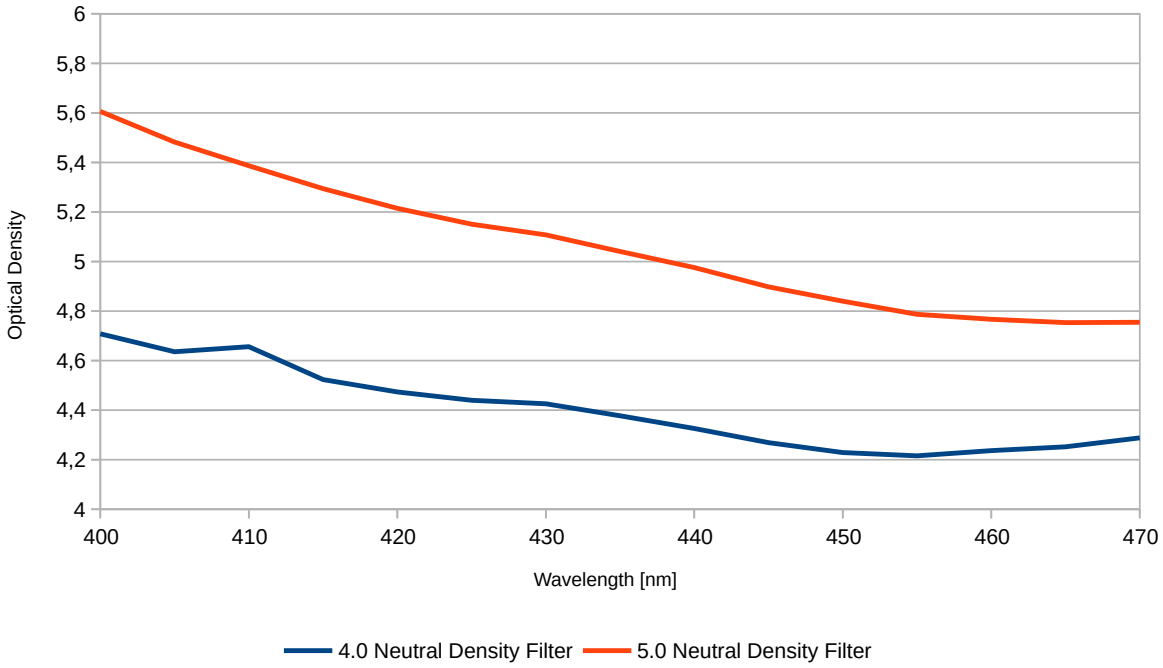

Figure 4.15: Wavelength-dependent calibration curves for the Thorlabs absorptive 4.0 (blue) and 5.0 (red) neutral density filters. The data points are spaced by 5 nm.

filter that is to be calibrated, allowing to relate the relative absorption between both filters obtained with the Rayleigh setup to the absolute calibration of the 4.0 filter conducted with the commercial spectrometer. Obviously this was only possible after the linearity of the involved electronics was guaranteed, which in turn was done using the optical densities obtained from the power meter (see subsection 4.4.5). The results of the wavelength-dependent filter calibration can be seen in figure 4.15. Their values at 430 nm are in good agreement with those obtained by the power meter. Note that the uncertainties on the optical density will be later determined by fitting the data obtained from reference samples of known scattering lengths (c.f. section 4.7).

4.4.3 Polarizers

In addition to the neutral density filters, two wire grid polarizers (Thorlabs WP25M-VIS) are placed within the light path and need to be characterized to correctly quantify the beam properties. Their purpose in the experimental setup is to select both the incident polarization axis of the beam as well as the axis under which the scattered light is measured. Consequentially, the orientation of the optical axis of the polarizer as well as its transparency to fully polarized light along said axis need to be determined.

For the first part of the calibration, an unpolarized light source was used to illuminate a water surface at Brewster's angle (53° for the transition between air and water). The polarizers were then placed in the reflected beam and slowly rotated until the light intensity reached its maximum. The respective position was marked with an angular precision of ±1°. However, this uncertainty will not be considered for the final analysis, since the transmission depends on $\cos^2\theta$ according to Malus' law, and thus even a deviation of a full degree would change the result only by 0.03%.

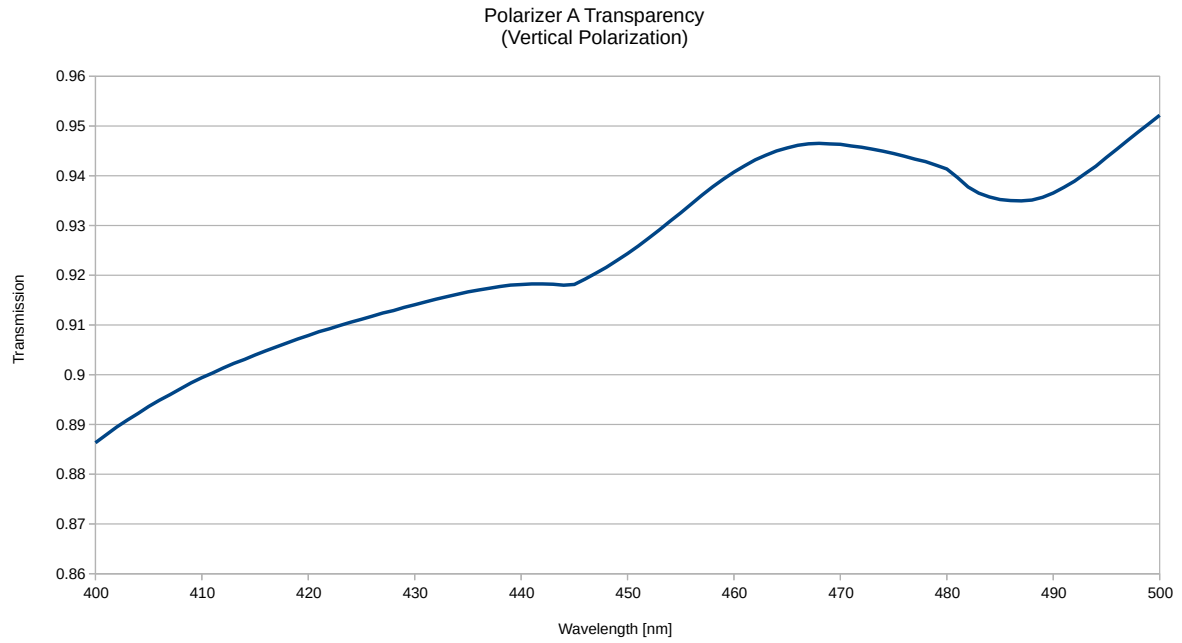

Figure 4.16: Calibration curve of polarizer A. The intensity I_{A+B} was divided by I_B in order to obtain the transparency T_A.

Secondly, the polarizer transparency was characterized. To this end, both polarizers were placed into a UV/Vis-Spectrometer (PerkinElmer Lambda 850) in sequence, with the same (vertical) orientation of the optical axis. Effectively, the first filter creates an impromptu polarized beam, that should pass unobstructed through the second one. Comparing the measurements of both polarizers versus only one of them allows to obtain a wavelength-dependent transparency curve of the filter that was removed. Figure 4.16 shows the obtained calibration curve for polarizer A, which is the one that is placed in the scattered light path and whose transparency needs to be known for the analysis procedure (c.f. sections 4.2, 4.5 and 4.6.) The uncertainty of the result was determined to ± 0.0005, given the spectrometer's resolution.

4.4.4 Geometry

For the Rayleigh scattering experiment to produce sensible results, the various components of the setup must be aligned with extraordinary precision. Extreme care was exercised to make sure that all instruments are vertically located at the same height as the beam – which was measured to 12.6 cm above the optical table, with < 8 mm in diameter – as well as in correct horizontal placement within the beam's path.

Horizontal adjustment was achieved twofold: For components along the beam path, the light itself was used for correct alignment. First, the photomultiplier on the opposite side of the setup was placed in such a way that the beam profile would hit the photosensitive area full center, without any optical instruments in between. Afterwards, each subsequent component was added individually – starting with the ones closest to the lamp – and aligned such that the beam spot would not shift from its unobstructed position.

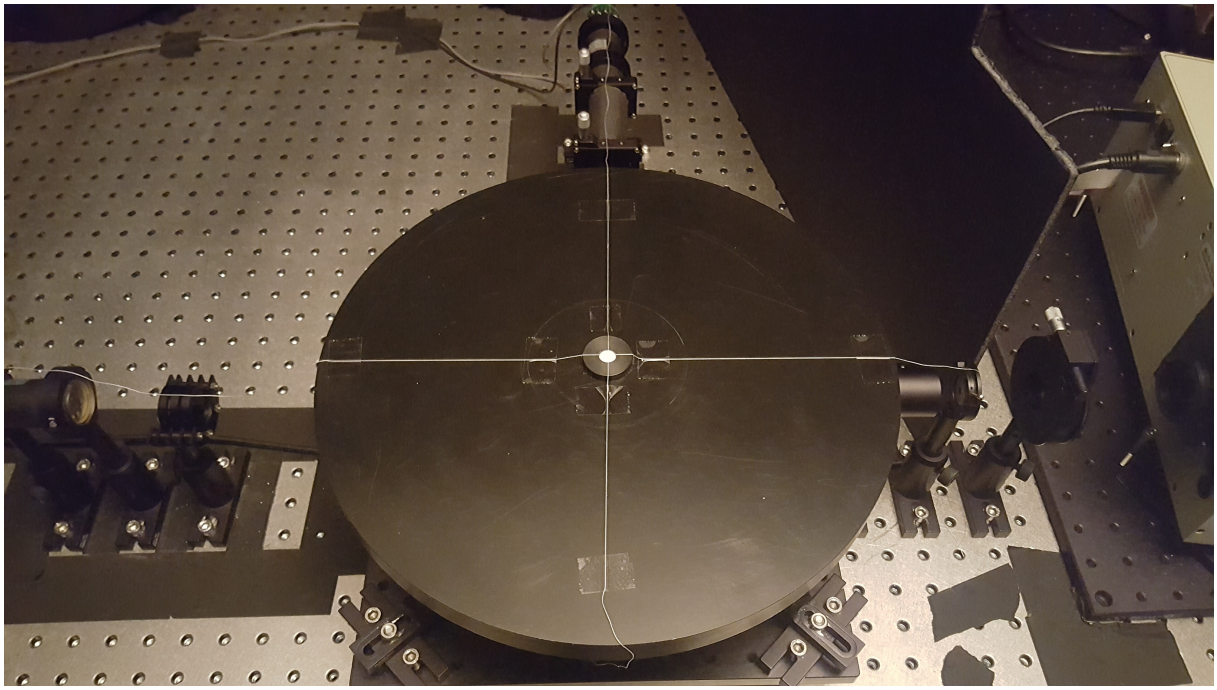

Figure 4.17: Horizontal alignment of the components along the scattering axis relative to the beam axis.

After all instruments along the beam axis were properly placed, the components on the perpendicular axis had to be aligned accordingly. As a visual aid, the beam path was traced with a string of thread and a second string was added at 90° going through the center of the sample position, as depicted in figure 4.17. The center of the scatter-PMT, the two precision slits and the polarizer were then adjusted accordingly.

In theory, components along the beam axis should already have the correct vertical alignment, as they were adjusted according to the beam profile itself. Still, each component was individually examined for the correct height and if necessary fine-tuned while constantly cross-checking that the beam spot would not misalign. As for the objects in the scattering path, each component was first raised individually to the correct height and later matched with its neighbors using single and two-way spirit levels. Precision for vertical alignment was determined to be at the sub-millimeter level.

The previously described alignment was subsequently visually checked. To this end, a PnBAPS68 colloid sample (Poly-n-Butylacrylamide-Polystyrene, $\varnothing = 68\,\mathrm{nm}$, solved in water) with strong scattering properties was placed in the cuvette slot to highlight the beam path. On the perpendicular axis, the PMT is removed from the setup and a lamp is placed in its holder instead. Figure 4.18 shows both light sources overlap in the middle of the cuvette, demonstrating the correct alignment of the axes.

Furthermore, temporarily removing the scatter-PMT also gave the opportunity to check the adjustment of its field of view. First visual inspection revealed that the beam is well within the window provided by the two precision slits. However, a reflection of the light on the surface of the index-matching liquid was also visible at the upper edge of the window. Subsequently, more Ccyclohexane was added into the vat until the liquid

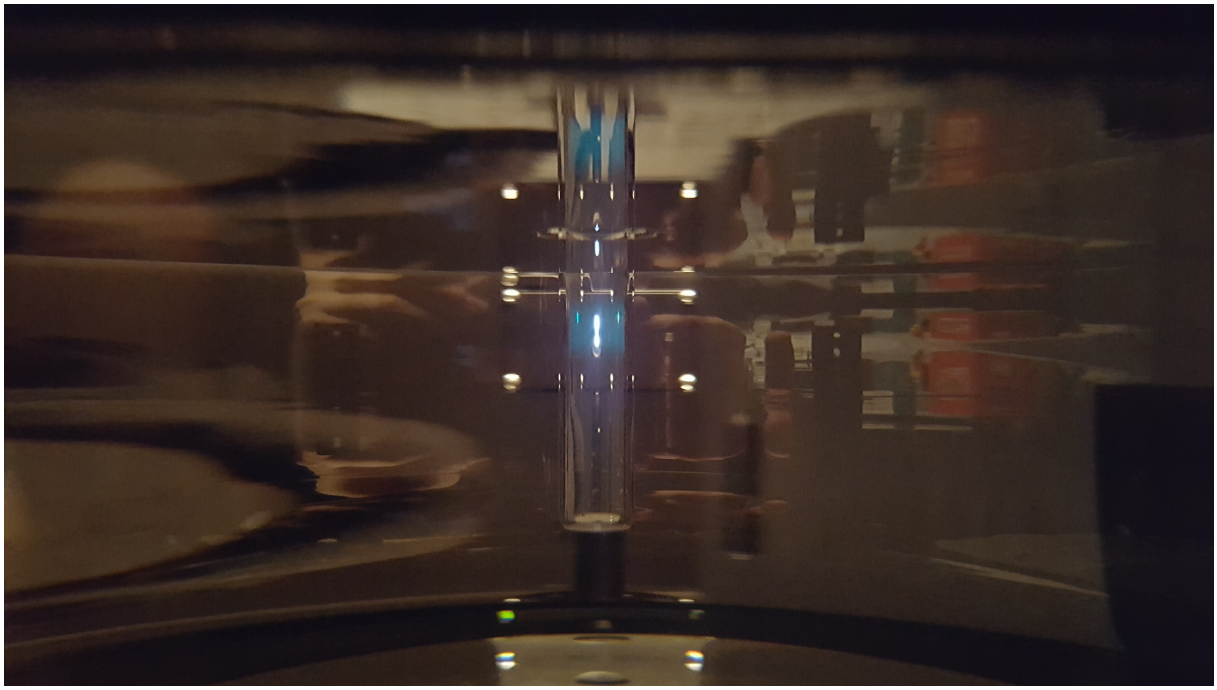

Figure 4.18: Demonstration of the correct alignment of the light beam (teal) with the scattering axis, represented by a lamp (white) placed at the location of the photomultiplier. Note the reflection of the beam on the index matching liquid surface on top.

Figure 4.19: Photo taken from the position of the scat-PMT demonstrating its field of view, with the slit window (red) and the beam (teal). The beam is in good view and no reflection at the liquid surface is visible.

level rose high enough for the reflection to no longer be able to pass through both slits and reach the PMT. Figure 4.19 shows PMT_S's field of view with the beam clearly visible within the slit window (marked red) and without any reflection visible. Compare this to figure 4.18, which is taken from the opposite side and shows the reflection that would be located above the slit window.

4.4.5 Electronics

Once both the light source and the neutral density filters were properly characterized, it was possible to use them to in turn calibrate the entire electronics chain, consisting of the photomultiplier tubes (Hamamatsu R9980 K-ASSY) powered by a high voltage supply unit (iseg DPR 20 605 24 5) set to $-1.5\,\mathrm{kV}$ negative voltage and read out with a desktop digitizer (Caen DT5751). To this end, filters with increasing opacity were placed in the beam path, that would cause an appropriate reduction in counts within the PMTs. If the electronics system is able to correctly measure the change in intensity, it can be considered linear as a whole.

In total, eleven filters with optical densities between 0.3 and 4.0 were used to reduce the lamp intensity, with an initial reference measurement at full power. Note that the beam-PMT was still shielded by the 5.0 neutral density filter, to protect it from possible damage caused by overexposure due to its placement directly in the light path. Conversely, the scatter-PMT is only able to see as much light as is scattered by the colloid sample (previously mentioned in subsection 4.4.4) which is sufficiently little so that it does not need additional shielding.

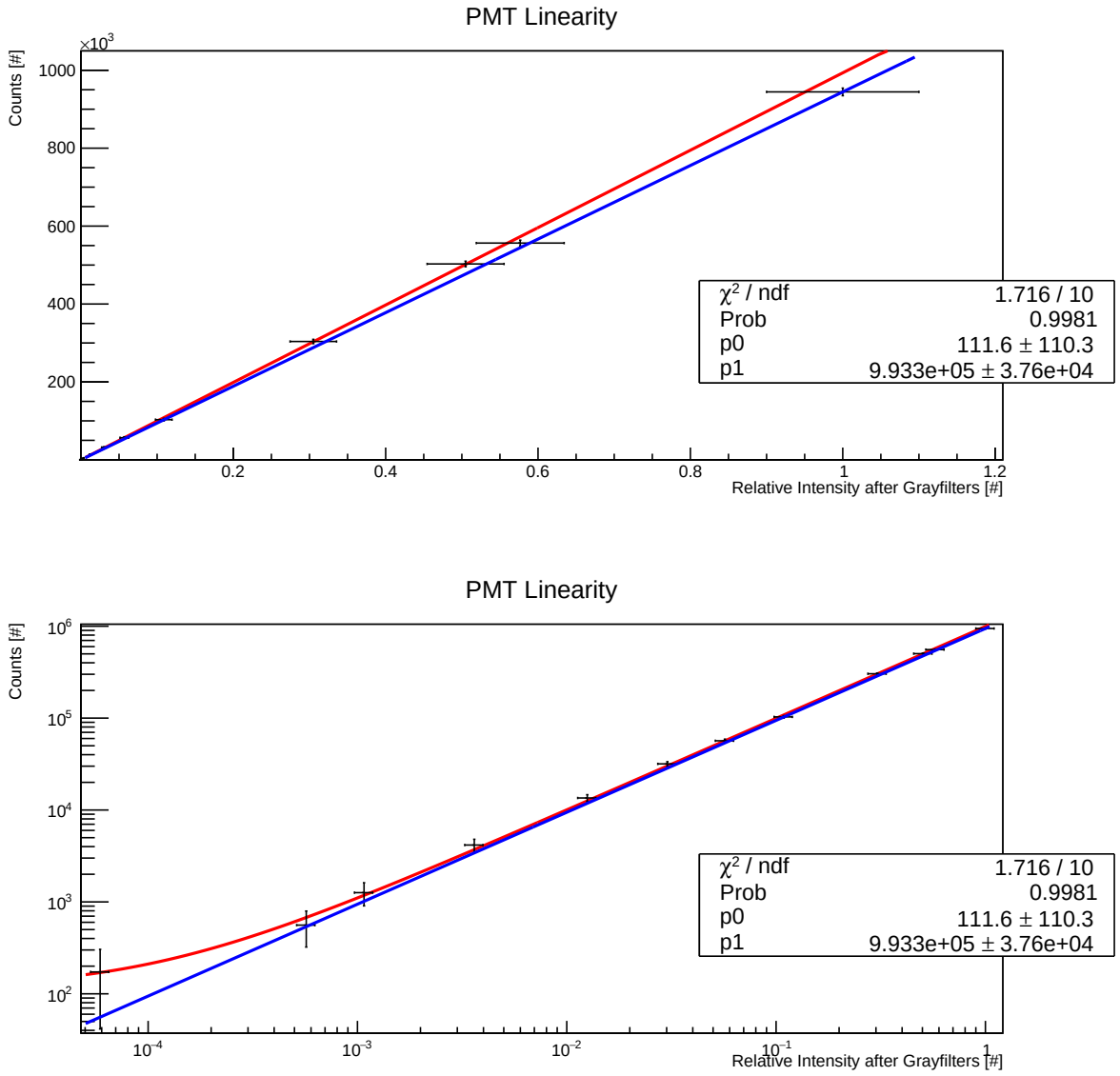

Figure 4.20: Results of the linearity measurement for the electronics chain of the Ralyeigh scattering experiment for the beam-PMT on a linear (top) and logarithmic (bottom) scale, fitted by a linear function with a constant offset (red). Light intensity was gradually reduced by neutral density filters of increasing opacity and the amount of single photons in each PMT was counted. Error bars on the y-axis were increased by a factor of 10 for visibility. The blue line represents the ideal linearity without background events.

With both PMTs operating in a low-intensity range, they are able to discern individual photons. The light intensity can then be directly equated to the number of counts detected by the PMTs. To this end, 20,000 time windows of $\sim 10\,\mu$s length were recorded per filter (and once for the reference). All data was taken consecutively on the same day, so as not to introduce a systematic error into the measurement due to variable beam intensity after switching the lamp off and on again (c.f. subsection 4.4.1). The number of pulses within each measurement was then counted and plotted against the relative intensity (calculated by using the optical density of the filters obtained in subsection 4.4.2 within the inverse of formula (4.8)) and fitted by a linear function with a constant offset.

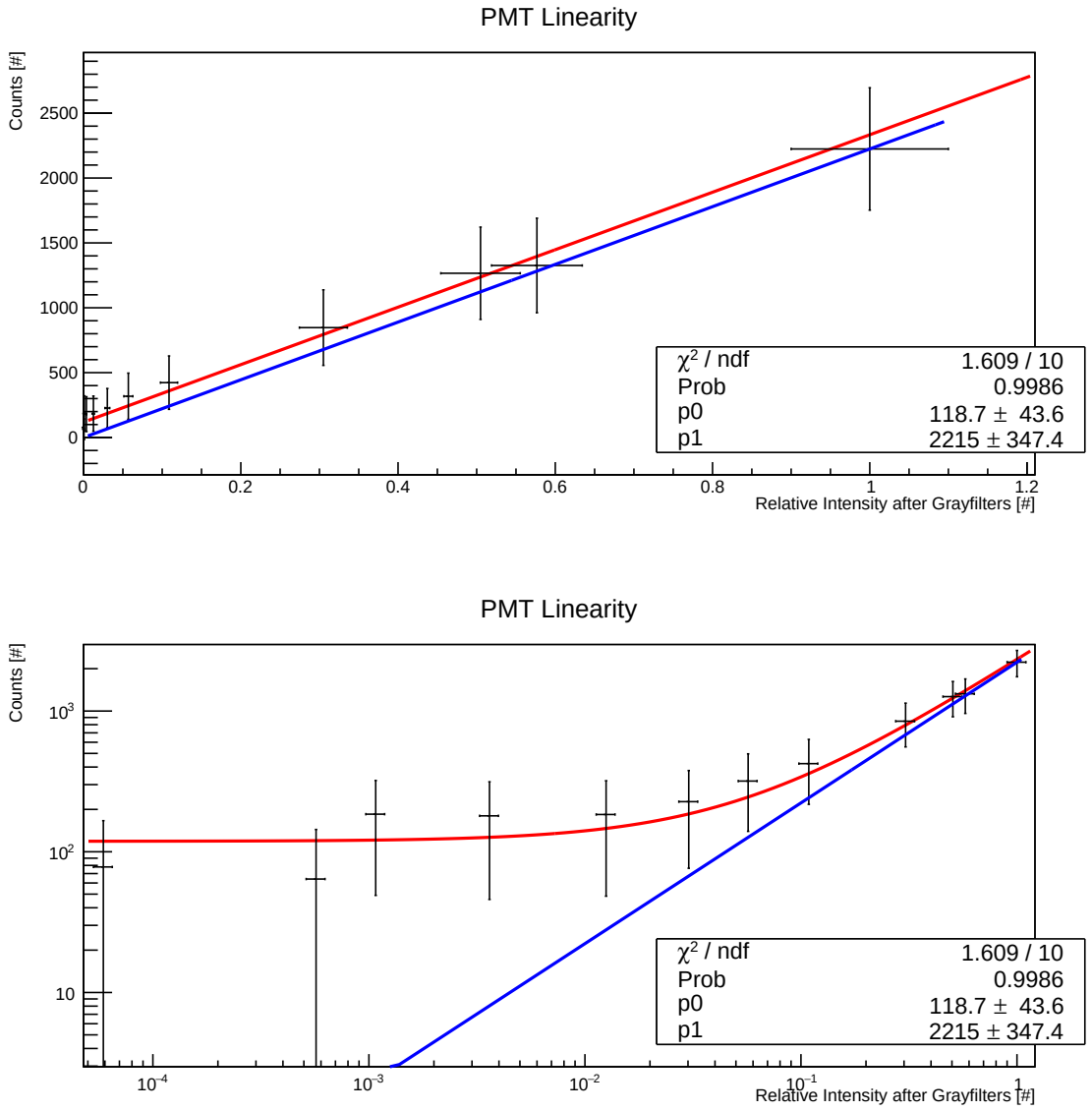

Figure 4.21: Results of the linearity measurement for the electronics chain of the Ralyeigh scattering experiment for the scatter-PMT on a linear (top) and logarithmic (bottom) scale, fitted by a linear function with a constant offset (red). Light intensity was gradually reduced by neutral density filters of increasing opacity and the amount of single photons in each PMT was counted. Error bars on the y-axis were increased by a factor of 10 for visibility. The blue line represents the ideal linearity without background events.

The results for the beam-PMT can be seen in figure 4.20 while those for the scatter-PMT are shown in figure 4.21 respectively. Note that the error bars for the number of counts on the y-axis were increased by a factor of ten, as they otherwise would not have been visible in this scale. The fit is colored in red while the blue line shows the ideal linearity connecting the reference measurement without ND filters to the coordinate system's point of origin. Both fit curves follow this line closely up until the very low intensity regime, where they approach a constant offset representing the number of background events from the PMT's dark count rate. This deviation is much more prominent in the scatter-PMT than the beam-PMT, due to its lower signal intensity.

Overall both PMTs as well as the electronics they are attached to are considered to be linear based on these results. Nevertheless, an effort was made for each sample measurement to be preceded by an accompanying background check of equal length, the number of counts within then being subtracted from the signal data. The dark count rate was estimated to be in the order of $\sim 500\,\mathrm{cts/s}$ (given $\mathcal{O}(100\,\mathrm{cts})$ within $0.2\,\mathrm{s}$), caused by a combination of residual light in the dark room and thermionic discharges from the PMT itself (c.f. section 4.3).

4.5 Analysis Procedure

As previously mentioned in section 4.1, Rayleigh scattering has a very distinct angular emission profile; the orthogonal polarization is isotropic in θ-direction while the parallel polarization roughly follows a $\cos^2(\theta)$-dependence. Figure 4.22 shows the Rayleigh scattering θ-dependence, as well as the angular region perpendicular to the beam that the experiment is sensitive to.

The intensity of the scattered light can be trivially expressed as the difference between the initial and the final intensity after passing the sample. Using the Beer-Lambert-law from equation (4.1), one of these two quantities can be eliminated from the formula:

$$\begin{aligned} I_{\mathrm{Scat}} &= I_0 - I(x) \\ &= I_0 \cdot \left(1 - \exp\left(-\frac{x}{\Lambda_{\mathrm{Ray}}}\right)\right) \\ &= I(x) \left(\exp\left(+\frac{x}{\Lambda_{\mathrm{Ray}}}\right) - 1\right) \end{aligned} \tag{4.9}$$

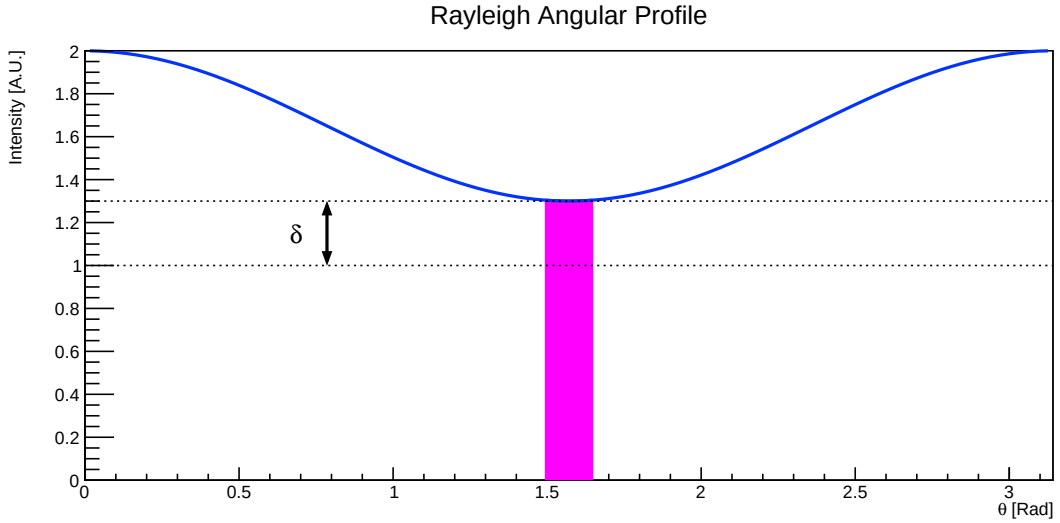

Figure 4.22: Rayleigh angular profile for a real Rayleigh scatterer. The constant lower half of the curve is contributed by the orthogonal polarization and is isotropic in θ-direction. The parallel polarization in the upper part is $\cos^2(\theta)$-dependent, whereby its minimum value depends on the depolarization ratio δ. The violet strip represents the part of the total emission that the experimental setup is measuring.

Since the setup is measuring $I(x)$ instead of I_0, it is more convenient to use this parametrization going forward. This formula can then be solved for Λ_{Ray}:

$$\Lambda_{\mathrm{Ray}} = x \cdot \ln^{-1}\left(\frac{I_{\mathrm{Scat}}}{I(x)} + 1\right) \tag{4.10}$$

In accordance with equation (4.3), I_{Scat} can be calculated by measuring both polaizations independently, then adding up the individual contributions. However, since the setup is sensitive only within the angular range where the photomultiplier is located, the detected intensity needs to be scaled up to account for the entire solid angle: Integrating the angular distribution function over 4π and dividing it by the integral for a small range around $\theta = 90°$ and $\varphi = 0°$ yields a scaling factor that allows to extrapolate from the photons observed within the selected solid angle to the total scattered light.

For the orthogonal polarization, this is fairly easy, as the Rayleigh scattering amplitude possesses no angular dependence in θ-direction. Therefore, only the angular distribution function for φ needs to be taken into account:[128]

$$I_\perp = I_\perp(90°) \cdot \frac{\int_{0°}^{360°}\int_{0°}^{180°}\left[1 - \frac{1}{2}\cos(2\varphi)\right][1]\sin\theta \mathrm{d}\theta\mathrm{d}\varphi}{\int_{-\varphi/2}^{\varphi/2}\int_{90°-\theta/2}^{90°+\theta/2}\left[1 - \frac{1}{2}\cos(2\varphi)\right][1]\sin\theta \mathrm{d}\theta\mathrm{d}\varphi} \tag{4.11}$$

However, the parallel polarization not only depends on θ but also on the depolarization ratio δ (c.f. equation (4.5)). As such, the angular distribution function must not only satisfy the condition of $F(\theta = 0°) = 1$ but $F(\theta = 90°) = \delta$ as well:

$$I_\parallel = I_\parallel(90°) \cdot \frac{\int_{0°}^{360°}\int_{0°}^{180°}\left[1 - \frac{1}{2}\cos(2\varphi)\right]\left[\delta + (1-\delta)\cos^2\theta\right]\sin\theta \mathrm{d}\theta\mathrm{d}\varphi}{\int_{-\varphi/2}^{\varphi/2}\int_{90°-\theta/2}^{90°+\theta/2}\left[1 - \frac{1}{2}\cos(2\varphi)\right]\left[\delta + (1-\delta)\cos^2\theta\right]\sin\theta \mathrm{d}\theta\mathrm{d}\varphi} \tag{4.12}$$

The aforementioned four integrals were then solved using Mathematica, and yield surprisingly simple results, given their complexity:

$$\begin{aligned}
\int_{0°}^{360°}\int_{0°}^{180°}\left[1 - \frac{1}{2}\cos(2\varphi)\right][1]\sin\theta \mathrm{d}\theta\mathrm{d}\varphi &= 4\pi \\
\int_{-\varphi/2}^{\varphi/2}\int_{90°-\theta/2}^{90°+\theta/2}\left[1 - \frac{1}{2}\cos(2\varphi)\right][1]\sin\theta \mathrm{d}\theta\mathrm{d}\varphi &= \frac{3}{2}\cdot\varphi\cdot\theta \\
\int_{0°}^{360°}\int_{0°}^{180°}\left[1 - \frac{1}{2}\cos(2\varphi)\right]\left[\delta + (1-\delta)\cos^2\theta\right]\sin\theta \mathrm{d}\theta\mathrm{d}\varphi &= 2\pi\cdot\left[\frac{4}{3}\delta + \frac{2}{3}\right] \\
\int_{-\varphi/2}^{\varphi/2}\int_{90°-\theta/2}^{90°+\theta/2}\left[1 - \frac{1}{2}\cos(2\varphi)\right]\left[\delta + (1-\delta)\cos^2\theta\right]\sin\theta \mathrm{d}\theta\mathrm{d}\varphi &= \frac{3}{2}\cdot\varphi\cdot\theta\cdot\delta
\end{aligned} \tag{4.13}$$

Inserting these results into equation (4.10) yields the final formula to calculate the Rayleigh scattering length with the values obtained from the experiment:

$$\begin{aligned}\Lambda_{\mathrm{Ray}} &= x \cdot \ln^{-1}\left\{\frac{I_{\parallel}(90°) \cdot \frac{2\pi\left[\frac{4}{3}\delta+\frac{2}{3}\right]}{\frac{3}{2}\cdot\theta\cdot\varphi\cdot\delta} + I_{\perp}(90°)\cdot\frac{4\pi}{\frac{3}{2}\cdot\theta\cdot\varphi}}{\langle I(0°)\rangle \cdot T_{\mathrm{Pol}}\cdot 10^{OD}} + 1\right\} \\ &= x \cdot \ln^{-1}\left\{\frac{4\pi\left(I_{\parallel}(90°)\cdot\left[\frac{4}{3}+\frac{2}{3\cdot\delta}\right] + 2\cdot I_{\perp}(90°)\right)}{3\cdot\theta\cdot\varphi\cdot\langle I(0°)\rangle\cdot T_{\mathrm{Pol}}\cdot 10^{OD}} + 1\right\}\end{aligned} \tag{4.14}$$

Note that the correction factors for optical instruments are already included, that is, the transparency of the polarizer T_{Pol} which affects the intensities measured by the scatter-PMT $I_{\parallel}(90°)$ and $I_{\perp}(90°)$ as well as the transparency of the neutral density filter OD as defined in equation (4.8) which affects the beam-PMT. All contributions from other optical components, such as the lens or the transparency of the glass walls, appear in both light paths equally and therefore cancel each other out. The angular brackets around $\langle I(0°)\rangle$ denote that this value is calculated as the average from both the parallel and orthogonal measurements, since changing the polarizer orientation does not impact the beam-PMT. The depolarization ratio δ is calculated via

$$\delta = \frac{2I_{\parallel}(90°)}{I_{\parallel}(90°) + I_{\perp}(90°)} \tag{4.15}$$

which accounts for the initial beam already being vertically polarized.[129]

4.6 Error Estimation

Each of these parameters and measured values carries with them their own specific uncertainties, some of which were already mentioned in section 4.4. In order to obtain the total error on the final Rayleigh scattering length, their individual contributions must be correctly propagated. To this end, the final formula (4.14) was differentiated with respect to every individual parameter using Mathematica. Statistical and systematical uncertainties are hereby treated independently.

The systematical uncertainty comprises the individual contributions from the polarizer transparency, the attenuation or optical density of the neutral density filter, the beam's path length through the sample and the opening angles θ and φ, which themselves are given by the precision slits used to limit the PMT's field of view (c.f. section 4.2).

As previously mentioned in subsection 4.4.3, the transparency of the *polarizers* was determined by means of a UV/Vis-spectrometer (PerkinElmer Lambda 850), yielding values for the range between 400 nm and 500 nm with nanometer precision. The uncertainty on these values is given by the precision of the device itself, which according to the manufacturer amounts to ± 0.0005. The precision on the orientation of the optical axis was estimated to be $\pm 1°$, however, since this would only contribute 0.03% according to the $\cos^2\theta$-dependence in Malus' law, it will not be considered in the error estimation.

The transparency of the *neutral density filters* had to be determined using a combination of the aforementioned spectrometer and the Rayleigh scattering setup proper (c.f. subsection 4.4.2). Due to time constraints and relatively long measurement times, the calibration could only be performed in 5 nm intervals. However, this does not interfere with the measurements performed in this thesis, as the samples were not illuminated at wavelengths in between. Unfortunately, due to the rather complicated calibration procedure, it was not possible to calculate the uncertainty of the neutral density filters in an a priori fashion. Rather, the precision on the optical density was retroactively determined from the fit to the measurement results of a sample with known scattering length. This process will be described in detail in section 4.7, however, for completion's sake, it shall be mentioned that the resulting uncertainty amounts to ± 0.016.

The error on the *path length* within the sample is the most important uncertainty of the experiment, as it directly translates to the uncertainty of the Rayleigh scattering length itself, since both are directly proportional to one another (c.f. equation (4.14)). Unfortunately, it is also the largest uncertainty out of all of them, as it essentially depends on the diameter of the cuvettes. At the time of this writing, there has been a severe shortage of cuvettes on the market for some years now, due to a delay in production from one of the biggest manufacturers, with delivery times of half a year and upwards. Considering both cost and schedule, the cuvettes chosen for the experiment were 19 mm round cuvettes from Borosilicate glass (Fisherbrand, Catalog No. 14-385-900D). In this case, 19 mm refers to the outer diameter, with an inner diameter of 18 mm. However, upon closer inspection, it was found that the diameters vary from cuvette to cuvette, albeit in the sub-mm-range. Conservatively, the uncertainty of the cuvette diameter and thus the path length was estimated to $\pm 5\%$ or ± 0.9 mm.

The *opening angles* θ and φ depend on the lengths and distances of the setup itself as well as the optical components in use. If only the plain geometry of the setup were considered, the angles would be given by the ratio of the distance from the sample to the second precision slit and its height and width, respectively. Their individual uncertainties could then be calculated by propagating the uncertainties of the individual lengths in question.

However, given the fact that the light propagates within various media with different refractive indices, a deviation of the maximum accepted angle because of refraction on the surfaces needs to be taken into account. As demonstrated in figure 4.23, three regions are distinguished: Light passes at an angle α through the innermost region, the sample itself, which may or may not have the same refractive index as the middle region, being the index-matching liquid through which light propagates at an angle β. Finally, after traversing the outer region, that is air, at an angle γ the light hits the PMT's sensitive area. This is easiest to calculate for the vertical direction, where the light passes flat incident surfaces and the relation between the angles is given by Snell's law:

$$n \cdot \sin\alpha = n_{\mathrm{CHX}} \cdot \sin\beta = n_{\mathrm{Air}} \cdot \sin\gamma \tag{4.16}$$

with $n_{\mathrm{CHX}} = 1.426$ and $n_{\mathrm{Air}} = 1$. The glass walls of the cuvette and the vat are being included within the Cyclohexane region, as the liquid was specifically chosen to possess a similar refractive index. Although they don't match perfectly (c.f. table 4.1), they are close enough and the walls sufficiently thin that this approximation is warranted.

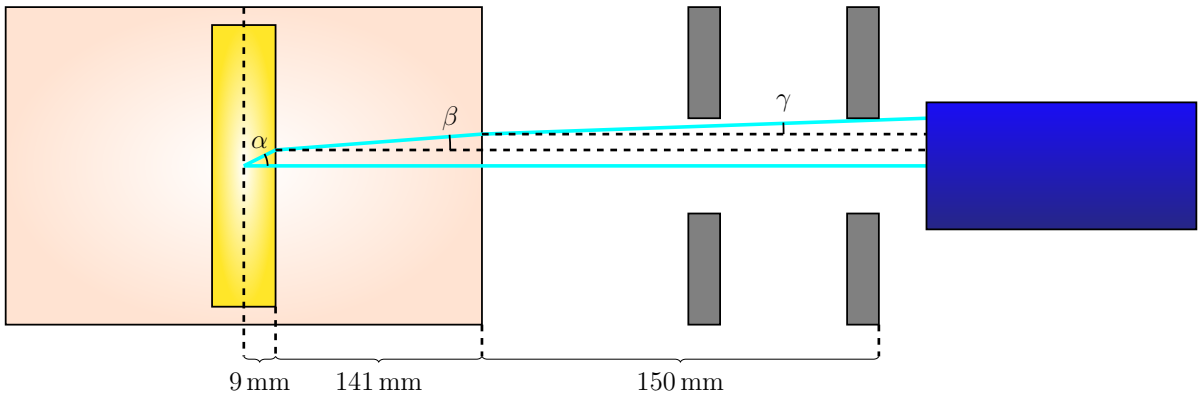

Figure 4.23: A side view of the path scattered light takes from the sample to the scatter-PMT. Distances not to scale. The lower blue line shows the direct path perpendicular to all surfaces. The upper blue line marks the beam path with the maximal angular deviation α that is still able to pass the slits after refraction.

Using the known geometry of the setup, it is possible to equate the slit height to the sum of distances that the light is traveling within each medium:

$$9\,\text{mm} \cdot \tan\alpha + 141\,\text{mm} \cdot \tan\beta + 150\,\text{mm} \cdot \tan\gamma = \frac{h_{\text{Slit}}}{2} = 6.7945\,\text{mm} \tag{4.17}$$

It is possible to express β and γ as functions of α and the various refractive indices using equation (4.16):

$$\begin{aligned} \beta &= \arcsin\frac{n}{n_{\text{CHX}}}\sin\alpha \\ \gamma &= \arcsin\frac{n}{n_{\text{Air}}}\sin\alpha \end{aligned} \tag{4.18}$$

Replacing them in equation (4.17) and using the small angle approximation allows to solve for α

$$9\,\text{mm} \cdot \alpha + 141\,\text{mm} \cdot \left(\frac{n}{n_{\text{CHX}}}\right) \cdot \alpha + 150\,\text{mm} \cdot \left(\frac{n}{n_{\text{Air}}}\right) \cdot \alpha = 6.7945\,\text{mm} \tag{4.19}$$

$$\alpha = \frac{6.7945\,\text{mm}}{9\,\text{mm} + 141\,\text{mm} \cdot \left(\frac{n}{1.426}\right) + 150\,\text{mm} \cdot n} \tag{4.20}$$

Equation (4.20) only depends on the refractive index n of the respective sample. The primary calibration liquid that will be used in section 4.7 is a water-based solution and therefore possesses the same refractive index as water, which is 1.341 around 430 nm, and yields a vertical opening angle of $\alpha_{\text{H2O}} = 1.136°$. The other calibration sample is Cyclohexane itself, and results in an maximum angle of $\alpha_{\text{CHX}} = 1.070°$. In comparison, the purely geometrical approach would have resulted in $\alpha_{\text{Geo}} = 1.298°$. The uncertainty on these angles can now be calculated from the individual uncertainties on the cuvette radius (9.0 ± 0.45) mm, the path lengths within and outside the vat, (141 ± 1) mm and (150 ± 1) mm, as well as the slit height (13.589 ± 0.001) mm given by the manufacturer. Uncertainties on the various refractive indices were not considered.

In theory, the same procedure can now be used to access the corrected angle in horizontal direction, using the slit width $(1.8 \pm 0.01)\,\mathrm{mm}$ instead of the slit height. However, the formula would be much more complicated, as the curved surfaces of the cuvette and the vat have to be considered. At the same time, this very curved surface would result in a far smaller deviation from the purely geometrical expectation, as the light would hit the surfaces always roughly perpendicular, thus suppressing any refraction. It was therefore decided to instead use the geometrical angle of $\theta = 0.345°$ and apply an estimated uncertainty of 3% to this value.

Each of the aforementioned uncertainties has the power to shift the total Rayleigh scattering length up or down according to equation (4.14). In the worst case scenario, every contribution shifts the final result in the same direction without compensating each other. The total systematical uncertainty is therefore the sum of the individual deviations, which themselves are calculated by taking the product of the component's uncertainty ΔP and the partial derivative of Λ_{Ray} with respect to its respective parameter P:

$$(\Delta\Lambda_{\mathrm{Ray}})_{\mathrm{sys}} = \sum_i (\Delta P_i)_{\mathrm{sys}} \frac{\partial \Lambda_{\mathrm{Ray}}}{\partial P_i} \tag{4.21}$$

The statistical error rises from the uncertainties of all the measured intensities from both photomultipliers and across the two polarizations. Since the experiment operates in the photon counting region, the amount of measured light is simply represented by the dimensionless number of single photons detected within the time window (c.f. section 4.3). Since this number is Poissonian distributed, the uncertainty of each measurement can be easily calculated as the square root of the count number, $\sqrt{n}$. These uncertainties are then added quadratically according to Gaussian error propagation, in order to obtain the final statistical error on the Rayleigh scattering length. It should be noted that each measurement was preceded by a background estimation using Cyclohexane that was subtracted from the data. This background measurement also possesses a Poissonian uncertainty which was factored in as well.

$$(\Delta\Lambda_{\mathrm{Ray}})_{\mathrm{stat}} = \sqrt{\sum_i \left((\Delta I_i)_{\mathrm{stat}} \frac{\partial \Lambda_{\mathrm{Ray}}}{\partial I_i} \right)^2} \tag{4.22}$$

In conclusion, table 4.2 shows an overview of the various parameters and variables that give rise to the total uncertainty, each with its respective error:

	T_{Pol} @430 nm	OD @430 nm	x	θ	φ	Counted Photons
Value	0.9141	5.108	1.8 mm	0.0060	0.0373	n
Uncertainty	0.0005	0.016	0.9 mm / 5%	0.0002	0.0003	$\sqrt{n}$

Table 4.2: Values and uncertainties for the various parameters and variables used to calculate the Rayleigh scattering length. Wherever the calibration is wavelength-dependent, the value for 430 nm was chosen as an example.

4.7 Reference Samples

After the setup was assembled, but before the first proper scintillator measurements, it was decided to test the experiment using reference samples of known scattering lengths. To this end, a liquid was procured, which behaves as a perfect Rayleigh scatterer, i.e., its depolarization ratio is zero according to equation (4.5) as the horizontal polarization does not scatter at all. Furthermore, the wavelength-dependency of the Rayleigh scattering length follows a λ^4-function.

All the following information on the sample is taken from source [130] or from private communications with its author. The sample in question was a water-based colloidal suspension wherein Poly-n-Butylacrylamide-Polystyrene nanoparticles with a size of 68 nm were dispersed. The sample is therefore called PnBAPS68 but will henceforth only be referenced as "the colloid sample". These nanoparticles are perfectly spherical and reflective, ergo their only contribution to attenuation according to equation (4.2) is scattering, in particular Rayleigh scattering. This has been verified via a measurement with the UV/Vis-spectrometer, which is shown in figure 4.24. The attenuation length Λ_{Att} can therefore be directly equated with the Rayleigh scattering length Λ_{Ray} The extinction coefficient can be calculated according to:

$$\alpha = \rho_N \cdot \sigma_{\text{Scat}} = \rho_N \cdot \frac{24\pi^3 \cdot V_P^2 \cdot n_{\text{Med}}^4}{\lambda^4} \cdot \left(\frac{n_{\text{Rel}}^2 - 1}{n_{\text{Rel}}^2 + 2} \right)^2 \tag{4.23}$$

with the particle density ρ_N, the scattering cross-section σ_{Scat}, the particle volume $V_P = {}^4\!/_3 \pi r_P^3$ and the wavelength λ. Note the explicit λ^4-dependency that was previously mentioned. The parameters n denote the various refractive indices, with $n_{\text{Rel}} = 1.194$ being

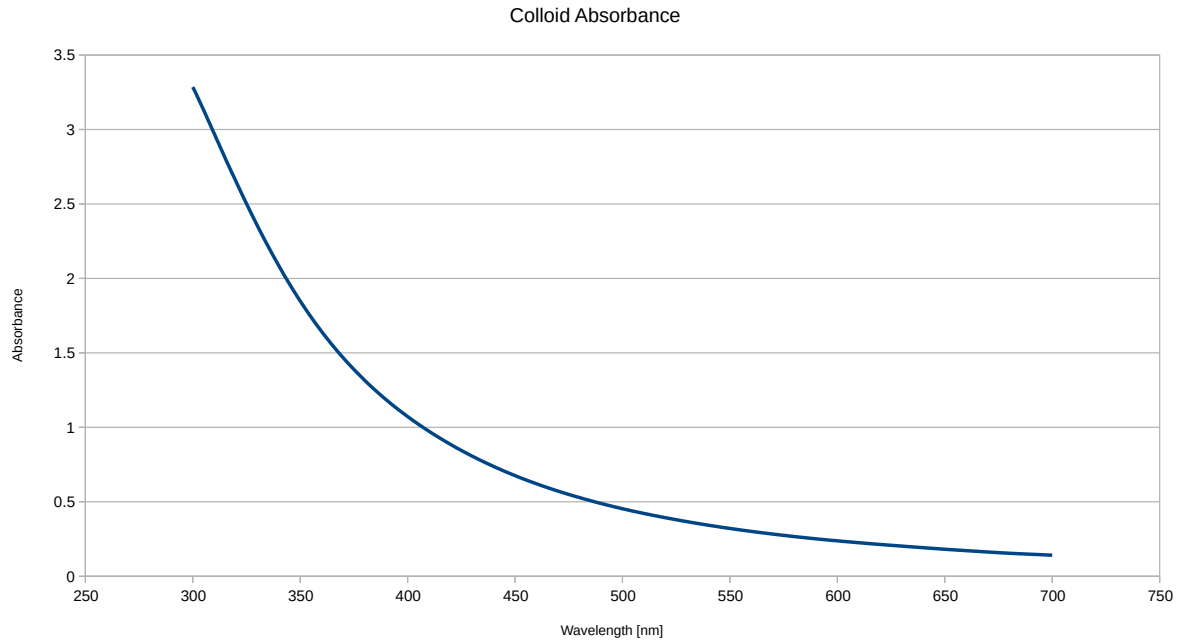

Figure 4.24: Absorbance spectrum of the PnBAPS68 colloid sample with a particle concentration of $5.8 \cdot 10^{18}\,\text{m}^{-3}$

the relative index between the particles and the medium. Since this value was measured using a laser at 632 nm, where water has an index of $n_{\text{Med}} = 1.333$ the particle's own refractive index can be calculated as $n_P = n_{\text{Med}} \cdot n_{\text{Rel}} = 1.592$. For the particles in question, this results in a cross section of $\sigma_{\text{Scat}} = 3.43 \cdot 10^{-17}\,\text{m}^2$ at 430 nm.

Since the procured sample had a concentration of $c = 5.8 \cdot 10^{18}\,\text{m}^{-3}$, the attenuation length – which in this case is equal to the Rayleigh scattering length – can be calculated as the inverse of the extinction coefficient in equation (4.23) and results in $\Lambda_{\text{Ray}} = 5.02\,\text{mm}$ for a wavelength of 430 nm. However, for various reasons, it was chosen not to use this concentration directly, but create from it several diluted samples which would then be analyzed instead. For one, a scattering length in the range of mm would already create a visible drop in beam intensity over the diameter of an 18 mm thick cuvette (as shown in figure 4.25), and therefore the assumption of each scattering center within the sample having an equal chance of emitting photons would no longer be valid. The second reasoning was purely practical, in that measuring diluted samples would still leave the majority of the original liquid untouched, in case of accidental contamination.

In total, five samples were prepared for analysis. The highest concentration, $c = 5.8 \cdot 10^{16}\,\text{m}^{-3}$, was still one hundredth of the original particle density, and each subsequent one was further diluted by a factor of 2, resulting in scattering lengths of 0.5 m, 1 m, 2 m, 4 m and 8 m, respectively. Since the colloid samples act as perfect Rayleigh scatterers, no contribution from the horizontal polarization is expected. Thus, all photons that were detected during this measurement were considered background events and their number subtracted from the counts obtained with the vertical polarization. Furthermore, the equation to determine the Rayleigh scattering length (4.14) can be simplified to:

$$\Lambda_{\text{Ray}} = x \cdot \ln^{-1}\left\{\frac{8\pi \cdot I_{\perp}(90°)}{3 \cdot \theta \cdot \varphi \cdot \langle I(0°)\rangle \cdot T_{\text{Pol}} \cdot 10^{OD}} + 1\right\} \tag{4.24}$$

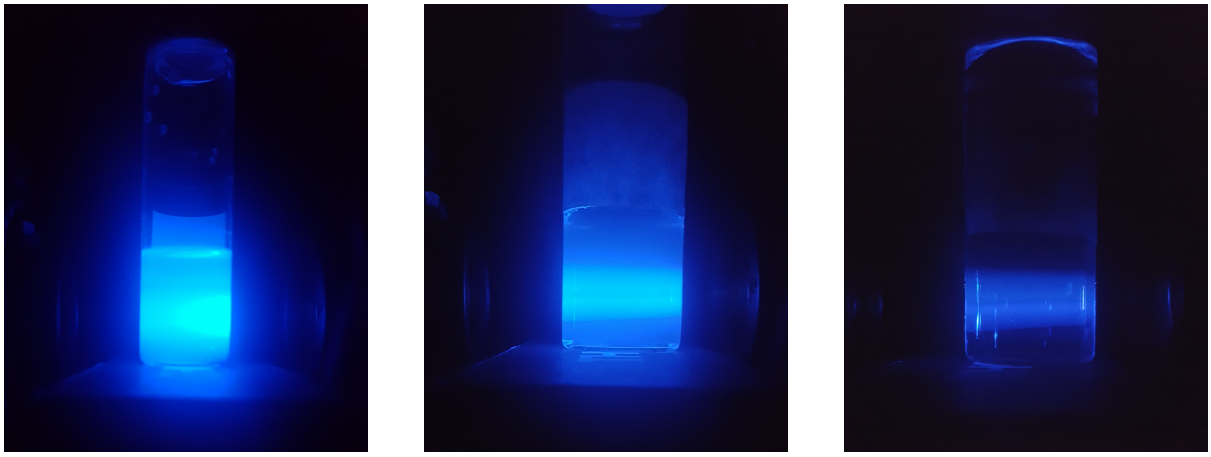

Figure 4.25: Colloid samples with various concentrations illuminated from the right. The leftmost picture shows the original sample with a concentration of $c = 5.8 \cdot 10^{18}\,\text{m}^{-3}$ and a Rayleigh scattering length of $\Lambda_{\text{Ray}} = 5.02\,\text{mm}$ at 430 nm. The next two pictures show dilutions with water in ratios of 1:10 and 1:100, yielding ten and a hundred times longer scattering lengths, respectively. Note the visible drop in intensity in the leftmost sample with a scattering length smaller than the diameter of the glass vial.

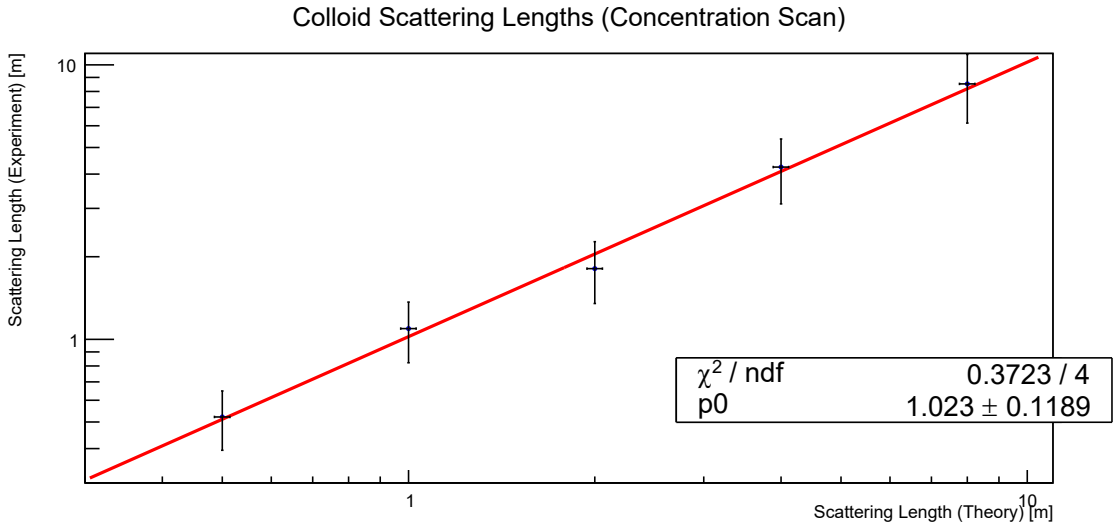

Figure 4.26: Measured Rayleigh scattering lengths at a wavelength of 430 nm versus their expected values for colloid samples of various concentrations. The higher the particle density, the lower the scattering length. The measurement is in good agreement with the expectation.

Figure 4.26 shows the obtained scattering lengths for the individual samples, plotted against their expected value, at a wavelength of 430 nm. The uncertainty for the theoretical expectation is determined by the wavelength precision of the experiment's monochromator ($\Delta\lambda = \pm 2\,\text{nm}$, c.f. subsection 4.4.1) as well as the uncertainty on the concentration during dilution, which was estimated to be on the 1% level. The linear fit function is in very good agreement with the identity relation, although this could be attributed to the relatively large error bars. Still, the scattering length values themselves also appear to be close to the expectation. All in all, it was considered a confirmation that the experiment is able to produce correct scattering lengths.

Next, the sample with the highest concentration ($c = 5.8 \cdot 10^{16}\,\text{m}^{-3}$) was selected to investigate the wavelength dependency, and whether the setup would be able to correctly determine the expected λ^4-behaviour. In total, five wavelengths were investigated: 400 nm, 415 nm, 430 nm, 450 nm and 470 nm. The results can be seen in figure 4.27. A function of the form $y = A \cdot x^B$ was used to fit the data, and the results for the exponent are in good agreement with the fourth power that is characteristic for Rayleigh scattering.

For reference, figure 4.28 shows the same measurement results plotted against the expected results in the same way that the concentration scan was performed. Unlike the concentration scan, however, this fit is barely not in agreement with the identity function. Since most of the scattering lengths are lower than their expectations, yet the sample still displays the correct wavelength-dependency, this points to an underlying systematic problem, like an error during the dilution process, rather than an issue caused by the measurement itself. As such, the setup is still considered to have passed both trials; the check for reproducibility of calculated Rayleigh lengths during the concentration scan as well as the investigation of correct λ^4-dependency in the wavelength scan.

It should also be noted that this plot was used to fine tune the error on the neutral density filters. To this end, the uncertainty was gradually increased until all error bars were large enough to enclose the fit function, which resulted in $\Delta OD = \pm 0.016$.

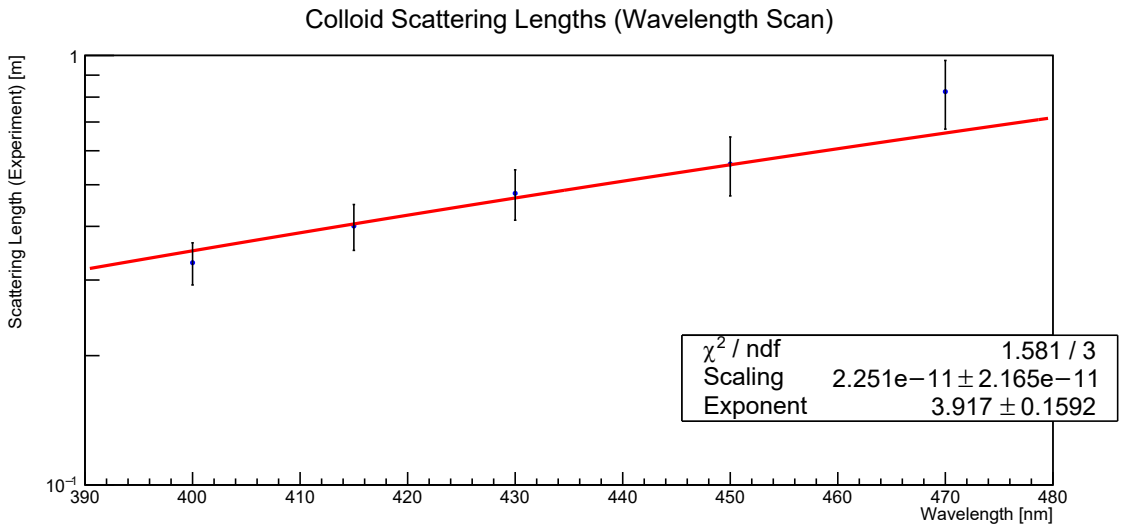

Figure 4.27: Measured Rayleigh scattering lengths versus the respective wavelength at which they were measured for a colloid sample with $c = 5.8 \cdot 10^{16}\,\mathrm{m}^{-3}$. The fit function correctly reproduces the expected λ^4-dependency.

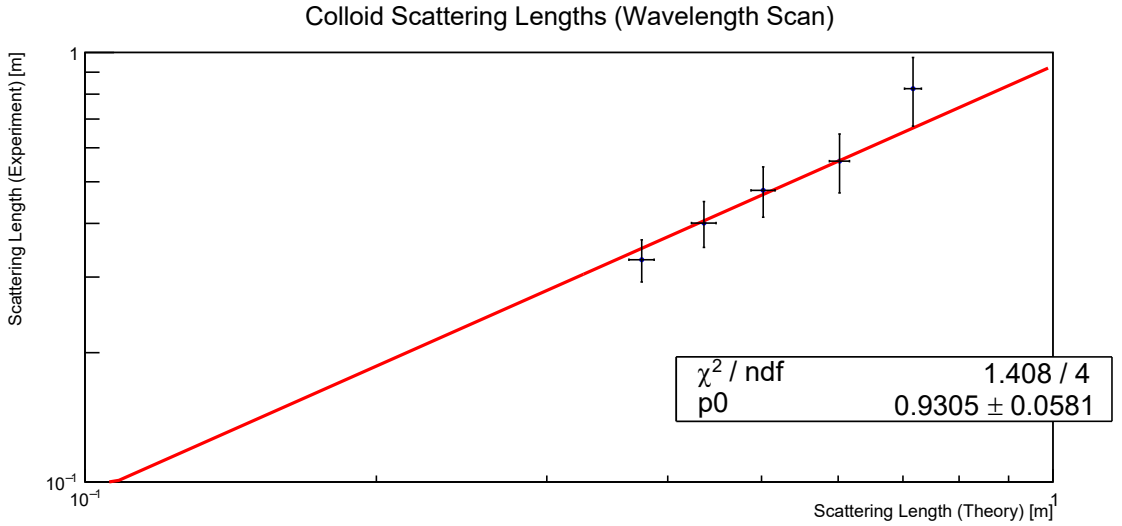

Figure 4.28: Measured Rayleigh scattering lengths at various wavelengths versus their expected values for a colloid sample with $c = 5.8 \cdot 10^{16}\,\mathrm{m}^{-3}$. The fit is barely not in agreement with the identity relation.

After having tested the experimental setup using a water-based colloid sample, it was decided to do another cross-check before starting with actual scintillators. The second type of reference liquid was chosen to be Cyclohexane (CHX), the very same chemical that is already used in the setup for index-matching (c.f. section 4.2). CHX is very similar to liquid scintillators in that it is an organic compound with a similar refractive index, so it works as a good trial run for the experiment. CHX also happens to be a perfect Rayleigh scatterer just like the colloids and has a known scattering length of 44 m at a wavelength of 430 nm.[131] Although it should be noted that this literature value refers to the chemical in general and the scattering length of this specific CHX sample might differ due to impurities.

The measurement process was identical to the one conducted for the colloid samples: Single photons were counted for both horizontal and vertical polarization, whereby the former were considered to be background only and thus subtracted from the latter. Ergo, the same simplified formula (4.24) can be used to obtain the Rayleigh scattering length.

Figure 4.29 shows the wavelength dependency of the CHX results while figure 4.30 shows the results in comparision to the theoretical expectation, which was calculated from the literature value of $\Lambda_{\text{Ray}}^{\text{CHX}}(430\,\text{nm}) = 44\,\text{m}$ via λ^4-dependency. The experiment is once again able to correctly reproduce the correct exponent in the $y = A \cdot x^B$ fit function and the measured values are in good agreement with the theory. Although it should be noted that such a long Rayleigh scattering length did result in few photon counts in the scatter-PMT, which in turn is responsible for the large error bars, as the uncertainty is mostly dominated by statistics, especially at high wavelengths where the scattering length rises even further.

The total number of counted photons for all samples at all investigated wavelengths including their respective Rayleigh scattering lengths and each statistical and systematical error can be found in Appendix B.

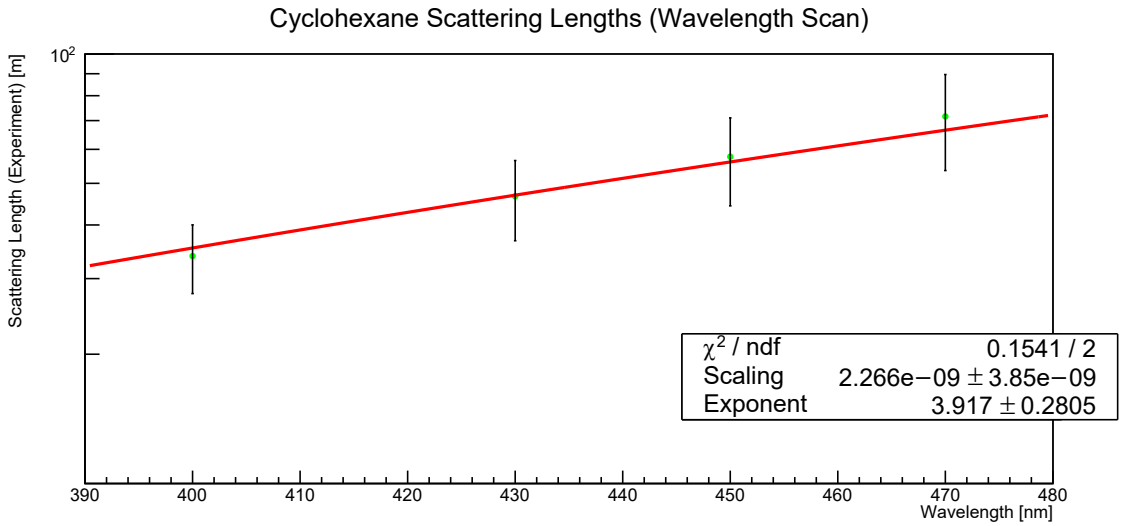

Figure 4.29: Measured Rayleigh scattering lengths versus the respective wavelength at which they were measured for Cyclohexane. The fit function correctly reproduces the expected λ^4-dependency.

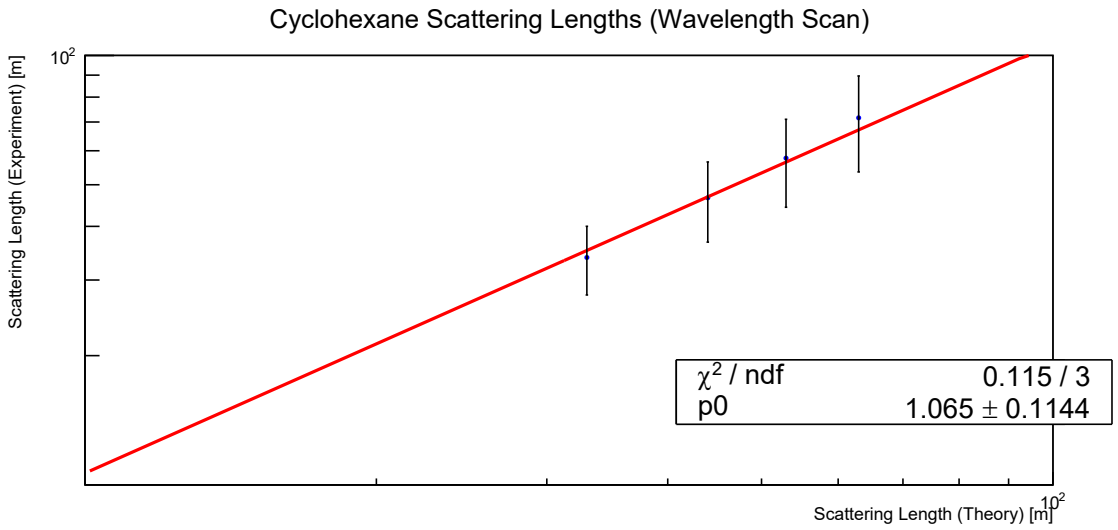

Figure 4.30: Measured Rayleigh scattering lengths at various wavelengths versus their expected values for Cyclohexane. The fit is in agreement with the identity relation.

4.8 Scintillator Results

Measuring actual liquid scintillators is different from the previously mentioned reference samples in that they are no longer ideal Rayleigh scatterers. As such the scattered light does actually contribute to the horizontal polarization, which can therefore no longer be assumed to comprise background events only. This required a dedicated background measurement with Cyclohexane (CHX) to accompany each individual scintillator measurement at every single wavelength. Thus, for every investigated Rayleigh length, three different sets of data had to be taken: First, the sample itself, measured in vertical polarization; Second, the sample again, in horizontal polarization; Third, a sample of CHX, measured at horizontal polarization. As CHX is an ideal Rayleigh scatterer, all pulses detected during the third measurement are assumed to be background only and their number subtracted from the scintillator counts. Therefore, all three measurements were conducted with the same amount of statistics so as to be directly comparable. Furthermore, the data taking was performed consecutively in order to avoid potential changes in the experiment's environment or the components themselves (such as the lamp's intensity).

The first liquid to be investigated was a sample of commercial sales LAB from the Nanwan Chemical Co., Ltd. located in Nanjing, China, provided by the Institute of High-Energy Physics (IHEP) in Beijing. Just like the calibration samples, it was measured at five different wavelengths: 400 nm, 415 nm, 430 nm, 450 nm and 470 nm. The results can be seen in figure 4.32. Note that the plot only shows the statistical uncertainties. The data does seem to follow a λ^n-dependency for higher wavelengths, although the fit does not yield an $n = 4$ result. Similarly, the Rayleigh lengths deviate significantly from the expectation in the lower range, which is assumed to be caused by a contaminant that absorbs in this region. For this reason it was decided to fit the lower end of the data using a Breit-Wigner formula, which describes behaviour near a resonance peak:

$$f_{\mathrm{BW}}(\lambda) = C \cdot (\lambda^2 - \lambda_{\mathrm{Res}}^2)^2 \tag{4.25}$$

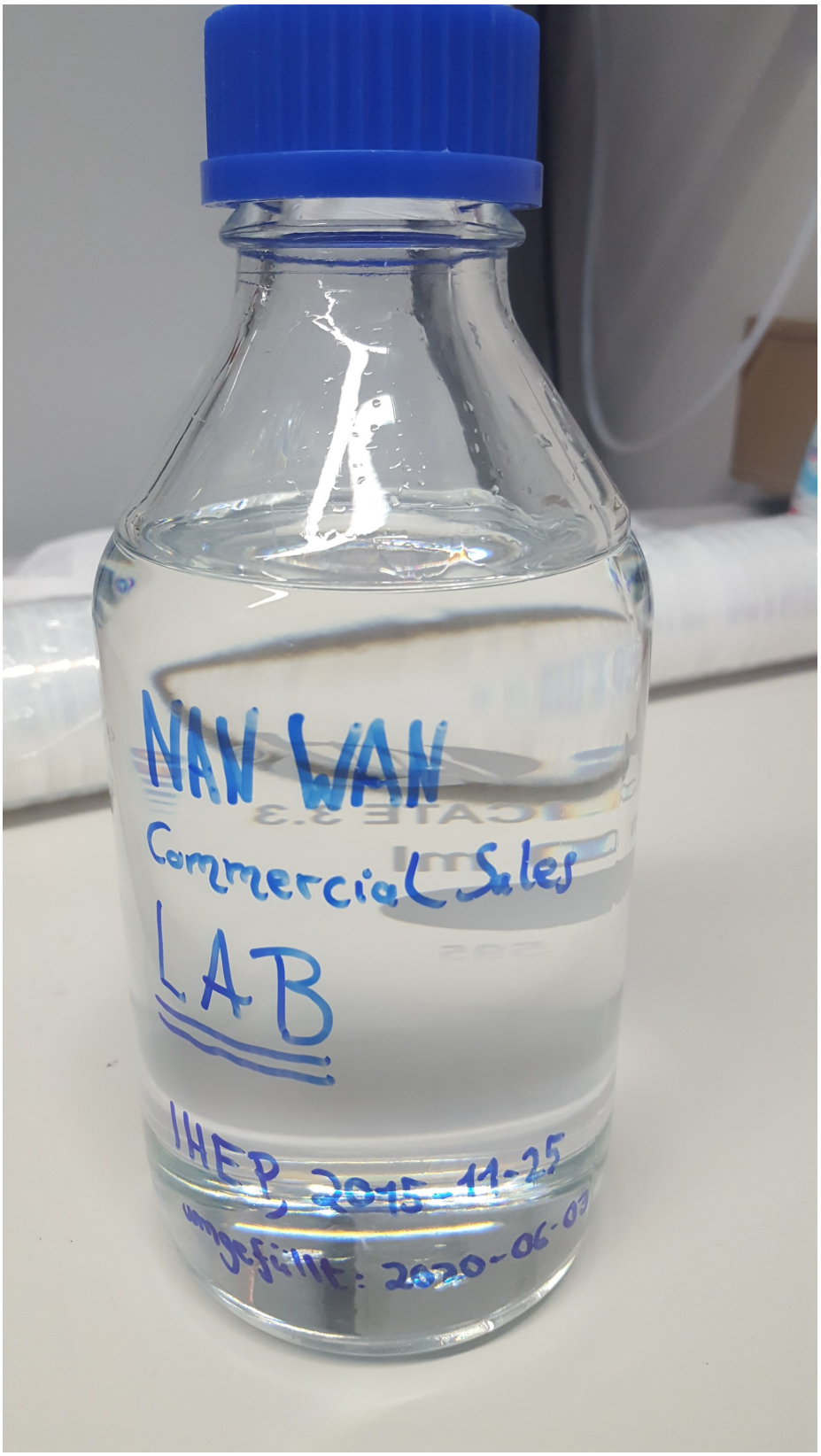

Figure 4.31: The bottle of chinese Nanwan Linear Alkyl Benzene liquid scintillator from where samples were taken for the Rayleigh scattering length measurement.

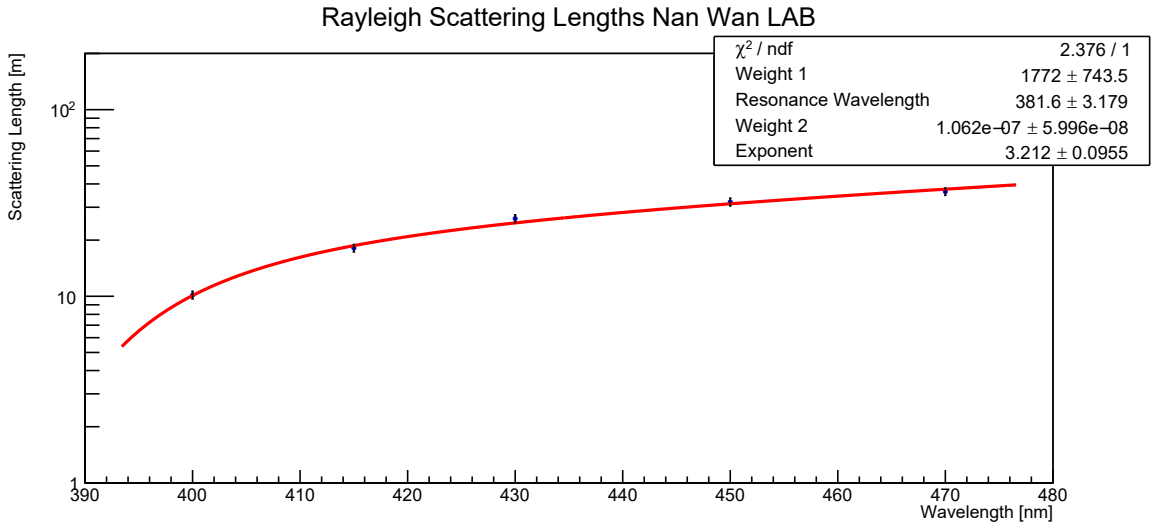

Figure 4.32: Rayleigh scattering lengths of the Nanwan sample. The data was fitted with a combined λ^n-function at the high end and a Breit-Wigner resonance formula at the low end.

The original Breit-Wigner formula describes rising resonances in energy space and has the variable in the denominator of a fraction. Since the fit is intended to model a falling resonance in wavelength space, the reciprocal was used. Furthermore, the Breit-Wigner distribution possesses some additional correction terms that depend on the resonance width, which had to be left out of the fit as they would have introduced too many parameters for just five data points. As the data taking requires several days per Rayleigh scattering length, it was decided to forego the correction terms. However, upgrading the experiment to speed up data taking would allow to obtain enough data points in a feasible time frame to reintroduce them in the future.

For the total fit, the Breit-Wigner formula and the monomial function need to be combined in a way that the *lower* of the two is dominant, so they are added reciprocally:

$$\frac{1}{f_{\text{fit}}(\lambda)} = \frac{1}{f_{\text{BW}}(\lambda)} + \frac{1}{f_{\text{Mono}}(\lambda)} \tag{4.26}$$

The resulting fit parameters hint at a resonance somewhere below 400 nm that affects the two lower data points. While the combined fit only yields an exponent of 3.26 ± 0.08 for the monomial part, it should be noted that the three topmost data points are well in agreement with λ^4 if fitted independently and the parameter is likely dragged down by the transition region. This is supported by the results for the depolarization ratio δ from equation (4.5), which is expected to be ~ 0.30 for LAB[120]. The sample shows a value around $\delta \simeq 0.18$ (c.f. table B.4) for higher wavelengths – which is lower than the expectation yet consistent – but rises sharply when approaching 400 nm, supporting the argument of a contamination. The difference in depolarization ratio from the expectation could be explained by variations in the chemical composition, as LAB is not a homogeneous liquid but a mixture of several molecules that all possess Benzene rings but differ in the length of the attached carbon chains (c.f. section 3.3). Furthermore, the Breit-Wigner formula assumes one single resonance peak whereas in reality, absorption occurs over a broader spectrum, so the equation should only be seen as an approximation.

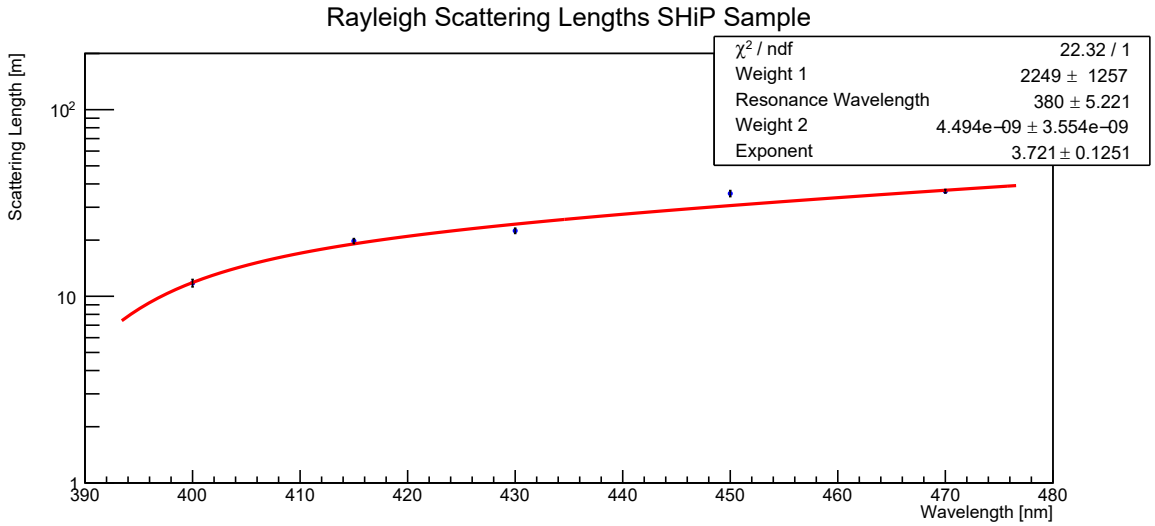

Figure 4.33: Rayleigh scattering lengths of the SHiP sample. The data was fitted with a combined λ^n-function at the high end and a Breit-Wigner resonance formula at the low end.

A second liquid was then investigated as a comparison to the Nanwan sample: Scintillator from the SHiP experiment[132] that had been purified using an aluminium (Al_2O_3) column in order to remove optical impurities. Originally the sample consisted of 1.5 g/l PPO solved in LAB from the chemical company SASOL,[133] however, the majority of the wavelength shifter should be removed by the purification column. The sample was measured at the same five wavelengths with the same amount of statistics as the Nanwan LAB to be comparable.[134] The fitted results can be seen in figure 4.33.

While the data points are more unstable than in the previous sample and the fit does not pass through all (statistical) error bars, the exponent in the monomial function is much closer to $n = 4$, yet still not entirely within the uncertainty. Once again the Rayleigh scattering length drops when approaching 400 nm, although this time only the lowest data point is affected. The depolarization ratio shows a value close to 0.3 (c.f. table B.5) for the higher wavelengths – except for the result at 450 nm, which hints at a measurement error given that the Rayleigh length at that point is also outside the fit function – and once again rises sharply at the lower end. Similarly to the Nanwan sample this drop could be explained by an unwanted contamination, but in the case of the SHiP scintillator specifically might also be caused by PPO remnants that survived the aluminium column.

Although the SHiP sample seems to be less affected by possible contaminants, it still shows a resonance behaviour around 380 nm just as the Nanwan LAB does. In order to exclude an error of the Rayleigh scattering measurement itself, both liquids were cross-checked with respect to their transparency using a UV/Vis-spectrometer. More specifically, for each type of liquid, one sample was taken directly out of the Rayleigh scattering setup while a second one was drawn from the original bottle for comparison. While the spectrometer only measures the absorbance of a sample – which is defined the same way as the optical density in equation (4.8) – it can be converted to an attenuation length (c.f. equations (4.1) and (4.2)) using a reference measurement with the empty cuvette.[135] The results are shown in figure 4.34.

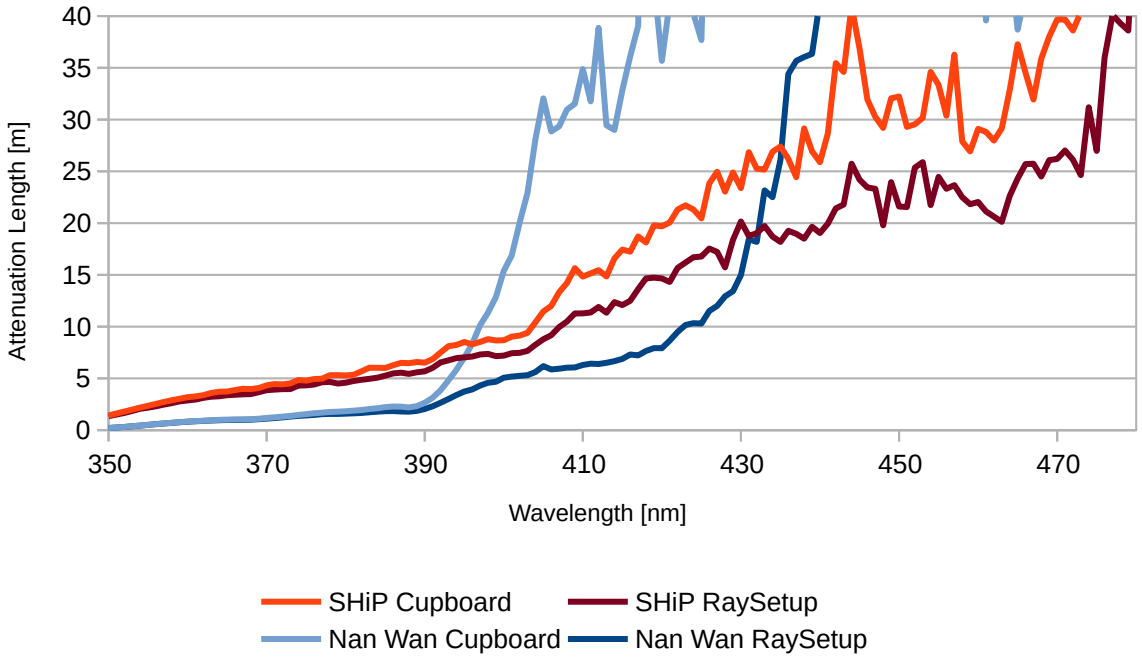

Figure 4.34: Attenuation Lengths of the Nanwan and SHiP samples. "RaySetup" refers to the liquids directly taken from the Rayleigh experiment while "Cupboard" denotes new samples taken from the original bottle. Above $\sim 25\,\mathrm{m}$ the results become unstable.

Immediately visible is the big discrepancy between the Nanwan sample from the Rayleigh scattering setup and the new sample from the bottle. Where the new sample reaches high values in attenuation length at $\sim 400\,\mathrm{nm}$ and above, the sample investigated for Rayleigh scattering only clears up after $\sim 430\,\mathrm{nm}$, indicating a contamination in the wavelength region below. While this supports the measured Rayleigh scattering lengths from before, it also shows that the sample in question was not properly handled when it was taken.

A similar difference in attenuation length is also visible in the SHiP scintillator, although to a smaller degree than the Nanwan LAB. Nevertheless, both curves exhibit a bend at $\sim 405\,\mathrm{nm}$ after which the transparency increases faster than before. This behaviour agrees with the Rayleigh length measurements which showed a deviation from the expected behaviour only for the $\sim 400\,\mathrm{nm}$-value. Since both samples show this trend, it is unclear what causes this behaviour. Possible culprits are the liquid itself, PPO remnants or an unknown contaminant that was not purged by the aluminium column. However, even the clean Nanwan sample shows a similar bend at $\sim 390\,\mathrm{nm}$, so it might be an inherent property of the scintillator.

Furthermore, attention should be drawn to the fact that the attenuation length results get unstable after rising above $\sim 25\,\mathrm{m}$, most likely due to the limited sensitivity of the spectrometer. The measurements were conducted using $1\,\mathrm{cm}$-cuvettes as there was not enough liquid from the Rayleigh scattering setup to fill a larger $10\,\mathrm{cm}$ one, so in theory the sensitivity could be raised with more sample liquid. Even then, however, the spectrometer will most likely reach its limits rather quickly, stressing the need for dedicated laboratory setups to investigate LS purity, such as the herein mentioned Rayleigh scattering experiment.

In conclusion, the attenuation length cross-check using the spectrometer supports the results obtained from the experiment and the measured Rayleigh lengths are assumed to be correct. In that case, the LAB sample from Nanwan possesses a Rayleigh scattering length of $(26.1 \pm 1.2_{\text{stat}} \pm 2.6_{\text{sys}})$ m at 430 nm which rises to $(36.4 \pm 1.6_{\text{stat}} \pm 3.6_{\text{sys}})$ m at 470 nm in accordance with λ^4-dependency. These results are in good agreement with results of pure LAB measurements conducted by other groups, such as (28.2 ± 1.0) m @ 430 nm[120], (27.0 ± 2.3) m @ 430 nm[124] or (27.9 ± 2.3) m @ 430 nm and (40.2 ± 3.3) m @ 470 nm[136]. The SHiP sample shows similar Rayleigh lengths in the same region, ranging from $(22.4 \pm 0.7_{\text{stat}} \pm 2.2_{\text{sys}})$ m at 430 nm up to $(36.5 \pm 0.8_{\text{stat}} \pm 3.5_{\text{sys}})$ m at 470 nm.

Chapter 5

OSIRIS

With its 20 kt central volume across 35.4 m in diameter (c.f. section 2.1), the JUNO detector has high purity requirements. While the optical transparency was already addressed in chapter 4, other stringent limits are also set on intrinsic radioactivity of the detector materials, specifically the liquid scintillator (LS) itself. Radioactive decays have the ability to produce fake signals that mimic the energy and time distribution of inverse beta decays by which neutrino events are identified (see section 2.2). Removing unstable isotopes reduces the number of background events possibly misidentified as neutrino signals, so several purification systems are set in place to clean the LS prior to filling into the central detector (CD) volume and during cleaning cycles throughout JUNO's operation: An aluminium (Al_2O_3) purification column is meant to clear the scintillator from optical impurities while fractional distillation, water extraction and gas stripping aim to purge unwanted radionuclides.[74]

In order to gauge the remaining concentration of radioactive isotopes in the liquid, a pre-detector has been envisioned: The Online Scintillator Internal Radioactivity Investigation System (OSIRIS) is a monitoring device designed to not only measure the amount of radioactive decays in the LS, but also serve as a fail-safe system and issue a warning in case of high amounts of unwanted contaminants that made it past the purification plants. In such an event, it is possible to quickly stop the CD filling process and thus preventing contamination of the already filled scintillator. It is therefore intended to be installed at the last possible position in the JUNO filling line, after the purification systems and just before the filling and overflow tanks at the chimney of the detector, so no subsequent stations in the filling line have the opportunity of contaminating the LS after it has already passed OSIRIS (c.f. figure 5.1).

As a means to assess the feasibility and sensitivity of such a device, a `Geant4`-simulation has been written that allows to study its performance by employing Monte Carlo methods when replicating radioactive decays within and outside of the OSIRIS detector volume from various decay chains and isotopes. The sensitivity of the system has then been analyzed with custom-made software using `CERN root`, taking into account photomultiplier (PMT) detection efficiency and energy resolution. The goal of the study was to find a suitable design that is able to reach concentration sensitivities of 10^{-16} g/g, satisfying JUNO's solar neutrino detection requirements (c.f. section 5.1). To this end, different types of component dimensions, thicknesses, alignments and materials were investigated to determine the optimal layout of the OSIRIS detector for it to achieve its goal. A fiducial volume cut in the LS tank has been introduced in order to reduce ex-

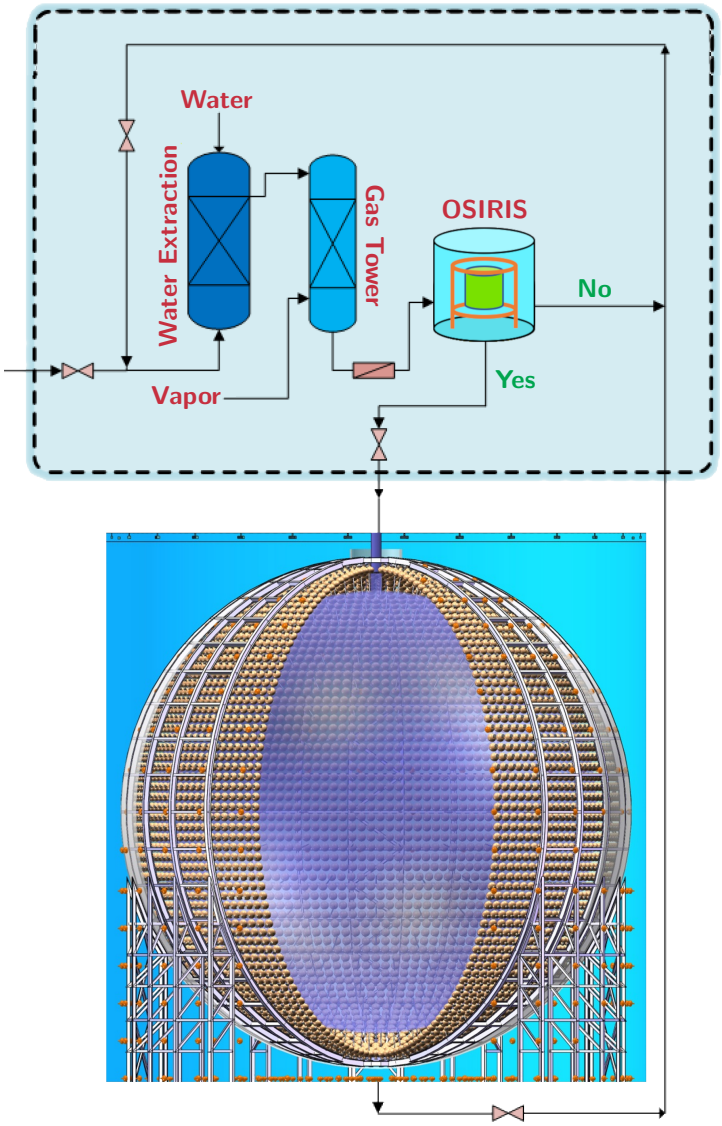

Figure 5.1: Location of the OSIRIS detector within the JUNO filling line, in relation to the purification plants and the chimney of the detector where the filling and overflow tanks are located.

ternal background events while energy and time cuts have been put in place to reduce accidental coincidences and thus maximize the sensitivity of OSIRIS to the radioactivity of the contaminants within the JUNO LS.

5.1 Concept

The overall purpose of the OSIRIS detector is to help JUNO reach the radiopurity requirements for various neutrino detection channels in order to achieve its physics goals (c.f. section 2.4). Specifically, the purity requirements of the solar neutrino analysis have been chosen as the target sensitivity, as it is the most stringent limit across all physics programs. Generally speaking, the baseline purity required for solar neutrinos is one or-

Internal Radiopurity Requirements		
Isotope	Baseline	Optimal
^{210}Pb	$5 \cdot 10^{-25}$ g/g	$1 \cdot 10^{-25}$ g/g
^{85}Kr	500 cts/d/kt	100 cts/d/kt
^{238}U	$1 \cdot 10^{-16}$ g/g	$1 \cdot 10^{-17}$ g/g
^{232}Th	$1 \cdot 10^{-16}$ g/g	$1 \cdot 10^{-17}$ g/g
^{40}K	$1 \cdot 10^{-17}$ g/g	$1 \cdot 10^{-18}$ g/g
^{14}C	$1 \cdot 10^{-17}$ g/g	$1 \cdot 10^{-18}$ g/g
Cosmogenic Background Rates		
^{11}C	1860 cts/d/kt	
^{10}C	35 cts/d/kt	

Table 5.1: Radiopurity requirements in JUNO for solar neutrino detection. The requirements for antineutrino detection (e.g. for mass ordering determination using reactor electron antineutrinos) are two orders of magnitude more lenient in the cases of ^{238}U, ^{232}Th and ^{40}K with respect to the optimal solar radiopurity. [74, 75]

der of magnitude better than for reactor antineutrinos, while the optimum is even two orders of magnitude lower.[74] The exact numbers for various isotopes and decay chains are given in table 5.1.

While all isotopes need to be below their respective limits for the physics programs to be realizable, the initial design study for OSIRIS focused on reaching the target sensitivity for just one decay chain in particular as a proof of concept. This was chosen to be the ^{238}U chain, for several reasons: First, OSIRIS intends to monitor the radioactive contamination of the LS via a coincidence measurement, and this decay chain includes the $^{214}\text{Bi} \rightarrow {}^{214}\text{Po} \rightarrow {}^{210}\text{Pb}$ sequence of consecutive decays, which is a powerful tool to suppress accidental coincidences by other backgrounds with its short lifetime ($\tau(^{214}\text{Po}) = 236.6\,\mu\text{s}$) and monoenergetic delayed event. Secondly, it is also the most common contamination to appear in the LS, as contact with air due to a leak will introduce ^{222}Rn into the mix, which is part of the Uranium series and will eventually decay to ^{214}Bi.

Implementing energy and time cuts on the distinct BiPo-signal being investigated, OSIRIS will then be able to use the number of detected decays in the LS volume to draw conclusions on the ^{214}Bi concentration in the scintillator and thus, by extension, also on other contaminants in the same decay chain. It is assumed that for the intrinsic LS radioactivity, all nuclides from the decay chain have reached secular equilibrium, so the concentration of ^{214}Bi can be translated directly into the concentration of ^{238}U (and similarly for all nuclides in between) (c.f. section 5.6). While this does not necessarily hold true for a recent contamination with Radon due to an air leak late in the LS filling line, ^{222}Rn has a sufficiently short lifetime of 5.5 days with its subsequent daughters decaying on timescales of minutes, so an excess in Radon should still be immediately visible as a rise in Bi-Po-events.

Although not covered in the scope of this thesis, the final detector will also be able to identify contaminations with other isotopes, such as ^{14}C, ^{210}Pb, cosmogenic ^{9}Li, ^{8}He and ^{11}C as well as isotopes from the ^{232}Th decay chain, the latter of which has an equivalent fast decay, namely $^{212}\text{Bi} \rightarrow {}^{212}\text{Po} \rightarrow {}^{208}\text{Pb}$ ($\tau(^{212}\text{Po}) = 431.4\,\text{ns}$), that can be used as a coincidence signal to gauge the concentration of radionuclides from this decay chain.

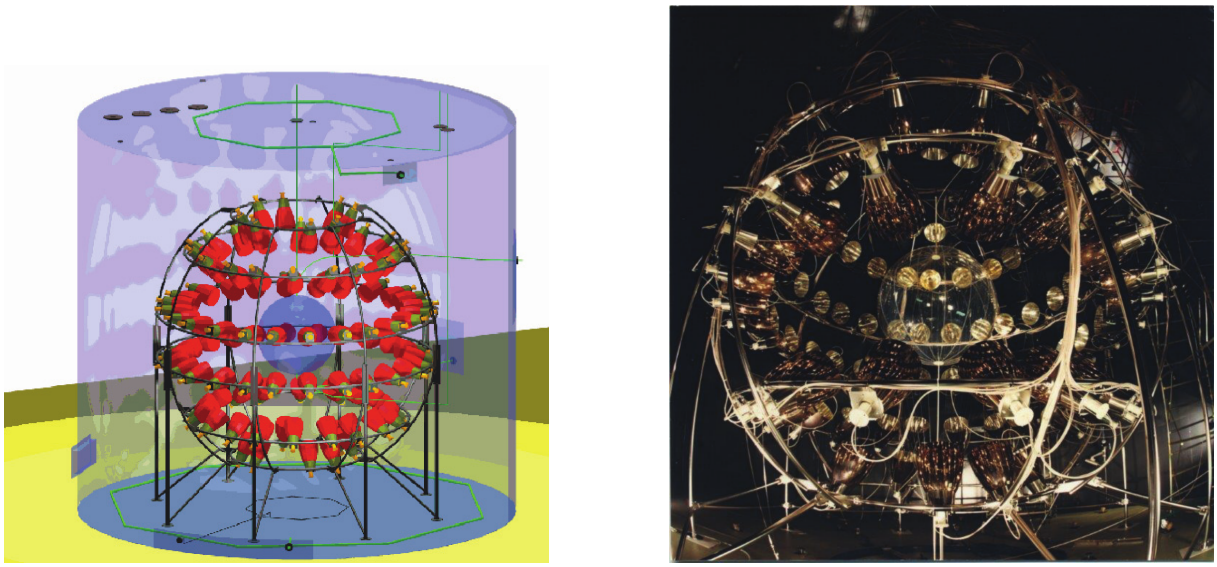

Figure 5.2: Left: A sketch of the Counting Test Facility. Right: A photo of the CTF detector from within the outer tank. [137]

5.2 The Counting Test Facility

The overall design of the OSIRIS detector is heavily inspired by the Counting Test Facility (CTF) at the Laboratori Nazionali del Gran Sasso (LNGS) that operated from 1995 to 2010, which itself served as a proof of concept to see if purities required for neutrino detection inside liquid scintillators could even be reached.[137] As such, the CTF was a crucial step in the creation of the Borexino detector and can be seen as its spiritual predecessor. In terms of radiopurity, the CTF was able to reach levels up to $1 \cdot 10^{-16}$ g/g for ^{238}U and ^{232}Th as well as a ^{12}C/^{14}C ratio of $1 \cdot 10^{-18}$ g/g.[138]

The detector itself consisted of an amorphous nylon sphere ($\varnothing = 2\,\mathrm{m}, d = 0.5\,\mathrm{mm}$) to contain a 4.8 m^3 volume of the Borexino liquid scintillator mixture (Pseudocumene + 1.5 g/L PPO), held in place by a stainless steel structure onto which 100 8"-PMTs (Thorn EMI 9351) were mounted. All of this was submerged in a cylindrical tank ($\varnothing = 11\,\mathrm{m}, h = 10\,\mathrm{m}$) filled with 1 kt pure water, providing ~ 4.5 m shielding against external radiation. A sketch and a photo of the CTF detector are shown in figure 5.2. [137, 139]

Several radioactive background analyses for the LS mixture were performed with the CTF facility. The ^{238}U chain was measured by means of the ^{214}Bi-^{214}Po decay, with a coincidence time window of $2\,\mu\mathrm{s} < t < 710\,\mu\mathrm{s}$, which OSIRIS has adopted. Similarly, the ^{212}Bi-^{212}Po decay was used with a $t < 2\,\mu$s time cut to determine the ^{232}Th contamination. Other investigated nuclides were ^{14}C, ^{85}Kr and the non-secular-equilibrium ^{210}Po.

In 2000, the CTF was refurbished for monitoring the Borexino scintillator before filling: The PMTs that had broken in the years prior were replaced and a second nylon vessel was inserted between the PMTs and the central scintillator volume, to hold back Radon-contaminated water. The low radioactivity levels from the initial operation period were reproduced, giving green light for the Borexino filling. This usage was the inspiration for the OSIRIS radioactivity monitor concept, although with one key difference: While the CTF separately measured but a sample of the total solution, OSIRIS intends to operate in continuous mode as a part of the JUNO filling chain proper. [137]

5.3 Evolution of the OSIRIS Detector

The initial OSIRIS simulation was programmed in `Geant4` 9.6p4[140] with additional features of `CERN root` 5.34/23[141] (file saving management, etc.) in which the analysis software was coded as well. (The simulation has since moved to `Geant4` 10.2p3[142] after the analyses covered in this thesis were performed.) More specifically, the simulation was based on a stripped-down and then modified version of the Novice example simulation N01[143] (later discontinued from `Geant4` 10 onwards) that is meant to illustrate the most fundamental classes that `Geant4` needs in order to successfully create a test particle (self-referentially called a "geantino") and propagate it through a previously defined detector geometry. For OSIRIS, this geometry was changed according to the design stages the detector passed through as time went on and more physics, particles and general features were added piecemeal when the simulation evolved in complexity and scope. The current section not only provides a quick overview of the individual stages of the OSIRIS detector design but also denotes the individual additions to the simulation code at each step.

5.3.1 Minimal Working Example

The first iteration of the OSIRIS simulation was basically identical to the `Geant4` Novice example N01, with the only difference being the change of the geometry to a cylindrical tank following the very first concept of the detector as a repurposed storage tank. It mainly consisted of a steel cylinder vessel ($\varnothing = 19\,\mathrm{m}, h = 12.5\,\mathrm{m}, d = 6\,\mathrm{mm}$) filled with LAB as a liquid scintillator whose walls were then covered with 20" PMTs modeled as a half-sphere made of solid borosilicate. Properties of the used materials have been taken from the LENA simulation. Since the OSIRIS simulation was meant to determine the optimal detector dimensions for a radioactivity monitor it needed to be automatically scalable when changing individual detector dimensions such as height or width on the fly. This version of the simulation was thus meant to serve as a Minimal Working Example (MWE) of the geometry construction and was primarily used to test the automatic PMT placement code which is why the PMTs were still one solid object without internal structure and had no spacing from one another. The geometry of the MWE can be seen in figure 5.3. No actual particle simulations and analyses were performed at this stage yet.

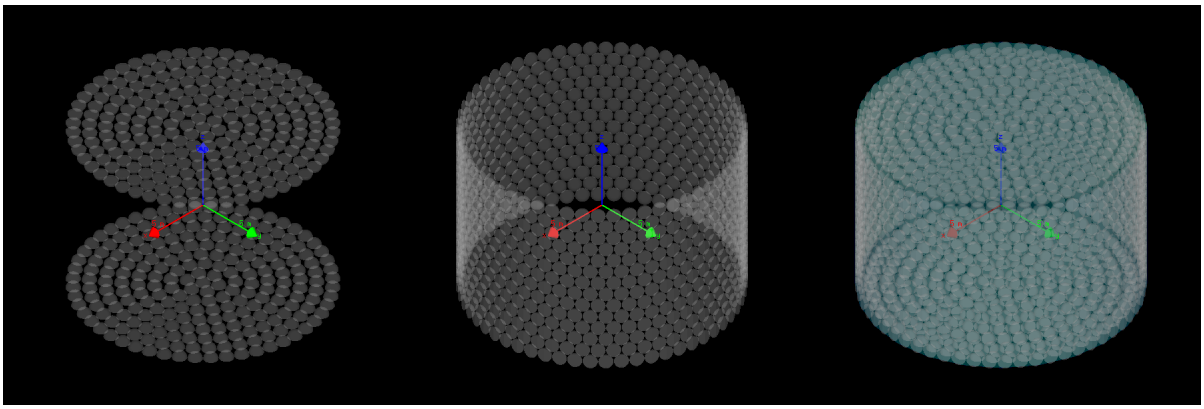

Figure 5.3: The MWE of the earliest version of the OSIRIS simulation (right). This code was meant to test the automatic PMT placement along the wall (middle), floor and ceiling (left).

5.3.2 Single Tank Version

Early designs of the OSIRIS detector intended to improve upon the CTF concept by trying to completely remove buoyancy forces, thus allowing to fully drain the LS without the risk of an implosion. The very first design study didn't have a water shielding at all, rather it was a cylindrical steel tank ($\varnothing = 19\,\mathrm{m}, h = 12.5\,\mathrm{m}$) with $d = 6\,\mathrm{mm}$ thick walls that was directly filled with LS. This concept would have allowed to test $\sim 670\,\mathrm{t}$ of LS at a time over the three months projected for JUNO filling. The idea initially was to dual-purpose one of the preexisting storage, filling or overflow tanks and mount the PMTs on the inside of the walls in order to instrumentalize it as a radioactivity detector. However, it turned out that none of the tanks on site was large enough, so this idea was discarded and a new dedicated tank for monitoring the LS contamination was soon envisioned.

The geometry changed significantly once the simulation became more elaborate and moved on to actually simulate physical particles within the detector. The tank radius and height were reduced ($\varnothing = h = 10\,\mathrm{m}$) to provide a feasible starting point for to-be-investigated dimensions, although wall thickness stayed the same ($d = 6\,\mathrm{mm}$). The PMTs were now modeled as an ellipsoid with a cylindric base filled with vacuum, with a window thickness of 1 mm. The PMT dimensions ($a = b = 254\,\mathrm{mm}, c = 184\,\mathrm{mm}, h_{\mathrm{PMT}} = 523\,\mathrm{mm}, r_{\mathrm{Trunk}} = 60\,\mathrm{mm}$) were taken from the JUNO simulation. Furthermore, six horizontal lines with 23 PMTs each were distributed across the tank wall, with an additional 31 PMTs on both floor and ceiling each for a total of 200 photmultipliers in the detector. The outer tank was also surrounded by 60 cm of rock (simulated as concrete) to all sides as a source for external gammas that would penetrate OSIRIS at the JUNO site. The geometry can be seen in figure 5.4.

The type of primary particles simulated was changed to high-energy gammas being created in one of three possible volumes: The external rock mantle, the steel tank or the PMT glass. From each of these points of origin, gammas from ^{40}K as well as the ^{238}U and ^{232}Th decay chains (c.f. figures 5.6 and 5.7) were simulated, with the former being a monoenergetic 1.4 MeV line and the latter being randomly chosen from the distribution of the various gamma energies of each series[144] as shown in figure 5.5. The gammas then propagate through the different materials and the simulation records the Monte Carlo

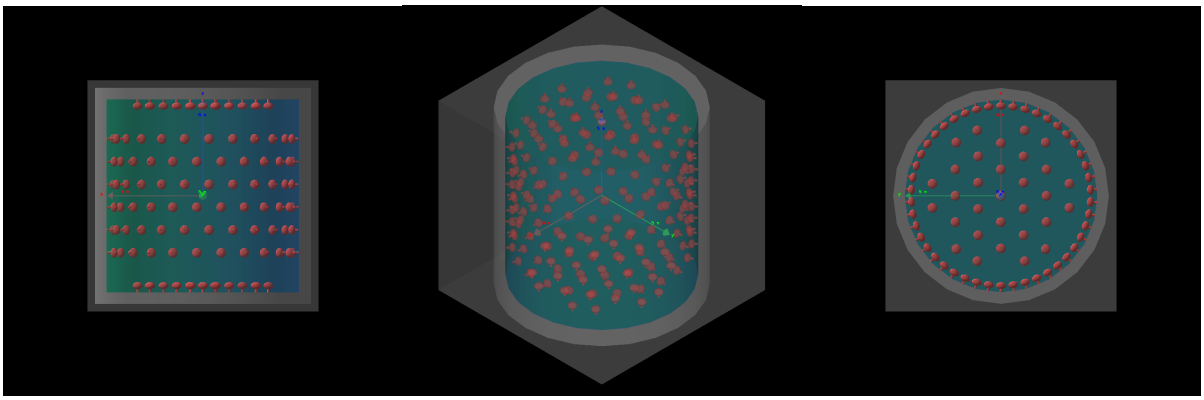

Figure 5.4: The first version of the OSIRIS simulation actually capable of generating high-energy gamma particles, propagating them through the detector and recording their points of interaction with the surrounding material.

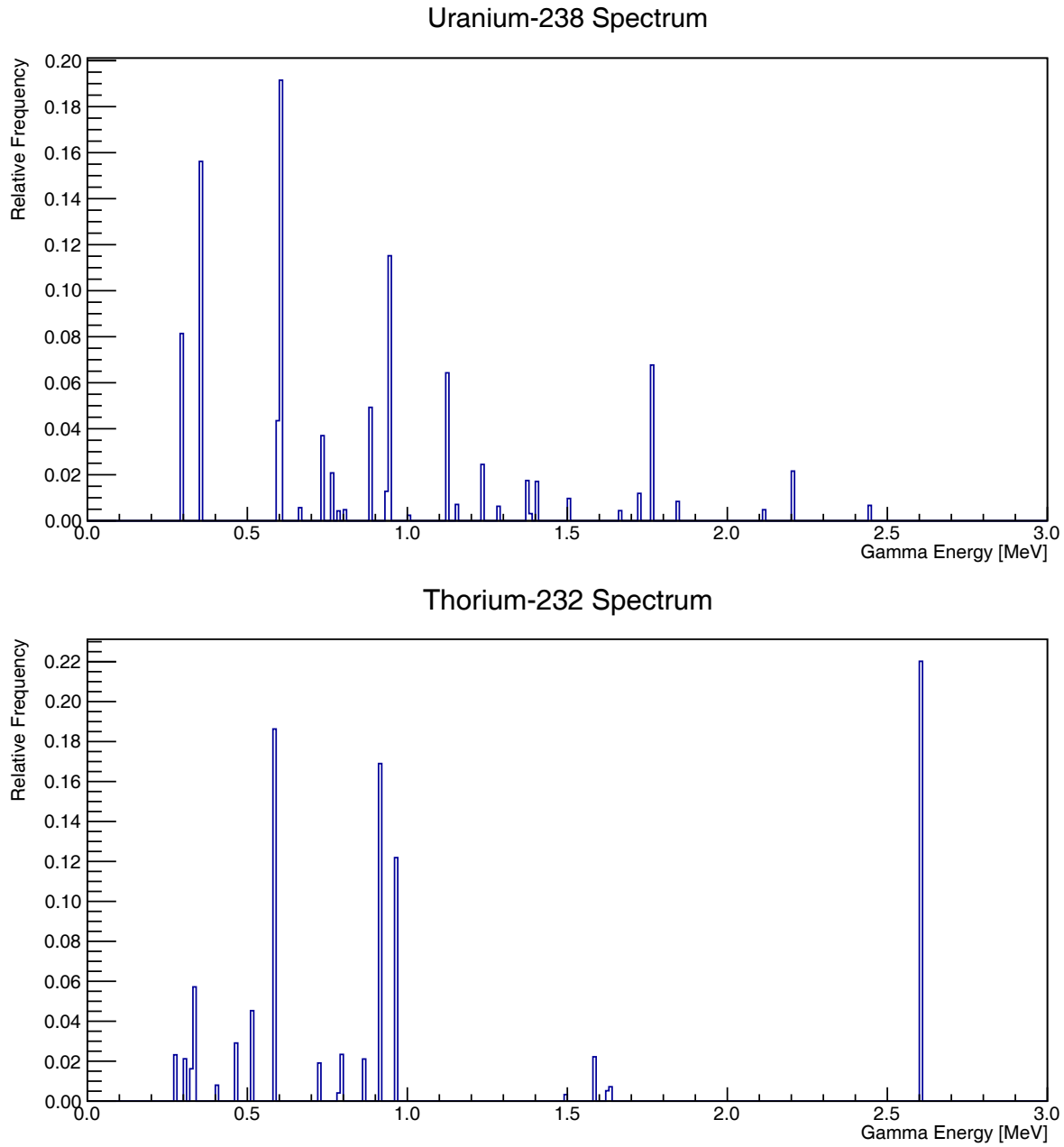

Figure 5.5: The gamma energy spectra from the Uranium and Thorium decay chains. The y-axis shows the relative frequency of this decay from the overall rate versus the gamma energy on the x-axis. [144]

truth information of their interaction with the surrounding materials in terms of x, y and z coordinates as well as the deposited energy in `root` data files. This information is then used for offline analysis. At this point, the simulation considers scintillation, the Cherenkov effect, the photoelectric effect, gamma conversion, absorption, Compton-, Rayleigh- and Mie-scattering as well as reflection and refraction on optical surfaces as physics processes affecting gammas and optical photons. Furthermore, multi-scattering, ionization, Bremsstrahlung, annihilation and pair production are activated for leptons. These processes are called whenever applicable for the respective propagating particle.

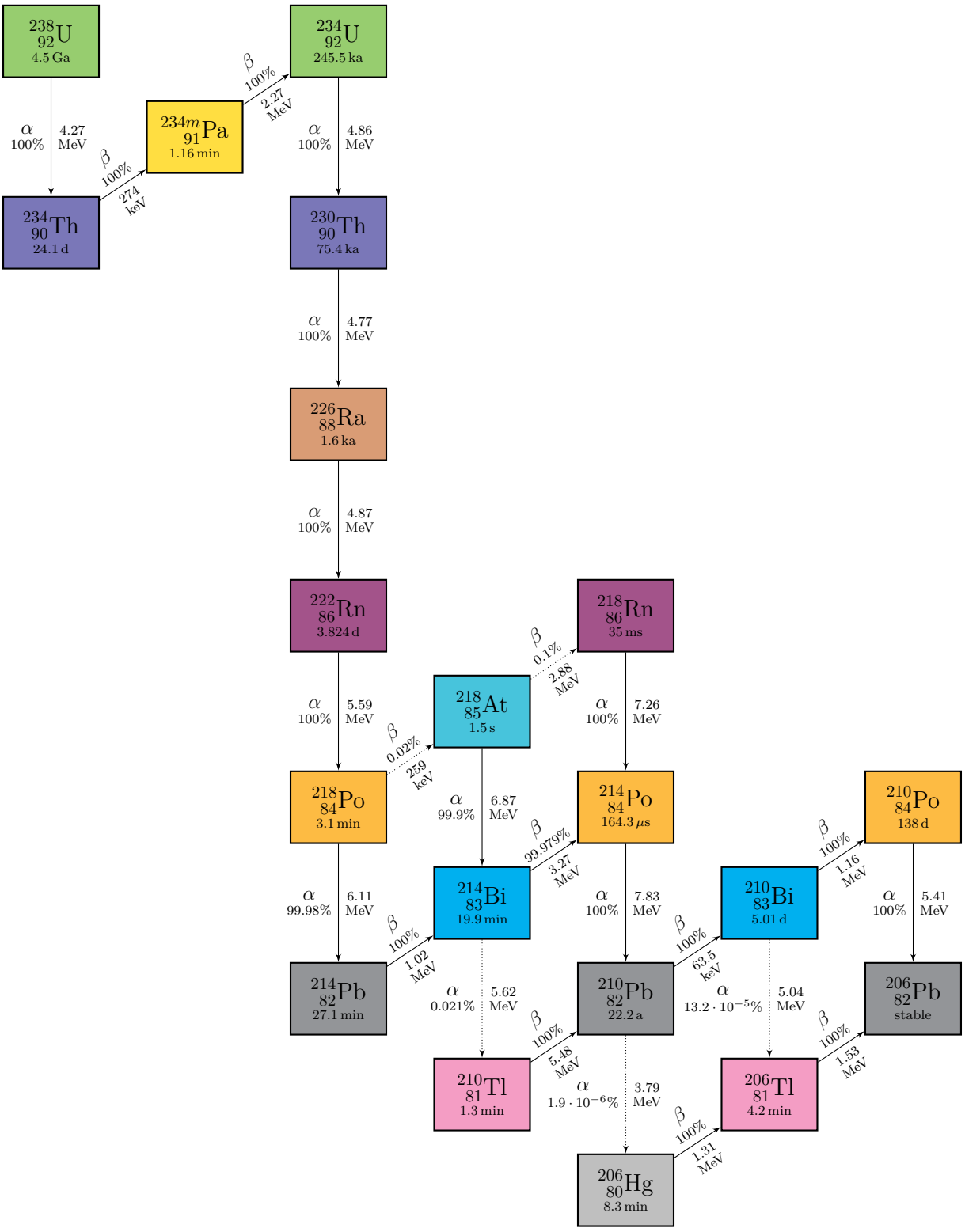

Figure 5.6: Uranium decay chain [145]

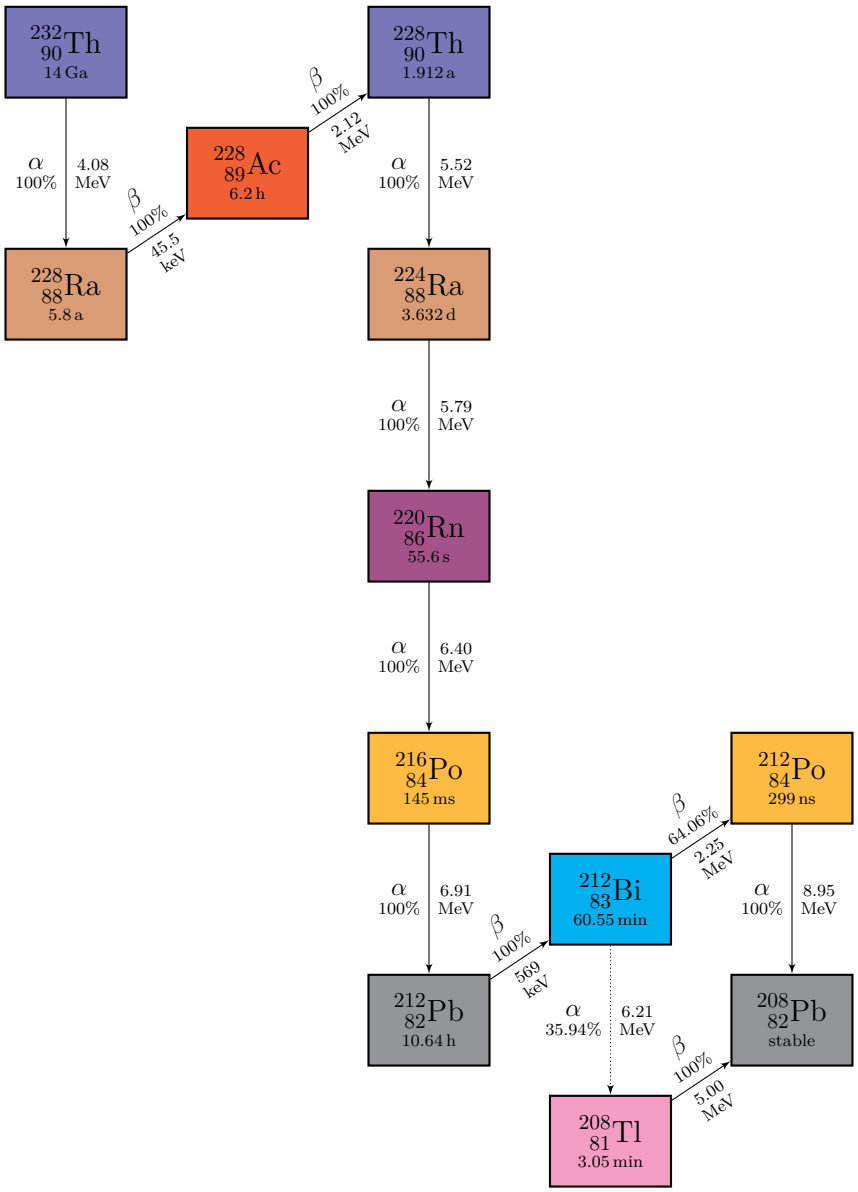

Figure 5.7: Thorium decay chain [145]

In this version of the OSIRIS detector, the total area covered by the PMTs amounts to 40.5 m^2 compared to a tank surface area of 471.24 m^2 (calculated at the location of the PMTs' equatorial line), resulting in an 8.6% coverage. Factoring in the PMTs' detection efficiency (quantum efficiency QE $\times$ collection efficiency CE) of 35% means that around 3% of the total photon yield $Y_\gamma = 10,000\,\gamma$/MeV would be detected. Taking a conservative estimate of $Y_{\text{p.e.}} = 200$ p.e./MeV, an upper limit for the energy resolution of the detector can be calculated using Poisson statistics:

$$\frac{\Delta E}{E} = \frac{\Delta N}{N} \overset{\text{Poisson}}{=} \frac{1}{\sqrt{N}} = \frac{1}{\sqrt{Y_{\text{p.e.}} \cdot E}} \tag{5.1}$$

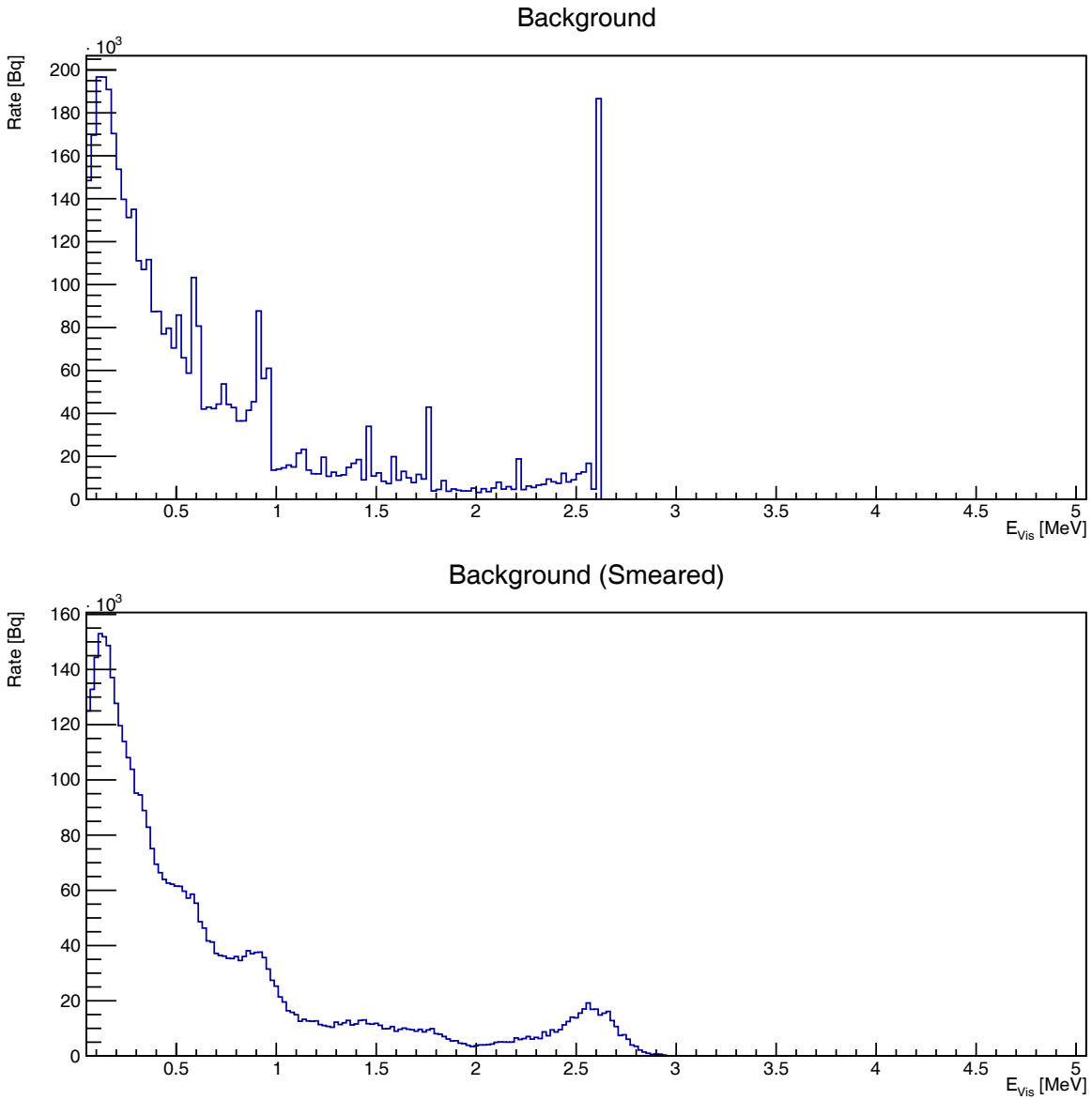

Figure 5.8: External backgrounds in the single tank version of OSIRIS from ^{238}U, ^{232}Th and ^{40}K recorded as Monte Carlo truth (top) and after smearing with an energy resolution of 7% @ 1 MeV (bottom)

The detected energy spectrum recorded from the Monte Carlo truth data was subsequently smeared with this energy resolution (approximately 7% @1 MeV). The resulting effect can be seen in figure 5.8. At this point in the simulation, the "smearing" was performed by a random number generator, which re-assigns a new energy to the event that is within the uncertainty range. A different smearing process would later be implemented that results in smoother curves and does not rely on RNG, as described in section 5.5.

5.3.3 Drainable Tube Design

The next iteration of the detector would have featured a drainable acrylic cylinder surrounded by a buffer liquid in an external tank, housing the PMT system. The central volume was equally large as the steel tank, once again to avoid buoyancy forces, although the acrylic vessel then would have needed to be of a certain thickness to withstand the outside pressure whenever the LS would be drained. In addition to the external liquid buffer - either oil or water, which would have depended on the PMT compatibility and the tank size - shielding at the top and bottom of the detector was to be provided by 5" steel slabs. The planned design at this stage in development is shown in figure 5.9.

The idea to simultaneously utilize this volume as a storage-, filling- or overflow-tank in the JUNO filling line was briefly revisited; however, pretty soon the decision was made by the JUNO Central Detector subgroup to have all the tanks in the filling line oriented horizontally instead of vertically, to reduce hydrostatic pressure, in case the LS would expand due to temperature changes. As a consequence, the concept of a dual-purpose tank was dropped entirely.

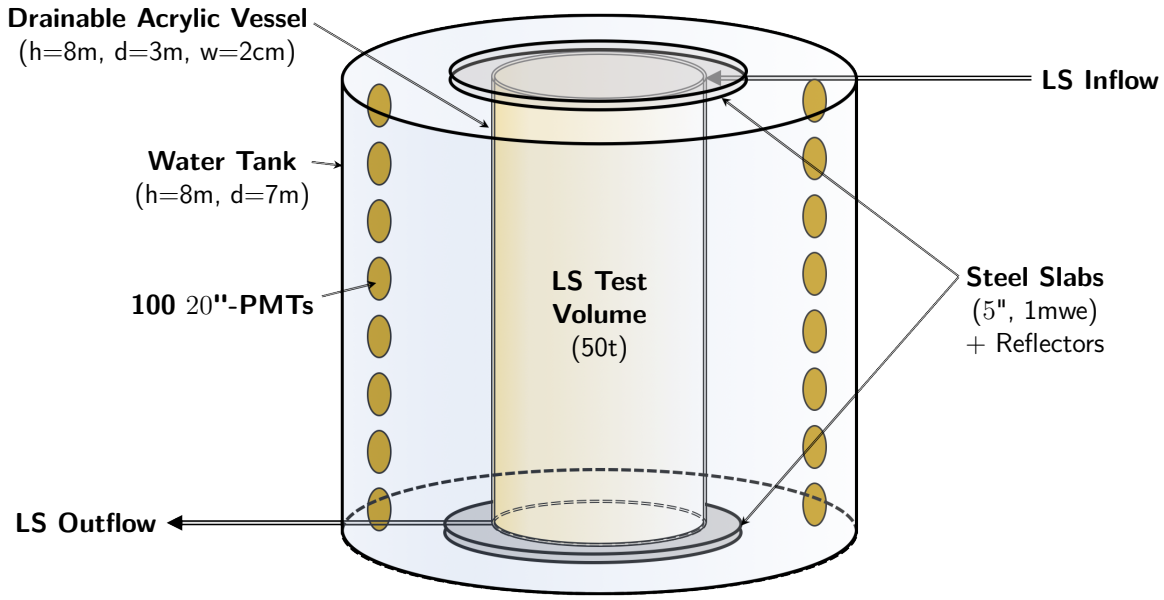

Figure 5.9: An early design concept of the OSIRIS detector. At this stage, the central LS volume was supposed to be fully drainable, while being surrounded by a buffer liquid (either water or oil) and capped off by 5" steel slabs on top and bottom for shielding. A possible variation of the design would have included reflectors on floor and ceiling to improve light collection, but at the cost of position and timing reconstruction. [146]

This reduction of the scintillator volume to an acrylic cylinder within a larger buffer tank forced the next set of major modifications in the simulation: Once again, the outer tank was reduced in size ($\varnothing = h = 8\,\mathrm{m}$) and a new acrylic vessel ($\varnothing = 3\,\mathrm{m}, d = 2\,\mathrm{cm}$) was introduced to extend from top to bottom, filled with LS and surrounded by a buffer liquid to shield from external radioactivity, which in this design was chosen to be water. As a consequence, the PMTs on floor and ceiling have been removed and the total number was also reduced from 200 to 100 units. In order to compensate for the lack of external shielding on top and bottom of the LS volume, 5" steel slabs were added to the tank that are supposed to provide an equivalent amount of shielding from the surrounding rock as 1 m of water would. The cylindrical mantle however stayed at the same thickness ($d = 6\,\mathrm{mm}$) once more, as did the rock volume ($d = 60\,\mathrm{cm}$) and the dimensions of the PMTs themselves. The possibility of adding reflectors at the floor and ceiling was considered in order to compensate for the reduction in light collection efficiency from the reduced amount of PMTs, but was not included in the simulation.

Consequentially, with the new acrylic vessel being in direct contact with the LS, it needed to be considered as an additional source for external backgrounds, so from here on out – just like the rock, steel tank and the PMTs – gammas from ^{40}K, ^{232}Th and ^{238}U were simulated with the acrylic as a source volume as well. Furthermore, at this step in the development of the simulation, cosmogenic backgrounds intrinsic to the scintillator were taken into account as well, although the isotopes in question were not simulated directly, but rather their individual spectra were taken from the radioactivity expectations in JUNO (e.g. [147]) and rescaled according to the purity levels in OSIRIS. While the surrounding material can only contribute gammas with high enough energy to propagate into the active volume, radioactivity within the LS itself also needs to take into account energy depositions from alpha and beta decays which are already included in the various spectra. The individual contributions to the intrinsic background are shown in figure 5.11 and comprise ^{210}Pb, ^{238}U, ^{232}Th, ^{40}K, ^{11}C and ^{208}Tl. Backgrounds from ^{14}C were not included, as its emissions are below the energy threshold of 500 keV imposed on the analysis.

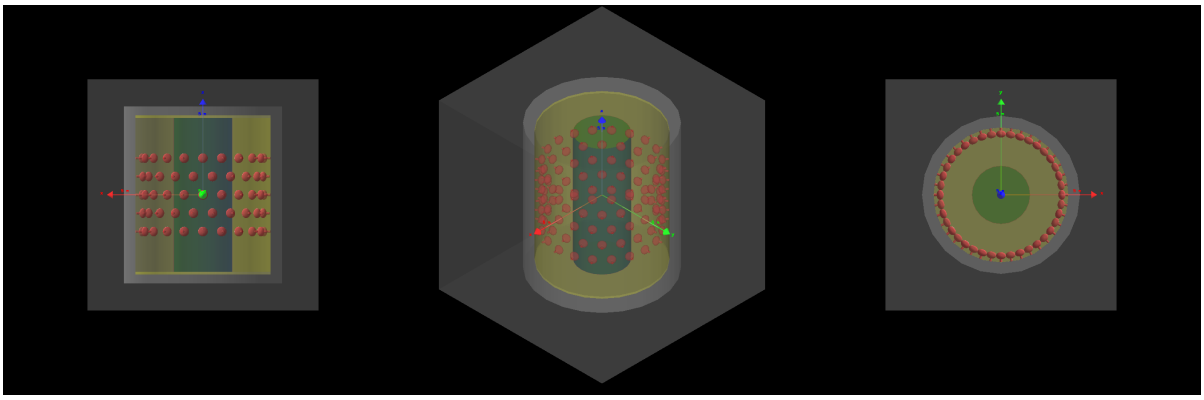

Figure 5.10: The `Geant4` implementation of the drainable tube version of the OSIRIS detector. The center acrylic tube (green) is filled with scintillator while the surrounding buffer (yellow) is made up of water. PMTs are now exclusively distributed along the mantle. The floor and ceiling width of the tank was increased to simulate the 5" steel slabs (left), however no reflectors have yet been added.

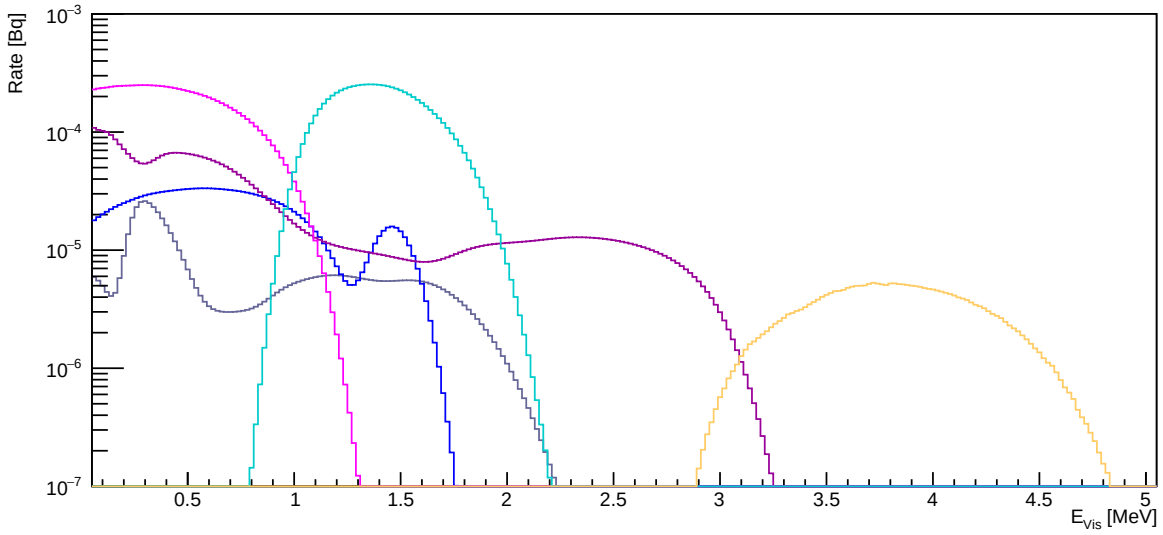

Figure 5.11: Cosmogenic backgrounds intrinsic to the liquid scintillator. The different contributions are ^{210}Pb (pink), ^{238}U (violet), ^{232}Th (gray), ^{40}K (blue), ^{11}C (cyan) and ^{208}Tl (yellow).

5.3.4 Nested Three Tank Model

While the buoyancy-less design persisted for a long time and was the basis for a significant part of the simulation studies, it was ultimately superseded by a three tank nested version, the reasons being that more shielding was required on top and bottom than the steel slabs were able to feasibly provide, while the ultimate transportation and assembly of the OSIRIS detector and its components necessitated a more modular structure. To this end, the overall tank size was shrunk down significantly, to $\varnothing = 5.44\,\mathrm{m}$, $h = 5\,\mathrm{m}$, so that it would fit through the JUNO access tunnels and could be moved by the on-site cranes in one piece. The reduced shielding would be compensated by external tanks in the shape

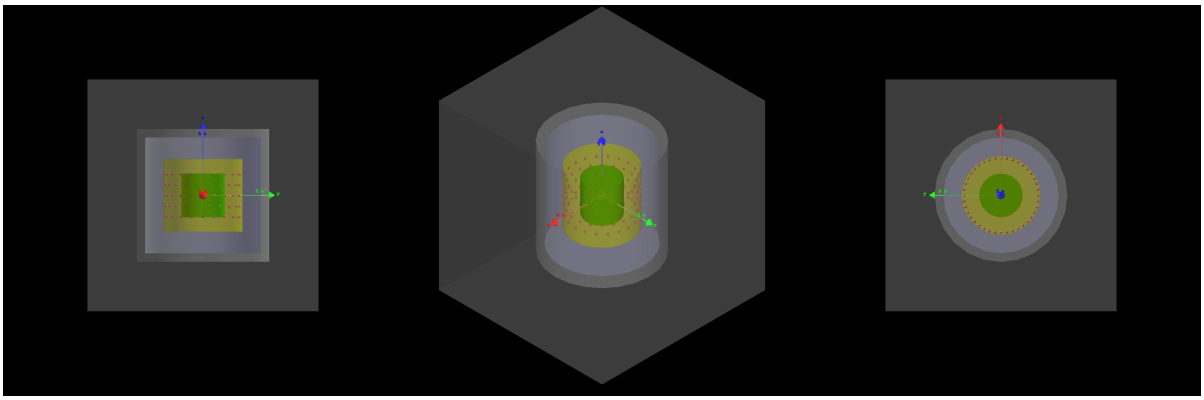

Figure 5.12: The `Geant4` implementation of the nested three-tank version of the OSIRIS detector. The center acrylic vessel (green) is filled with scintillator and is embedded within an oil buffer (yellow) which also houses the PMTs (red). An external water shield (blue) surrounds the entire detector.

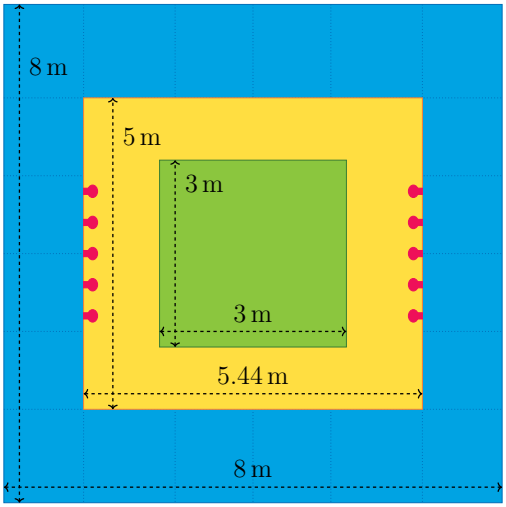

Figure 5.13: A sketch of the modular design version of the OSIRIS detector: A central $3 \times 3\,\mathrm{m}$ acrylic volume filled with LS (green) is surrounded by a $5.44 \times 5\,\mathrm{m}$ oil buffer (yellow) also housing the PMTs (red). The tank itself is encompassed by smaller vessels filled with water (blue) to provide additional shielding.

of cylinder-segments to be placed around, below and above the buffer tank, which itself still houses the PMTs mounted onto its walls, with a $\varnothing = h = 3\,\mathrm{m}$ acrylic vessel filled with LS at the center. A sketch of this version of OSIRIS can be seen in figure 5.13. At this point in development the buffer liquid was set to be oil, as it was considered to re-use the PMTs from the Daya Bay experiment after its disassembly, which are designed to be submerged in a liquid scintillator gamma catcher. This version is also the final one that will be covered in the `Geant4` simulation within this thesis, although the design has further evolved since the official OSIRIS taskforce within JUNO has been assembled. It should be noted that within the simulation (c.f. figure 5.12), the water shielding is treated as a single volume instead of multiple compartments, to improve computation time.

5.4 Detector Simulation

The `Geant4` simulation is based on a stylized representation of the nested three-tank model mentioned in the previous section (c.f. figure 5.12). The cylindrical central volume ($h = \varnothing = 3\,\mathrm{m}$) holds the liquid scintillator (LS) within a thin ($d = 1.8\,\mathrm{cm}$) acrylic vessel. This vessel itself is encapsulated by a steel tank ($d = 5\,\mathrm{cm}$) that holds an organic buffer liquid. 100 inward-facing 8" photomultipliers (PMTs) were attached to the wall of the steel vessel in a honeycomb pattern over five rows. The PMTs themselves were modeled as an ellipsoid ($a = 101\,\mathrm{mm}, b = 68\,\mathrm{mm}$) with a cylindrical base ($r = 42.25\,\mathrm{mm}$) made of vacuum-filled glass ($d = 3\,\mathrm{mm}$). The dimensions of the buffer tank were chosen so that the LS has at least 1 m distance to all sides to any external gamma source, i.e. the PMTs or the steel tank itself. The steel tank is therefore slightly wider than it is high ($h = 5\,\mathrm{m}, \varnothing = 5.44\,\mathrm{m}, d = 5\,\mathrm{cm}$) in order to compensate for the height of the PMTs ($h = 220\,\mathrm{mm}$). The steel tank itself is then submerged in a water volume ($h = \varnothing = 8\,\mathrm{m}$) that serves as external shielding. The detector is encompassed by a rock layer ($d = 60\,\mathrm{cm}$) to all sides to represent the surrounding laboratory at the JUNO underground location.

The material properties (composition, density, refractive index, etc.) assigned to the different components were taken from the official JUNO simulation wherever possible (LS, stainless steel, acrylic) or adapted from the LENA simulation with updates from JUNO (rock, PMT borosilicate glass). However, in some cases both of these inherited their properties directly from `Geant4` (water, vacuum) which was then carried over to the OSIRIS simulation.

When running the simulation, the code distributes various particles at random positions within a chosen volume, propagates them and records the location and amount of any energy deposition within the LS. In the final investigated design of OSIRIS, possible sources of radioactivity are: The scintillator itself, the acrylic vessel, the PMT glass, the steel tank and the surrounding rock bed. The type of particle that was simulated depended on the respective volume.

Within the LS itself, the radioactive isotopes were simulated directly, decaying into daughter particles which then deposit energy in the scintillator material. Note that `Geant4` does not simulate secondary particles in the proper order, so it would not have been possible to later correctly assign which energy deposition is caused by which decay if simulating an entire decay chain consecutively. Therefore, each relevant isotope of a chain was simulated independently. As such, the simulated isotopes within the LS were ^{11}C, ^{10}C, ^{40}K, as well as the members of the Uranium series (^{238}U, ^{234}Pa, ^{234}U, ^{230}Th, ^{226}Ra, ^{222}Rn, ^{218}Po, ^{218}At, ^{218}Rn, ^{214}Pb, ^{214}Bi, ^{214}Po, ^{210}Tl, ^{210}Bi, ^{210}Po, ^{206}Tl) and the Thorium series (^{232}Th, ^{228}Ac, ^{228}Th, ^{224}Ra, ^{220}Rn, ^{216}Po, ^{212}Pb, ^{212}Bi, ^{212}Po, ^{208}Tl). Note that certain nuclides of a series were omitted if their daughter particles carried less than the 500 keV threshold energy.

For the external sources – i.e. rock, steel, PMTs and acrylic – only high-energy gamma particles have the necessary penetration depth to propagate into the active detector volume. (While the acrylic vessel does indeed have direct contact with the LS, alpha and beta particles only travel a few centimeters, which is less than the fiducial volume cut that will be implemented later during the analysis.) Therefore, it was sufficient to only simulate gamma particles, which are monoenergetic for ^{40}K (at 1.46 MeV) or were randomly drawn from the gamma energy distribution spectrum of the Uranium and Thorium chain (c.f. figure 5.5).

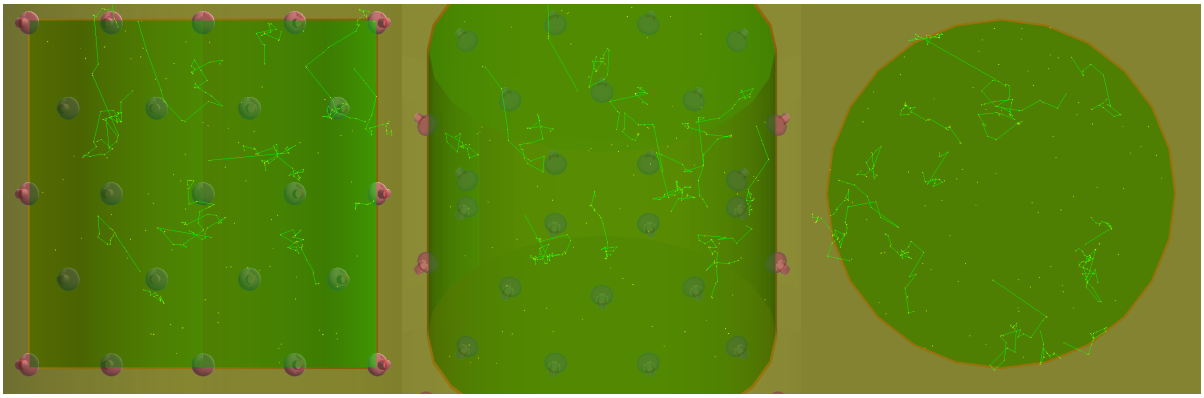

Figure 5.14: 100 ^{40}K decays simulated in the central detector. The probability to produce a 1.46 MeV gamma from electron capture is 10.72% (lines) while the remaining 89.28% cases result in a beta particle instead (dots).

The simulation then creates the respective particle, propagates it along a random trajectory and applies physical processes depending on the type of particle. Optical processes include Cherenkov radiation, scintillation, absorption, Rayleigh scattering, Mie scattering, and boundary processes (an umbrella term within `Geant4` which includes any interaction that happens on the boundary between two or more media, such as reflection, refraction, extinction, etc.) while so-called electromagnetic processes refer to Compton scattering, the photoelectric effect, gamma conversion, ionization of the surrounding material, Bremsstrahlung, pair production and annihilation, etc.

At this point, some nomenclature needs to be established: Every time the simulation is instructed by the user to create primary particles is called a "run" and all particles within one run share the same run ID. Similarly, creating one primary particle within a run constitutes an "event" and both the primary particle and all secondary particles it produces possess the same event ID. Lastly, every single instant that any particle undergoes a physical process is referred to as a "step". For illustration purposes, one run could be the instruction to generate 100 gammas. Each individual gamma would create a new event and every interaction this gamma or any secondary particle it produces would be its own step.

If a simulated particle crosses into the scintillator volume, each loss in particle energy as well as the location of the respective interaction that caused it is saved in a `root` tree on a step-by-step-basis alongside the event ID it belongs to. This allows to create a three-dimensional "map" of the energy depositions from the various particles, which can then be used to calculate the total background rate that the OSIRIS detector will be exposed to. Since only steps within the LS are recorded and not all events reach the central detector because of the strong shielding, a sufficiently high number of events must be simulated to provide enough statistics for the analysis. It has turned out that roughly 10^8 events per background type (Uranium, Thorium, Potassium) from the external rock volume and 10^6 events from all other volumes and backgrounds produce a sufficient amount of interactions ($\mathcal{O}(10^3)$) within the LS. Additionally, the code also saves the random number generator seed that was used to create the simulation data (which was chosen to be the UNIX time, to guarantee a different seed for each run) as well as the weight mass of every possible background source, as provided by `Geant4` itself.

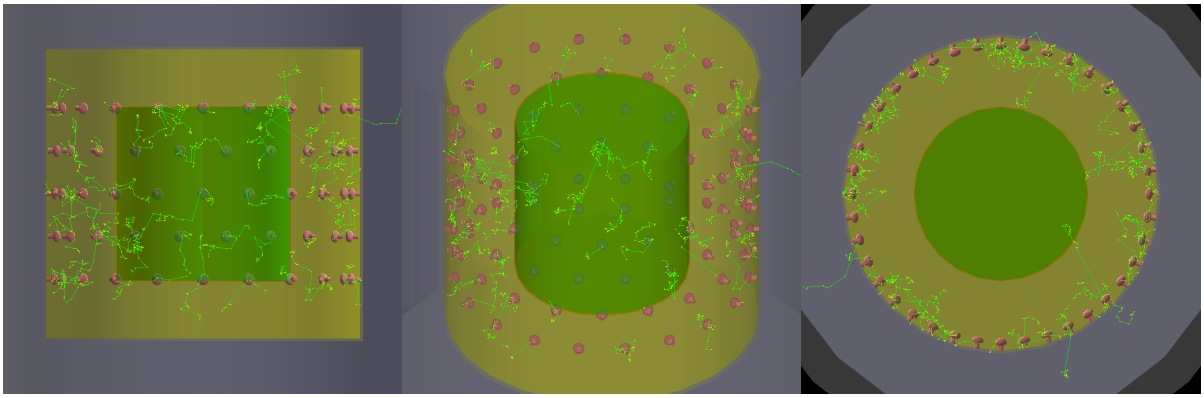

Figure 5.15: 100 1.46 MeV gammas from ^{40}K created in the PMT glass, then propagating into the central detector. Most are stopped within the buffer liquid, but some propagate into the LS volume.

5.5 Data Processing

The analysis determines the sensitivity of the OSIRIS detector by calculating how large the signal rate of Bi-Po-coincidences from a contamination must be in order to exceed the external background rate provided by the simulation data. The code therefore requires a combined background spectrum of all individual contributions.

The first step towards obtaining this spectrum is to merge the energy losses of all individually recorded steps based on the particle event that created them. The x, y and z coordinates of the individual steps are added by weight of the energy deposition in order to obtain an average location of where the detector would place this event. This is called a "barycenter". Their spatial distribution in the LS can be seen in figure 5.16.

$$x_{\text{Bary}} = \frac{\sum_i x_i \cdot E_i}{\sum_i E_i} \tag{5.2}$$

After barycenter calculations of the recorded events a fiducial volume cut is applied, which over several iterations has been chosen at 50 cm as the best value to remove as much of the background as possible while simultaneously keeping a high signal rate in the remaining volume. Only events with a barycenter position at least 50 cm away from all acrylic walls will be considered for the analysis. The remaining events are smeared with the detector's energy resolution, which can be calculated via Poisson statistics from the number of detected photoelectrons per energy deposition according to equation (5.1). As the PMTs cover roughly 2.7% of the tank's surface area and possess a photon detection efficiency of 35% (c.f. section 2.1), only 0.95% of all light will be detected. With an absolute light yield of $Y_\gamma = 10,000\,\gamma/\text{MeV}$, this results in a photoelectron yield of $Y_{\text{p.e.}} = 95\,\text{p.e./MeV}$. The total energy resolution is therefore:

$$\Delta E = \sqrt{\frac{E}{Y_{\text{p.e.}}}} \simeq 10.25\%\ @1\,\text{MeV} \tag{5.3}$$

Instead of filling all events directly into a histogram, each one is replaced by a Gaussian bell curve with a width corresponding to the uncertainty at the event's respective energy, normalized in such a way that the integral does not change. The histograms are then divided by the number of initially simulated events, so they can then be treated as probability density functions. The integral over a certain interval will then yield the probability of detecting background radiation in this energy range. Note that especially for external backgrounds, the total integral is most likely less than 100%, as not all primary particles reach the central detector or the fiducial volume (c.f. figure 5.15).

So far, all the different backgrounds have been treated separately, but in order to estimate the total event rate, they need to be added together, while respecting the specific activity of all the isotopes within each material. Values for the individual material impurities were sometimes obtained from JUNO-internal presentations but mostly the internal JUNO Material Radioactivity Database that collects the measured results from various samples of materials that are intended for usage in the JUNO detector. The relevant quantities are the ^{238}U, ^{232}Th and ^{40}K rates in the rock from the JUNO site, borosilicate from Hamamatsu PMTs, stainless steel and acrylic. The values in question are displayed in table 5.3. For the intrinsic backgrounds within the LS, the baseline JUNO solar neutrino requirements from table 5.1 were assumed to be the de facto activities, as any excess rate should be treated as an unwanted contamination by OSIRIS.

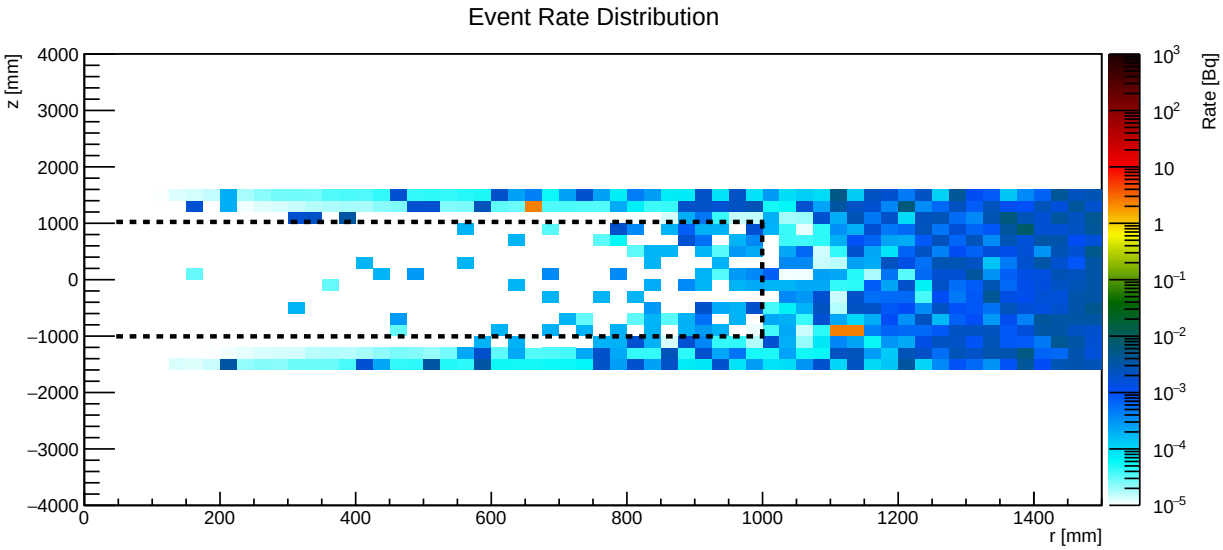

Figure 5.16: The spatial distribution of events within the LS, weighted by rate. In order to reduce the total background for the analysis, a 50 cm fiducial volume cut (dashed line) will be implemented.

For the intrinsic backgrounds within the LS, the values given in table 5.1 need to be converted to Bq/kg. For ^{11}C and ^{10}C, this is straightforward, as cts/d/kt only needs a scaling factor of $1.1574 \cdot 10^{-11}$. The remaining contributions, however, have to be individually adjusted using their respective specific activity, which is given by:

$$a = \frac{N_\mathrm{A} \cdot \ln 2}{T_{1/2} \cdot M} \tag{5.4}$$

where N_A is Avogadro's constant, $T_{1/2}$ is the half-life and M the molar mass of the nuclide in question. The resulting activities are shown in table 5.2.

The various probability distribution histograms then need to be multiplied with their respective activities per mass unit and the mass of the source volume (LS, acrylic, PMT, steel, rock). Furthermore, the values given only refer to the eponymous parent nuclide of a series, the rate must therefore be converted to the entire decay chain. For the intrinsic backgrounds, every isotope has been simulated individually, so it is sufficient to apply the same activity value to all daughters of a chain, assuming secular equilibrium. For the

Intrinsic Backgrounds Activity	
Isotope	Bq/kg
^{238}U	$1.24 \cdot 10^{-9}$
^{232}Th	$4.06 \cdot 10^{-10}$
^{40}K	$2.64 \cdot 10^{-9}$
^{11}C	$2.15 \cdot 10^{-8}$
^{10}C	$4.05 \cdot 10^{-10}$

Table 5.2: The baseline solar requirements from table 5.1 converted to Bq/kg for use in the OSIRIS analysis.

External Backgrounds Activity			
Bq/kg	^{238}U	^{232}Th	^{40}K
PMT	3.76	3.71	8.96
Rock	142	123	220
Steel	$1.2{\cdot}10^{-3}$	$8{\cdot}10^{-3}$	$13.4{\cdot}10^{-3}$
Acrylic	$12{\cdot}10^{-6}$	$4{\cdot}10^{-6}$	$270{\cdot}10^{-6}$

Table 5.3: External background activity per mass unit for the ^{238}U, ^{232}Th and ^{40}K backgrounds within the detector materials, given in Bq/kg. Values taken from JUNO-internal presentations or the JUNO Material Radioactivity Database.

external backgrounds, only high-energy gammas have been simulated, randomly drawn from the spectra shown in figure 5.5. The activity must therefore be multiplied with the total number of contributing isotopes in each series, once again assuming secular equilibrium. This number is 3 for ^{238}U (^{234}Pa, ^{214}Pb and ^{214}Bi) while it is 4 for ^{232}Th (^{228}Ac, ^{212}Pb, ^{212}Bi and ^{208}Tl).[144] Once appropriately scaled, the histograms' integrals directly correspond to the event rate and they can be simply added to obtain the combined spectrum. The result can be seen in figure 5.17 for the full LS volume and in figure 5.18 after the fiducial volume cut. Single event rate values for both are listed in table 5.4.

Closer inspection of the individual contributions reveals that the background is dominated by the external sources, with the biggest contributions from the rock around 2–3 MeV as well as the steel tank and the PMTs for lower energies. After a 50 cm fiducial volume cut, the intrinsic backgrounds scale by 1/3rd like the remaining LS volume while the external ones have been reduced by a factor 10 or more, depending on source and energy range. The contribution by the rock has been basically eliminated and the PMTs dominate the spectrum, with a similar contribution by the steel tank at higher energies.

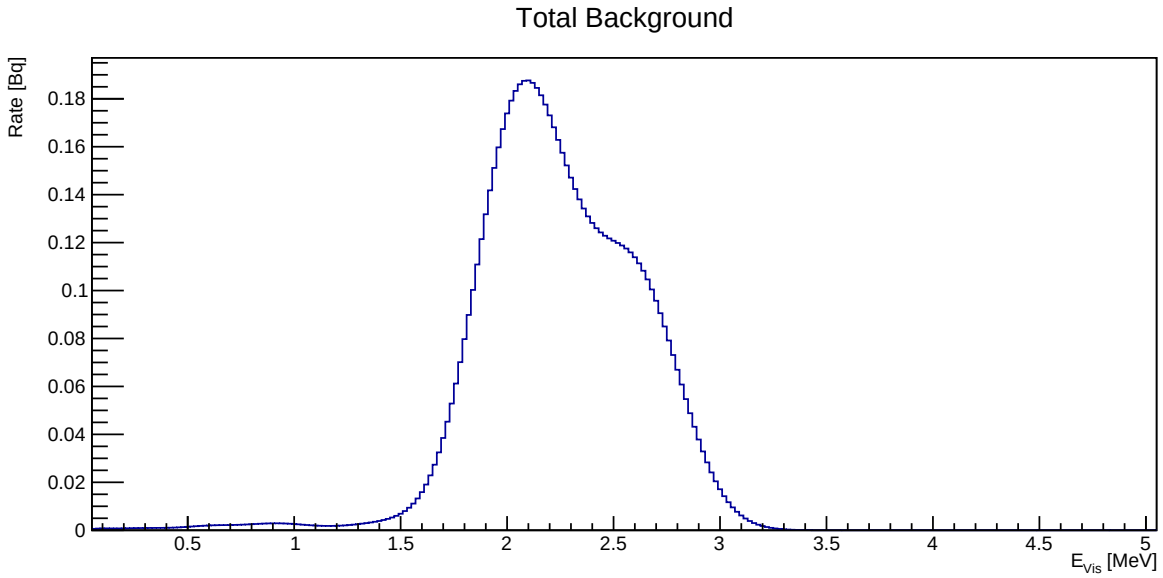

Figure 5.17: The radioactive background spectrum for the full detector, dominated by external sources. The biggest contributions are rock at higher and steel tank / PMTs at lower energies.

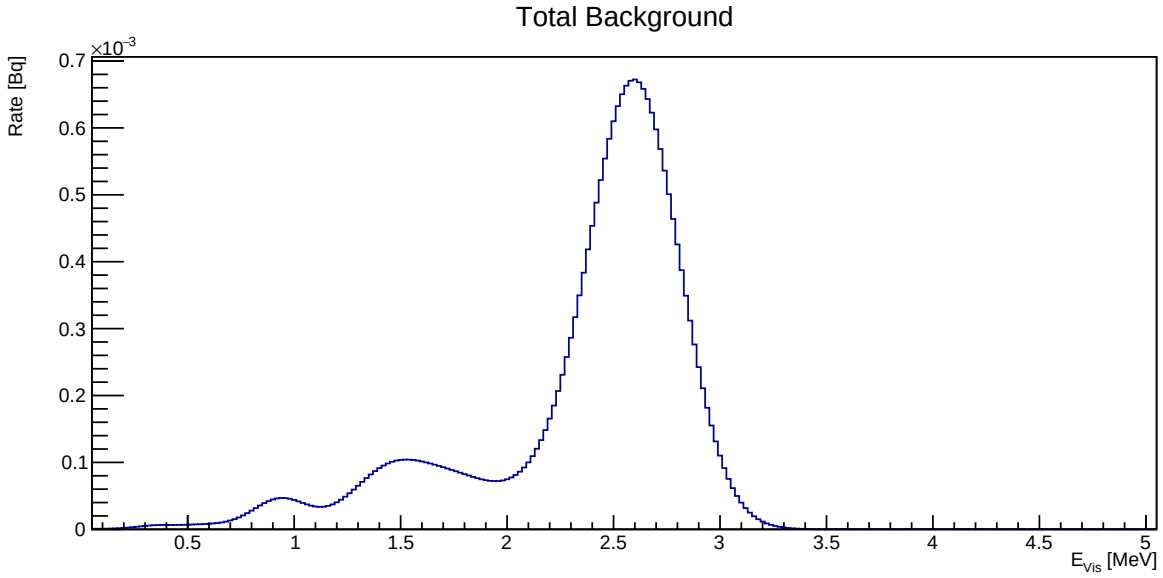

Figure 5.18: The radioactive background spectrum for the fiducial volume, dominated by external sources. The biggest contributions are the PMTs at lower and steel tank / PMTs at higher energies.

Singles Rate Full Volume			
mBq	Po-range	Bi-range	Total
PMT	6.74	97.5	195.8
Rock	0	5866	7327
Steel	5.39	221.2	296.6
Acrylic	2.26	1.62	36.99
LS	0.048	0.042	0.473
$\sum$	14.47	6185	7855

Singles Rate Fiducial Volume			
mBq	Po-range	Bi-range	Total
PMT	0.11	9.93	12.87
Rock	0	0	0
Steel	0.00002	8.88	9.63
Acrylic	0.020	0.079	0.562
LS	0.015	0.014	0.140
$\sum$	0.138	18.91	23.19

Table 5.4: Rate of single events within the full LS vessel and in the fiducial volume in mBq, split by background sources. The column titles refer to the intervals $[1.98; 5]$ MeV (Bi-range) and $[0.72; 0.82]$ MeV (Po-range) as defined in section 5.6 with the last column showing the total rate across all energies.

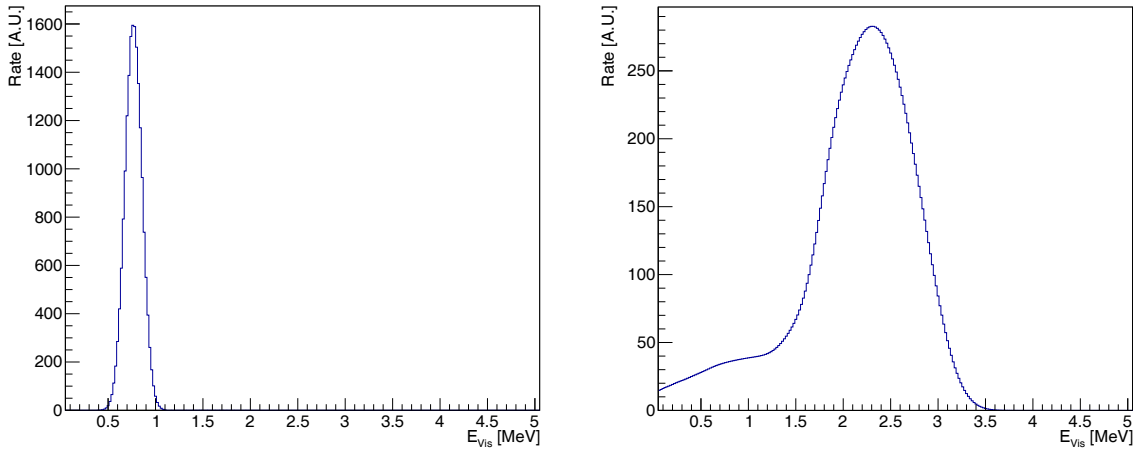

Figure 5.19: Right: The energy spectrum from the beta decay of ^{214}Bi ($p = 99.979\%$). Left: The energy spectrum from the alpha decay of ^{214}Po, after quenching by roughly 1/10th within LS. Both spectra were smeared with the energy resolution of 10.25% @1 MeV

5.6 Sensitivity Evaluation

The sensitivity of the OSIRIS detector can be evaluated by means of a rate comparison: The simulation provides an expected value of the rate caused by external backgrounds and intrinsic radiation within the liquid scintillator (LS) in an amount that is still deemed acceptable. If the LS contamination exceeds this accepted rate, more events would be detected in the same time. In particular, the events that are under investigation are Bi-Po-coincidences: That is an event with an energy in the range around the Q-value of ^{214}Bi's beta decay (3.27 MeV with a branching ratio of 99.979%, c.f. figure 5.6) directly followed by a signal in the energy range of ^{214}Po's subsequent alpha decay. The energy ranges in question were chosen according to the decay spectra of the two nuclides, as shown in figure 5.19, to be $[1.98; 5]$ MeV for the Bi-range and $[0.72; 0.82]$ MeV for the Po-range. Note that the decay energy of ^{214}Po is actually 7.83 MeV, but alpha particles are quenched by roughly a factor of 1/10th in liquid scintillators so that the visible energy is reduced to 0.77 MeV. The coincidence window that gives the maximum time the two signals are allowed to be separated was chosen as $\Delta t = 710\,\mu$s, which is three times the lifetime of the alpha decay, $\tau(^{214}\text{Po}) = 236.6\,\mu$s.

The number of false coincidences that are caused by accidental background events with similar energies and time distribution can then be calculated as:

$$N_{\text{BG}} = R_{\text{BG}}(\text{Bi-Range}) \cdot \Delta t \cdot R_{\text{BG}}(\text{Po-Range}) \cdot T \tag{5.5}$$

where R_{BG} denotes the rate of single backgrounds obtained by integrating the rate distributions shown in figures 5.17 and 5.18 over the respective energy ranges and T is the total time over which the LS is measured within OSIRIS.

Similarly, the number of real Bi-Po-coincidences within OSIRIS is given by:

$$N_{\text{BiPo}} = R_{\text{Bi}} \cdot \left\{1 - \exp\left(-\frac{\Delta t}{\tau(^{214}\text{Po})}\right)\right\} \cdot \epsilon_{\text{Bi}} \cdot \epsilon_{\text{Po}} \tag{5.6}$$

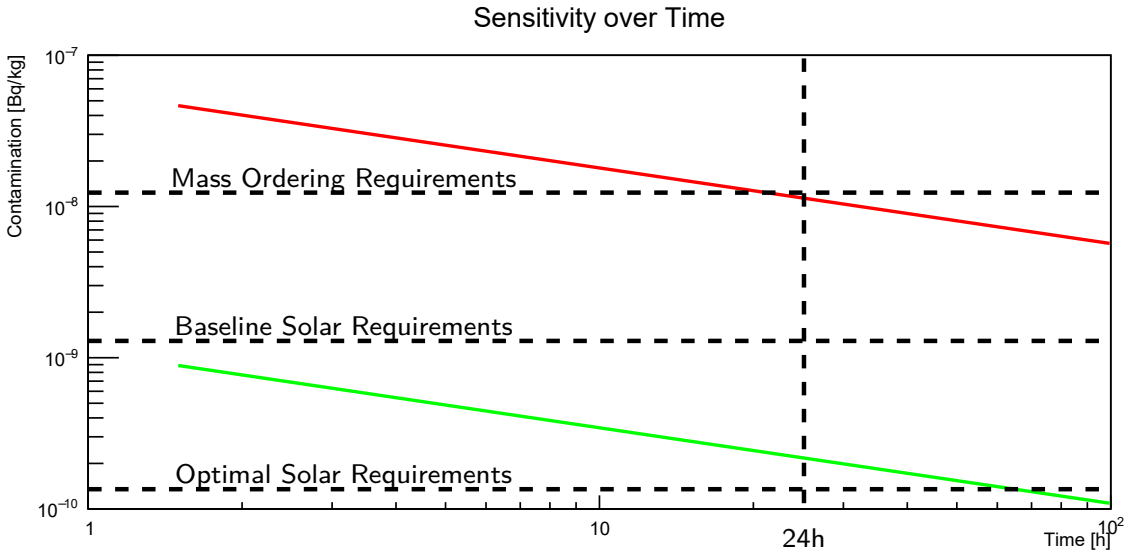

Figure 5.20: The Bi-Po-coincidence rate that the OSIRIS detector is sensitive to as a function of the total measurement time T for the full detector (red) and when using a 50 cm fiducial volume cut (green). After 24 hours, the detector reaches a sensitivity of $1.16 \cdot 10^{-8}$ Bq/kg for the full and $2.22 \cdot 10^{-10}$ Bq/kg for the fiducial volume.

with R_{Bi} the actual rate of ^{214}Bi decays as well as $\epsilon_{\mathrm{Bi}} = 67.85\%$ and $\epsilon_{\mathrm{Po}} = 49.38\%$ the selection efficiency of the respective energy ranges compared to the total (smeared) decay spectra.

It was decided that to distinguish real events from background fluctuations, the signal rate needs to exceed the background level with at least two standard deviations, which – assuming Poisson statistics – translates to:

$$N_{\mathrm{BiPo}} \gtrsim 2 \cdot \sqrt{N_{\mathrm{BG}}}. \tag{5.7}$$

Inserting equations (5.5) and (5.6) into equation 5.7 and solving for R_{Bi}, the rate limit to which OSIRIS is sensitive to can be calculated as a function of the total measurement time T by:

$$R_{Bi} \gtrsim \frac{2 \cdot \sqrt{R_{BG}(\mathrm{Bi}) \cdot \Delta t \cdot R_{BG}(\mathrm{Po})}}{\left\{1 - \exp\left(-\frac{\Delta t}{\tau(\mathrm{Po})}\right)\right\} \cdot \epsilon_{Bi} \cdot \epsilon_{Po}} \cdot \frac{1}{\sqrt{T}}. \tag{5.8}$$

The resulting sensitivity to the ^{214}Bi/^{214}Po-coincidence decays as a function of the measurement time T is displayed in figure 5.20. As OSIRIS' goal is to measure each batch for approximately one day, the respective values for 24 hours are $1.16 \cdot 10^{-8}$ Bq/kg for the full detector volume and $2.22 \cdot 10^{-10}$ Bq/kg after applying a 50 cm fiducial volume cut. For comparison, the Counting Test Facility (CTF) at the Laboratori Nazionali del Gran Sasso (LNGS) in Italy, described in section 5.2, reached sensitivities on the level of $\mathcal{O}(10^{-9}\,\mathrm{Bq/kg})$ using a similar sized detector.[138] Translating these values into concentrations shows that the OSIRIS detector is sensitive to contaminations up to $9.4 \cdot 10^{-16}$ g/g when using the full detector and $1.8 \cdot 10^{-17}$ g/g with the fiducial volume. OSIRIS thus

not only surpasses the sensitivity of the CTF but also manages to reach the sensitivity requirements of the JUNO limits for solar neutrino studies, exceeding them in their baseline purity (10^{-16} g/g) and comes close to their optimal values, which is one order of magnitude more stringent (10^{-17} g/g, c.f. tables 5.1 and 5.2).

Chapter 6

Conclusions & Outlook

This thesis aims to assist in improving the liquid scintillator (LS) purity for the Jiangmen Underground Neutrino Experiment (JUNO), both in terms of optical transparency as well as radioactive contamination. At the core of JUNO lies a $\varnothing = 35.4\,\mathrm{m}$ large acrylic sphere containing 20 kt of LS, submerged in a $\varnothing = 43.5\,\mathrm{m}$ cylindrical tank filled with roughly the same amount of water as external shielding. The LS not only serves as a target material for neutrino interactions but also as a means of detection, producing luminescent light after each weak nuclear interaction. JUNO's primary goal is the determination of the neutrino mass ordering, for which it requires a high energy resolution of $3\%/\sqrt{E[\mathrm{MeV}]}$. This can only be achieved by adhering to stringent constraints on cleanliness for the detector materials, in particular the LS itself: A high optical purity allows for unobstructed transport of the scintillation photons to the light-sensitive photomultiplier tubes (PMTs) surrounding the central vessel, enabling an efficient light collection, paramount for the energy resolution. At the same time, strict radiopurity limits guarantee a low background event rate, thus avoiding false signals, which is especially relevant for more elusive types of events, such as solar neutrinos. The present work addresses both of these topics in terms of hard- and software, utilizing laboratory experiments, computer simulation and data analysis.

The first part of the thesis focuses on optical purity, specifically the determination of LS scattering parameters. The relevant quantities in this case are characteristic lengths that reveal after what distance travelled within a medium a light beam's intensity has declined to $1/e$ of its initial value: With the previously mentioned detector dimensions, the JUNO scintillator aims for an attenuation length of $\Lambda_{\mathrm{Att}} \geq 20\,\mathrm{m}$ at 430 nm. This can be achieved, for example, by reaching an absorption length of $\Lambda_{\mathrm{Abs}} \geq 60\,\mathrm{m}$ and a scattering length $\Lambda_{\mathrm{Scat}} \geq 30\,\mathrm{m}$. A dedicated laboratory experiment was designed and constructed in order to investigate the Rayleigh scattering behaviour – the dominant scattering process inside JUNO – of LS at the lower end of the visible light spectrum. The setup determines the Rayleigh length by comparing the horizontally and vertically polarized components of light scattered at 90° within a sample to the throughgoing intensity. A monochromator allows for wavelength-dependent measurements and PMTs operating in single photon counting mode are used as light sensors. An extensive calibration campaign of all individual components and the system as a whole was conducted and the experiment was tested with organic and inorganic liquids, reproducing the known Rayleigh scattering lengths of the involved samples, to guarantee the reliability of the results.

Afterwards, two LS samples with unknown scattering lengths were investigated: One sample of commercial Linear Alkyl Benzene (LAB) from Nanjing, China, and another scintillator sample of LAB from the chemical company SASOL, which had previously been used for the SHiP experiment. Both samples were measured at 400 nm, 415 nm, 430 nm, 450 nm and 470 nm and generally showed similar behaviour: The Rayleigh scattering lengths followed the expected λ^4-dependency for higher wavelengths but experienced a decline from the expectation when approaching the lower end of the investigated spectrum. In order to exclude a possible error stemming from the experiment itself, both samples were cross-checked for transparency using a UV/Vis-spectrometer. The hereby obtained attenuation length results confirmed different behaviours in the two wavelength regions for both samples, and thus the scattering lengths are accepted to be correct. Therefore, the Nanjing commerical LAB yields a value of $(26.1 \pm 1.2_{\text{stat}} \pm 2.6_{\text{sys}})$ m while the SASOL sample shows a Rayleigh length of $(22.4 \pm 0.7_{\text{stat}} \pm 2.2_{\text{sys}})$ m at 430 nm, both of which lie in the range expected for pure LAB and agree with similar measurements performed by other groups.

While the setup performed admirably, there is still ample room for improvement. Currently, the software saves all detected pulses directly to a hard drive, in preparation for offline analysis. Although this was a prudent approach as long as the reliability of the results was constantly under investigation, it is also an excruciatingly slow process due to the speed of data transfer and the huge number of pulses needed for good statistics. Since the experiment has now been verified as trustworthy, the setup could be modified to directly count the pulses during live operation using a constant fraction discriminator. Additional PMTs could be added at angles other than 90°, which would allow to incorporate angular information into the Rayleigh scattering analysis. Lastly, the currently implemented continuous lamp might be replaced by a pulsed light source to obtain timing information on the scattering processes.

The second part of the thesis deals with radioactive contaminants inside the LS. In order for JUNO to achieve its main goal – the determination of the neutrino mass ordering – the LS has stringent requirements for radiopurity, in particular a concentration of less than $1 \cdot 10^{-15}$ g/g for isotopes from the ^{238}U and ^{232}Th decay chains. If JUNO intends to analyse solar neutrinos as well, the purity needs to be at least one order of magnitude better, preferably two. To assist in arriving at these target values, a pre-detector was envisioned that is meant to be placed in the JUNO liquid filling line and measure the LS with regards to radiopurity before it reaches the acrylic vessel. Not only would such a detector determine the exact concentration of contaminants within the scintillator, but it could act as a failsafe measure that issues a warning if a too high threshold is surpassed, allowing to stop the filling and further purify the LS so as not to pollute the central detector.

Towards this goal, a Monte Carlo simulation was written in `Geant4` in order to investigate the feasibility of such a device. Various layouts that differ in components and dimensions were investigated over the course of the study, before arriving at the final design: The Online Scintillator Internal Radioactivity Investigation System (OSIRIS) consists of nested concentric cylinders, with a $\varnothing = h = 3$ m LS volume at the very core, submerged within a $\varnothing \simeq h = 5$ m buffer tank housing an array of 100 8" PMTs detecting light emissions from radioactive decays. This tank in turn is surrounded by an $\varnothing = h = 8$ m external water shielding.

OSIRIS determines the concentration of radioactive nuclides in the LS based on a rate analysis of Bi $\rightarrow$ Po $\rightarrow$ Pb decays. These transitions produce distinct energy signals and have a short coincidence time, so they can be easily identified. The OSIRIS simulation provides a prediction of single event rates and their energies that reach the pre-detector's LS volume. Estimating the expected accidental coincidences from these single rates allows to calculate the lowest contamination that can still be identified against the background. In the scope of this thesis, the Uranium chain was investigated specifically, which includes the ^{214}Bi $\rightarrow$ ^{214}Po coincidence. Considering the expected activities from OSIRIS detector materials and the surrounding rock bed at the JUNO site, a sensitivity of $1.16 \cdot 10^{-8}$ Bq/kg can be reached, which translates to a concentration of $9.4 \cdot 10^{-16}$ g/g for nuclides from the Uranium chain. While this is below the requirements for the mass ordering determination, it is not sufficient for a solar neutrino analysis. Therefore, a 50 cm fiducial volume cut was implemented in order to further suppress background rates, leading to a new sensitivity of $2.22 \cdot 10^{-10}$ Bq/kg or $1.8 \cdot 10^{-17}$ g/g, which exceeds the baseline requirements for the JUNO solar neutrino program and barely falls short of the optimal concentration. Still, based on these analyses, the OSIRIS detector is considered to have reached its goals and passed the feasibility study.

This positive sentiment was shared by the JUNO collaboration who have since created a dedicated OSIRIS task force whose goal is realising the construction of the detector. The simulation has evolved significantly since the feasibility study conducted for this thesis, implementing additional features such as active detector volumes, photon propagation and position smearing. The coincidence search has been extended to include ^{212}Bi $\rightarrow$ ^{212}Po events from the Thorium chain as well. Finally, the simulation's Monte Carlo truth output is used as a basis to create reconstruction algorithms for the actual OSIRIS detector data, once in operation.

Similarly, the design of the detector itself has evolved, although the general layout from this thesis remains. While the $\varnothing = h = 3\,\mathrm{m}$ central acrylic vessel for the LS still persists, the buffer and veto volume merged into one one $\varnothing = h = 9\,\mathrm{m}$ water tank. Although no longer modular, the tank can now be delivered in parts and assembled on site. Since it will be made of carbon steel and bolted instead of welded, a high-density polyethylene (HDPE) liner is required to separate the water from the tank walls. 68 inward-facing 20" PMTs will be mounted onto a stainless steel scaffolding at 2.5 m distance to the center, with 12 PMTs of the same size on floor and ceiling of the tank to serve as an active muon veto array. The PMT array is outfitted with on-board electronics that allow self-triggering, on-the-fly gain selection over three ranges and direct signal digitization on the base, which gave them the term "intelligent PMTs" or iPMTs for short. [148]

The filling and drainage pipes at the top and bottom of the acrylic vessel now end in diffuser systems that improve the homogeneous distribution of freshly filled LS. This is meant to facilitate a possible continuous measurement mode, wherein new LS will arrive at a higher temperature and then cool down over the course of the measurement which leads to temperature and thus density layers within the detector, so that the oldest LS will always sit at the bottom, ready to be drained off. Each individual layer will still spend the same amount of time within OSIRIS to be investigated, but this eliminates waiting time during dedicated filling and draining phases. It also allows to pick samples more frequently from the purification systems as only a fraction of the total detector volume is replaced each time. [149]

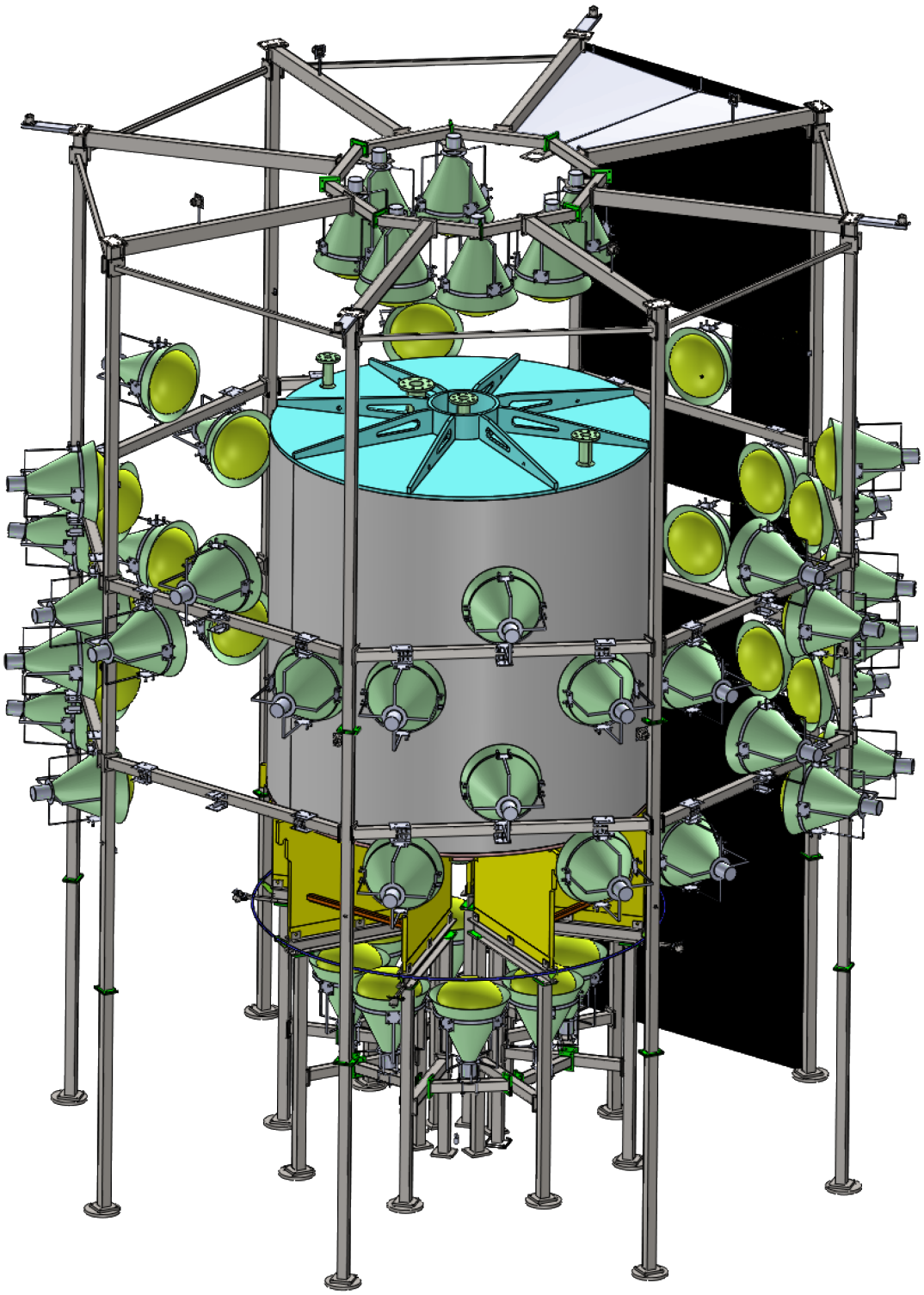

Figure 6.1: The latest version of the OSIRIS radioactivity monitor, at the time of this writing. A 3×3 m acrylic vessel filled with 19 t of LS is surrounded by a steel scaffolding at 2.5 m distance to the center of the detector to which an optical separation between inner detector and external veto is attached. 68 inward-facing 20" iPMTs are mounted onto the scaffolding, measuring the radioactive contamination of the LS by detecting scintillation light from radioactive decays. Not depicted is the 9×9 m carbon steel tank providing 330 t of water shielding and the 12 outward-facing iPMTs mounted on its floor and ceiling. [150]

Appendix A

Absorption and Emission Spectra of Scintillator Constituents

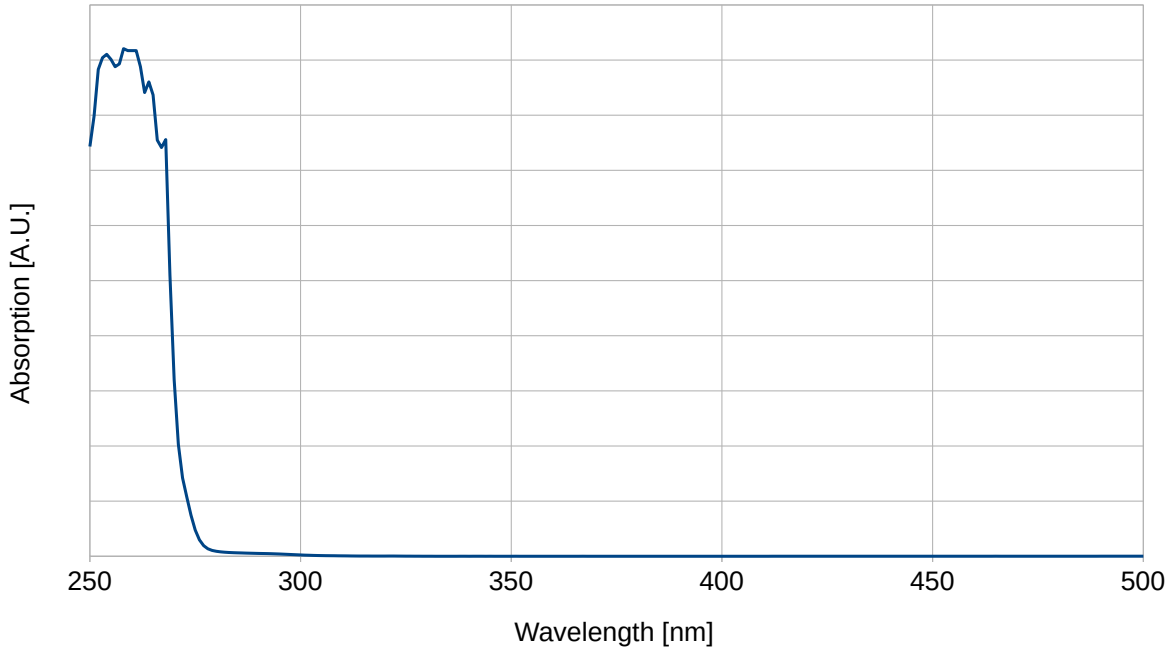

Figure A.1: Absorption spectrum of Linear Alkyl Benzene (LAB) diluted in Heptane. Maximum at 260 nm.

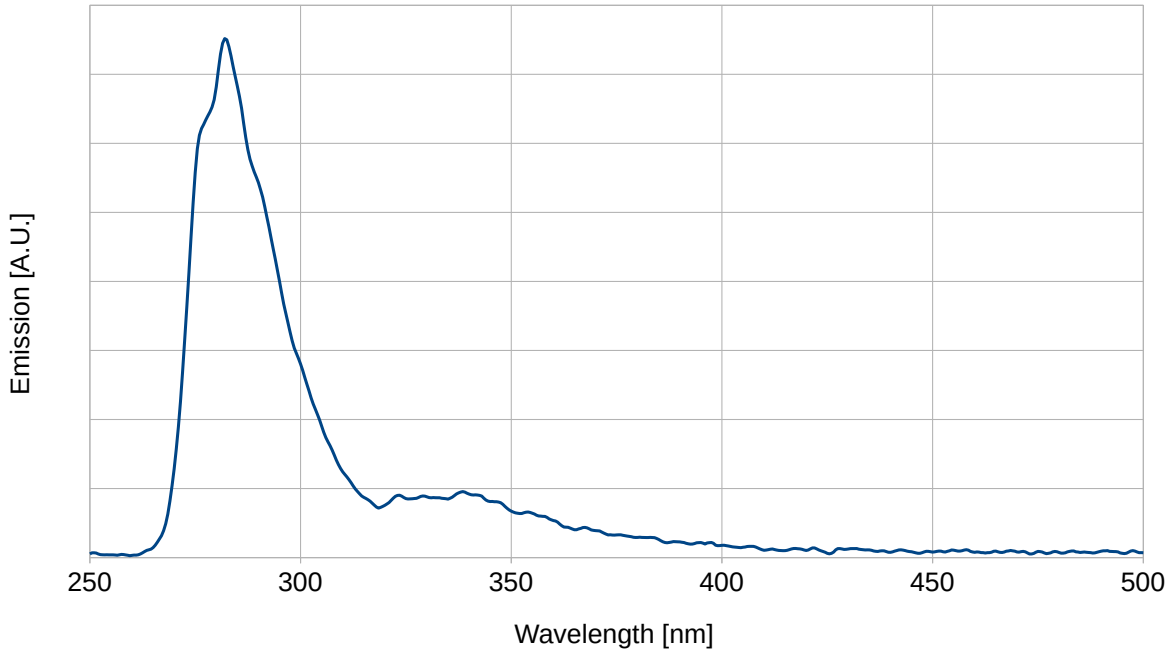

Figure A.2: Emission spectrum of Linear Alkyl Benzene (LAB) diluted in Heptane. Maximum at 282 nm.

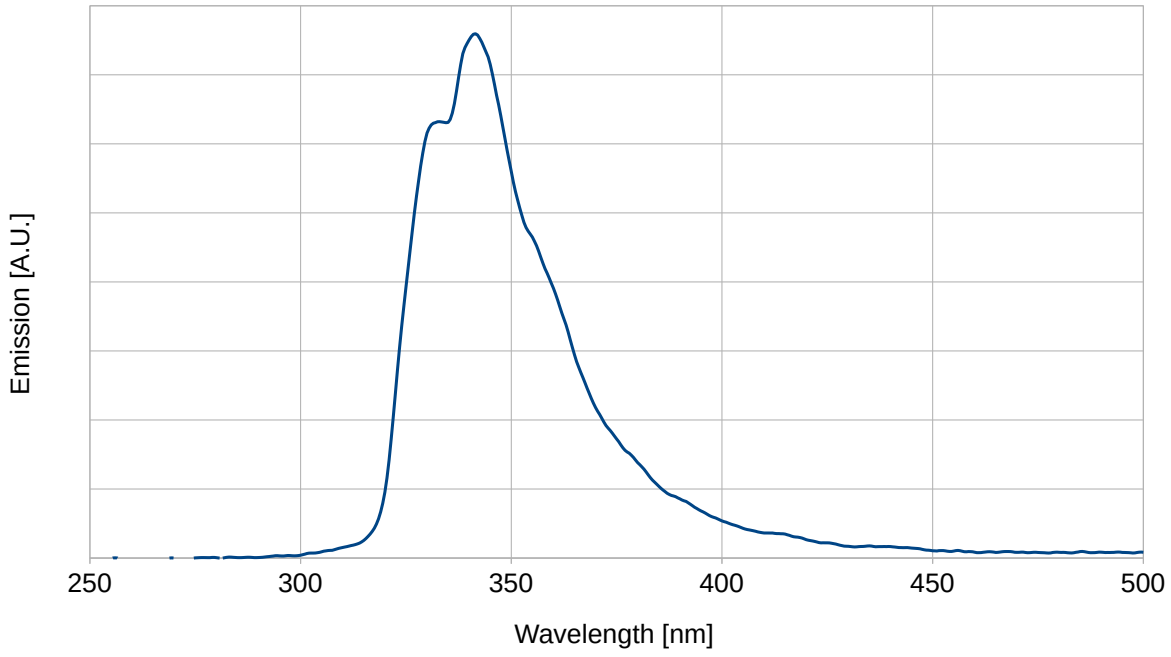

Figure A.3: Emission spectrum of pure Linear Alkyl Benzene (LAB) with self-absorption. Maximum shifted to 341 nm.

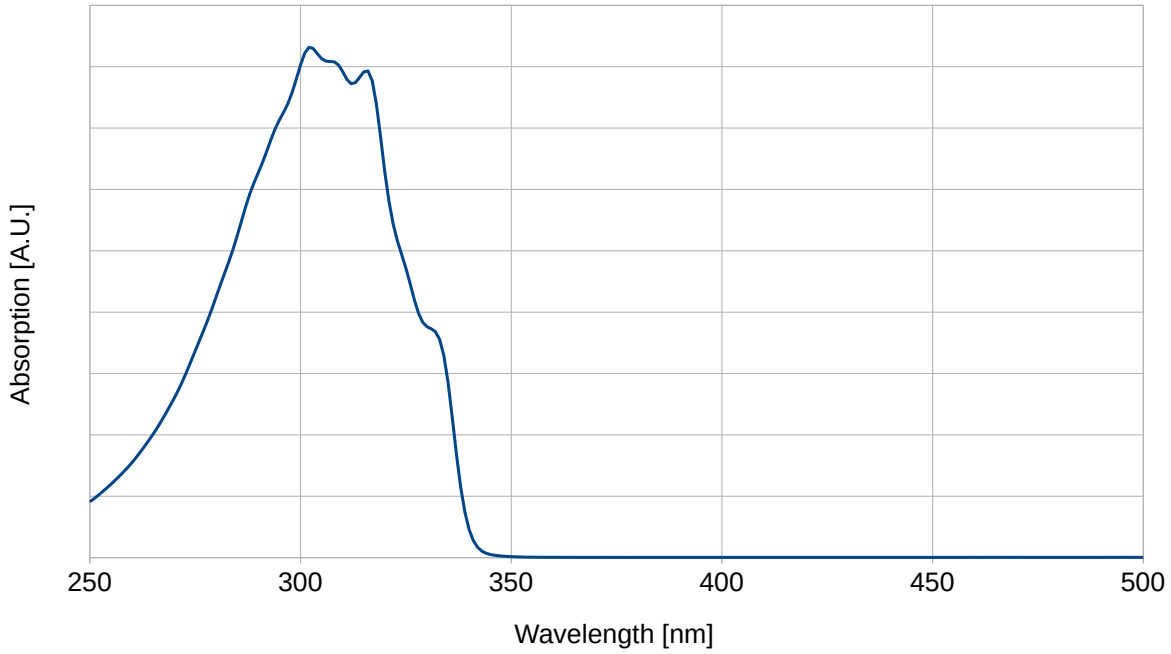

Figure A.4: Absorption spectrum of 2,5-Diphenyloxazole (PPO) diluted in Heptane. Maximum at 302 nm.

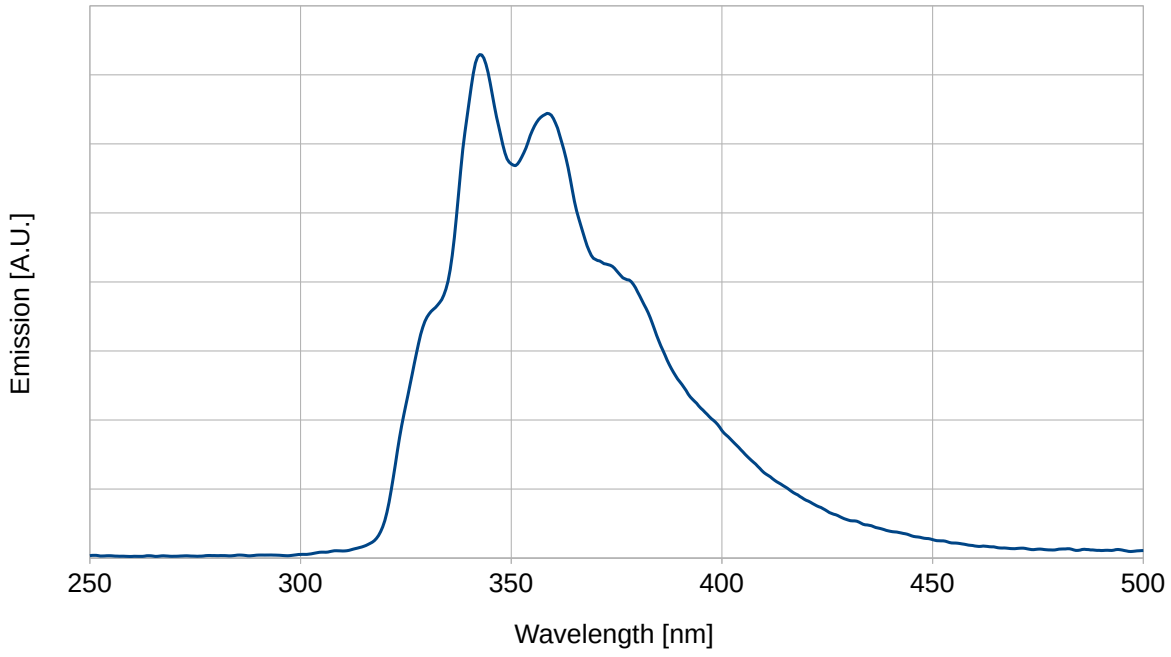

Figure A.5: Emission spectrum of 2,5-Diphenyloxazole (PPO) solved in LAB with a low concentration to avoid self-absorption. Maximum at 343 nm.

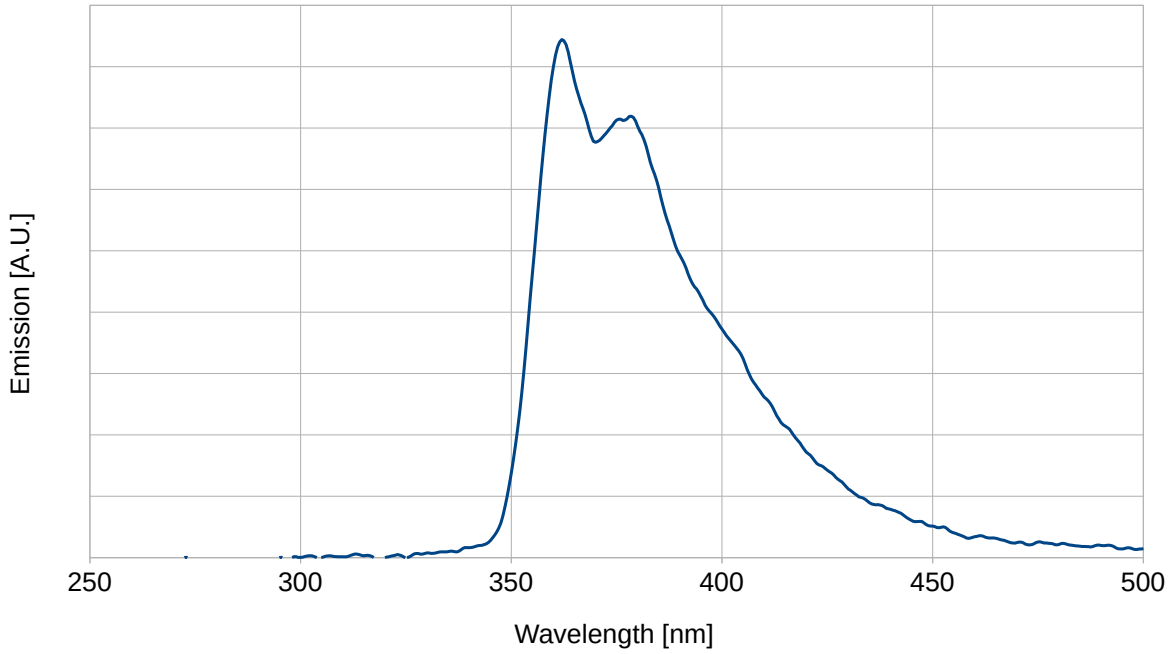

Figure A.6: Emission spectrum of 2,5-Diphenyloxazole (PPO) solved in LAB in a high enough concentration to allow self-absorption. Maximum shifted to 362 nm.

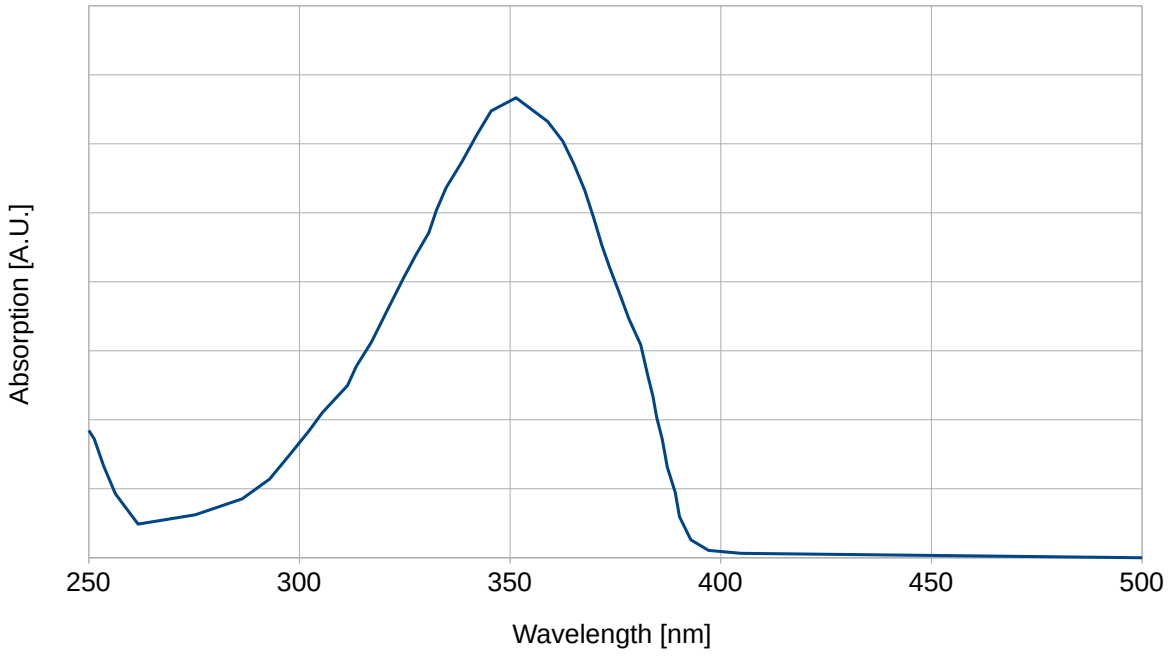

Figure A.7: Absorption spectrum of 1,4-bis(2-Methylstyryl)Benzene (bis-MSB). Maximum at 351 nm. [151]

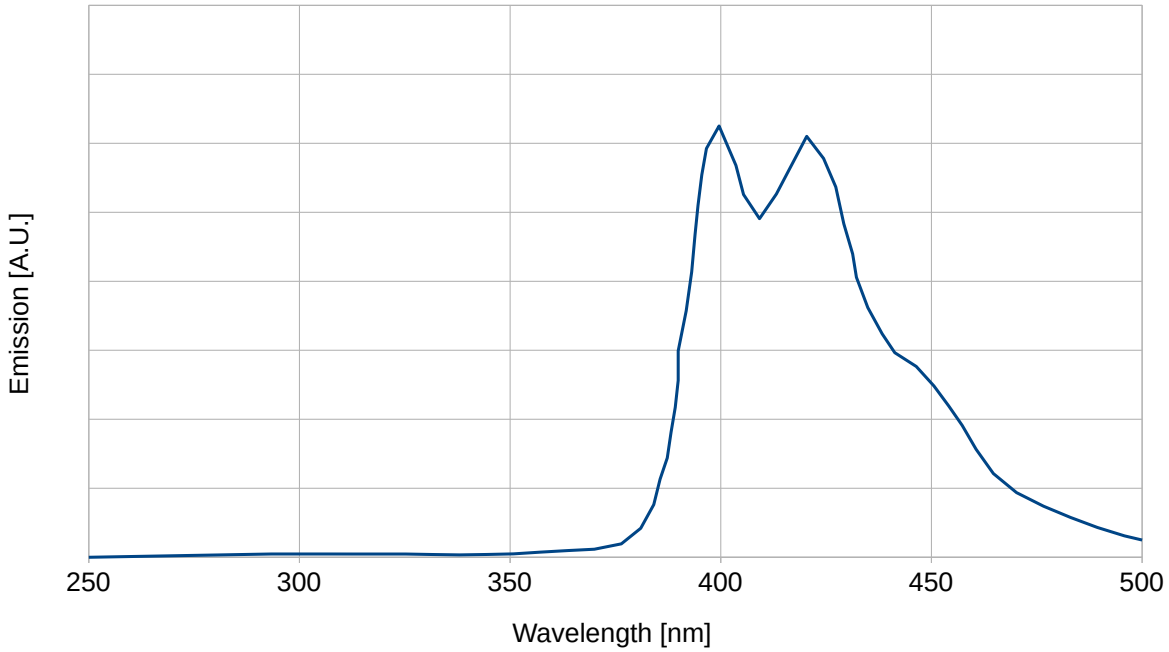

Figure A.8: Emission spectrum of 1,4-bis(2-Methylstyryl)Benzene (bis-MSB). Maxima at 400 nm and 420 nm. [151]

Appendix B

Rayleigh Scattering Length Data & Results

c [m^{-3}]	$5.80 \cdot 10^{16}$	$2.90 \cdot 10^{16}$	$1.45 \cdot 10^{16}$	$7.25 \cdot 10^{15}$	$3.63 \cdot 10^{15}$
$I^{\perp}_{\mathrm{Beam}}$ [#]	145655	143994	146982	148727	174146
$I^{\perp}_{\mathrm{Scat}}$ [#]	17333	8335	5307	2528	1665
$I^{\parallel}_{\mathrm{Beam}}$ [#]	145050	144091	146823	148988	173878
$I^{\parallel}_{\mathrm{Scat}}$ [#]	599	504	493	453	459
Λ_{Ray} [mm]	521.552	1094.482	1809.854	4242.612	8524.120
$(\Delta\Lambda_{\mathrm{Ray}})_{\mathrm{stat}}$ [mm]	3.466	11.285	25.600	108.871	341.284
$(\Delta\Lambda_{\mathrm{Ray}})_{\mathrm{sys}}$ [mm]	46.564	98.101	162.453	381.299	766.457

Table B.1: Single photon counts and resulting Rayleigh scattering lengths for the concentration scan of the colloid samples at 430 nm. The number of photons detected while investigating the horizontal polarization was interpreted as background events and subtracted from the vertical polarization.

λ [nm]	400	415	430	450	470
$I^{\perp}_{\mathrm{Beam}}$ [#]	40962	101268	178427	355508	577329
$I^{\perp}_{\mathrm{Scat}}$ [#]	22969	23666	22910	21480	20129
$I^{\parallel}_{\mathrm{Beam}}$ [#]	38973	98848	173912	348843	572828
$I^{\parallel}_{\mathrm{Scat}}$ [#]	1036	1039	1008	1031	1071
Λ_{Ray} [mm]	329.183	400.703	477.546	558.539	823.825
$(\Delta\Lambda_{\mathrm{Ray}})_{\mathrm{stat}}$ [mm]	7.779	13.331	21.455	37.686	76.165
$(\Delta\Lambda_{\mathrm{Ray}})_{\mathrm{sys}}$ [mm]	29.266	35.696	42.606	49.888	73.742

Table B.2: Single photon counts and resulting Rayleigh scattering lengths for the wavelength scan of the $c = 5.80{\cdot}10^{16}$ m^{-3} colloid sample. The number of photons detected while investigating the horizontal polarization was interpreted as background events and subtracted from the vertical polarization.

λ [nm]	400	430	450	470
$I^{\perp}_{\text{Beam}}$ [#]	82711	287124	582347	767815
$I^{\perp}_{\text{Scat}}$ [#]	1182	1154	1139	1114
$I^{\parallel}_{\text{Beam}}$ [#]	83271	286395	577490	763412
$I^{\parallel}_{\text{Scat}}$ [#]	740	791	815	824
Λ_{Ray} [m]	33.851	46.629	57.672	71.582
$(\Delta\Lambda_{\text{Ray}})_{\text{stat}}$ [m]	4.091	7.016	9.820	13.642
$(\Delta\Lambda_{\text{Ray}})_{\text{sys}}$ [m]	3.487	4.802	5.939	7.371

Table B.3: Single photon counts and resulting Rayleigh scattering lengths for the wavelength scan of the Cyclohexane sample. The number of photons detected while investigating the horizontal polarization was interpreted as background events and subtracted from the vertical polarization.

λ [nm]	400	415	430	450	470
$I^{\perp}_{\text{Beam}}$ [#]	299834	2176327	7094057	18133265	25795398
$I^{\perp}_{\text{Scat}}$ [#]	5344	13417	26057	32850	34256
$I^{\parallel}_{\text{Beam}}$ [#]	302105	1857637	7023546	18532829	26225955
$I^{\parallel}_{\text{Scat}}$ [#]	3398	8515	14997	19637	21144
I_{BG} [#]	1971	6586	13791	18504	19501
Λ_{Ray} [m]	10.158	18.116	26.085	32.033	36.387
$(\Delta\Lambda_{\text{Ray}})_{\text{stat}}$ [m]	0.477	0.824	1.232	1.535	1.639
$(\Delta\Lambda_{\text{Ray}})_{\text{sys}}$ [m]	0.921	1.694	2.582	3.194	3.584
δ_{depol}	0.59	0.44	0.18	0.15	0.20

Table B.4: Single photon counts and resulting Rayleigh scattering lengths for the Wavelength scan of the Nan Wan LAB sample. As the horizontal polarization does contribute to the scattering length, a dedicated background measurement with Cyclohexane was conducted.

λ [nm]	400	415	430	450	470
$I^{\perp}_{\text{Beam}}$ [#]	193130	505442	849499	3627625	12251617
$I^{\perp}_{\text{Scat}}$ [#]	2361	2811	2876	6000	15787
$I^{\parallel}_{\text{Beam}}$ [#]	192708	508377	857502	3590677	12156252
$I^{\parallel}_{\text{Scat}}$ [#]	1535	1490	1547	3818	10292
I_{BG} [#]	1074	1158	1246	3522	9157
Λ_{Ray} [m]	17.687	19.772	22.443	35.536	36.548
$(\Delta\Lambda_{\text{Ray}})_{\text{stat}}$ [m]	0.538	0.603	0.728	1.323	0.755
$(\Delta\Lambda_{\text{Ray}})_{\text{sys}}$ [m]	1.625	1.891	2.157	3.490	3.527
δ_{depol}	0.53	0.33	0.31	0.21	0.29

Table B.5: Single photon counts and resulting Rayleigh scattering lengths for the wavelength scan of the SHiP scintillator sample. As the horizontal polarization does contribute to the scattering length, a dedicated background measurement with Cyclohexane was conducted. [134]

Appendix C

Evolution of the OSIRIS Logo

Figure C.1: First sketch for an OSIRIS Logo.
2017-01-24

Figure C.2: First version of the OSIRIS Logo.
2017-02-15

Figure C.3: Attempt at updating the resolution of the OSIRIS Logo.
2018-02-20

Figure C.4: Color-corrected variant of the update, more reminiscent of the original design.
2018-02-22

Bibliography

[1] J. Chadwick. *Intensitätsverteilung im magnetischen Spectrum der β-Strahlen von radium B + C.* Verhandl. Dtsc. Phys. Ges. **16**, 383–391 (1914)

[2] A. de Gouvea. *TASI Lectures on Neutrino Physics* (2004). `arXiv:hep-ph/0411274`

[3] R. H. Stuewer. *The Nuclear Electron Hypothesis*, (pp. 19–67), (Springer Netherlands, Dordrecht, 1983). doi:10.1007/978-94-009-7133-2_2

[4] W. Pauli. *Collected Scientific Papers*, (Interscience, New York, 1964)

[5] C. Sutton. *Spaceship Neutrino*, (Cambridge University Press, 1992)

[6] J. Chadwick. *Possible Existence of a Neutron.* Nature **129**, 312 (1932). doi:10.1038/129312a0

[7] J. Chadwick. *The Existence of a Neutron.* Proceedings of the Royal Society of London A: Mathematical, Physical and Engineering Sciences **136**(830), 692–708 (1932). doi:10.1098/rspa.1932.0112

[8] J. Chadwick. *Bakerian Lecture – The Neutron.* Proceedings of the Royal Society of London A: Mathematical, Physical and Engineering Sciences **142**(846), 1–25 (1933). doi:10.1098/rspa.1933.0152

[9] C. L. Cowan, *et al. Detection of the Free Neutrino: a Confirmation.* Science **124**(3212), 103–104 (1956). doi:10.1126/science.124.3212.103

[10] G. Danby, *et al. Observation of High-Energy Neutrino Reactions and the Existence of Two Kinds of Neutrinos.* Phys. Rev. Lett. **9**, 36–44 (1962). doi:10.1103/PhysRevLett.9.36

[11] K. Kodama, *et al. Observation of tau neutrino interactions.* Physics Letters B **504**(3), 218 – 224 (2001). doi:10.1016/S0370-2693(01)00307-0

[12] B. T. Cleveland, *et al. Measurement of the Solar Electron Neutrino Flux with the Homestake Chlorine Detector.* The Astrophysical Journal **496**(1), 505 (1998)

[13] E. Kearns. *Experimental measurements of atmospheric neutrinos.* Nuclear Physics B - Proceedings Supplements **70**(1), 315 – 323 (1999). doi:10.1016/S0920-5632(98)00441-1. Proceedings of the Fifth International Workshop on topics in Astroparticle and Underground Physics

[14] The Super-Kamiokande Collaboration. *Evidence for Oscillation of Atmospheric Neutrinos.* Phys. Rev. Lett. **81**, 1562–1567 (1998). doi:10.1103/PhysRevLett.81.1562

[15] The SNO Collaboration. *Measurement of the Rate of $\nu_e + d \rightarrow p + p + e^-$ Interactions Produced by ^8B Solar Neutrinos at the Sudbury Neutrino Observatory.* Phys. Rev. Lett. **87**, 071301 (2001). doi:10.1103/PhysRevLett.87.071301

[16] The KamLAND Collaboration. *Measurement of Neutrino Oscillation with KamLAND: Evidence of Spectral Distortion.* Phys. Rev. Lett. **94**, 081801 (2005). doi:10.1103/PhysRevLett.94.081801

[17] A. Y. Smirnov. *Solar neutrinos: Oscillations or No-oscillations?* (2017). `arXiv:1609.02386 [hep-ph]`

[18] The Borexino Collaboration. *First real time detection of Be7 solar neutrinos by Borexino* (2007). `arXiv:0708.2251 [astro-ph]`

[19] The Borexino Collaboration. *First evidence of pep solar neutrinos by direct detection in Borexino* (2007). `arXiv:1110.3230 [hep-ph]`

[20] K. Sato, H. Suzuki. *Analysis of neutrino burst from the supernova 1987A in the Large Magellanic Cloud.* Phys. Rev. Lett. **58**, 2722–2725 (1987). doi:10.1103/PhysRevLett.58.2722

[21] I. Bartos, M. Kowalski. *Multimessenger Astronomy.* 2399-2891, (IOP Publishing, 2017). doi:10.1088/978-0-7503-1369-8

[22] A. de Gouvêa. *Neutrino Mass Models.* Annual Review of Nuclear and Particle Science **66**(1), 197–217 (2016). doi:10.1146/annurev-nucl-102115-044600

[23] Z.-Z. Xing, S. Zhou. *Neutrinos in Particle Physics, Astronomy and Cosmology*, (Springer, 2011)

[24] F. Couchot, *et al. Cosmological constraints on the neutrino mass including systematic uncertainties.* Astron. Astrophys. **606**, A104 (2017). doi:10.1051/0004-6361/201730927. `arXiv:1703.10829 [astro-ph]`

[25] V. N. Aseev, *et al. Upper limit on the electron antineutrino mass from the Troitsk experiment.* Phys. Rev. D **84**, 112003 (2011). doi:10.1103/PhysRevD.84.112003

[26] C. Patrignani, *et al. Review of Particle Physics.* Chin. Phys. **C40**(10), 100001 (2016). doi:10.1088/1674-1137/40/10/100001

[27] H. E. Logan. *TASI 2013 lectures on Higgs physics within and beyond the Standard Model* (2013). `arXiv:1406.1786 [hep-ph]`

[28] S. Weinberg. *Baryon- and Lepton-Nonconserving Processes.* Phys. Rev. Lett. **43**, 1566–1570 (1979). doi:10.1103/PhysRevLett.43.1566

[29] K. Babu. *Model of "calculable" Majorana neutrino masses.* Physics Letters B **203**(1), 132 – 136 (1988). doi:10.1016/0370-2693(88)91584-5

[30] E. Ma. *Verifiable radiative seesaw mechanism of neutrino mass and dark matter.* Phys. Rev. D **73**, 077301 (2006). doi:10.1103/PhysRevD.73.077301

[31] B. Pontecorvo. *Inverse beta processes and nonconservation of lepton charge.* Sov. Phys. JETP **7**, 172–173 (1958). [Zh. Eksp. Teor. Fiz.34,247(1957)]

[32] Z. Maki, *et al. Remarks on the Unified Model of Elementary Particles.* Progress of Theoretical Physics **28**(5), 870–880 (1962). doi:10.1143/PTP.28.870

[33] B. Kayser. *Neutrino Oscillation Phenomenology* (2008). `arXiv:0804.1121 [hep-ph]`

[34] S. Antusch, *et al. Unitarity of the leptonic mixing matrix.* Journal of High Energy Physics **2006**(10), 084 (2006)

[35] J. Heeck. *Seesaw parametrization for n right-handed neutrinos.* Phys. Rev. D **86**, 093023 (2012). doi:10.1103/PhysRevD.86.093023

[36] J. Schechter, J. W. F. Valle. *Neutrinoless double-β decay in SU(2)$\times$U(1) theories.* Phys. Rev. D **25**, 2951–2954 (1982). doi:10.1103/PhysRevD.25.2951

[37] C. Arnaboldi, *et al. CUORE: a cryogenic underground observatory for rare events.* Nuclear Instruments and Methods in Physics Research Section A: Accelerators, Spectrometers, Detectors and Associated Equipment **518**(3), 775 – 798 (2004). doi:10.1016/j.nima.2003.07.067

[38] K.-H. Ackermann, *et al. The Gerda experiment for the search of $0\nu\beta\beta$ decay in 76Ge.* The European Physical Journal C **73**(3), 2330 (2013). doi:10.1140/epjc/s10052-013-2330-0

[39] D. G. Phillips II, *et al. The MAJORANA experiment: an ultra-low background search for neutrinoless double-beta decay.* Journal of Physics: Conference Series **381**(1), 012044 (2012)

[40] C. Giunti, C. W. Kim. *Fundamentals of Neutrino Physics and Astrophysics*, (Oxford, UK: Univ. Pr. (2007) 710 p2007)

[41] B. Kayser. *On the quantum mechanics of neutrino oscillation.* Phys. Rev. D **24**, 110–116 (1981). doi:10.1103/PhysRevD.24.110

[42] S. Mikheyev, A. Smirnov. *Resonant neutrino oscillations in matter.* Progress in Particle and Nuclear Physics **23**, 41 – 136 (1989). doi:10.1016/0146-6410(89)90008-2

[43] S. P. Mikheyev, A. Y. Smirnov. *Resonant amplification of ν oscillations in matter and solar-neutrino spectroscopy.* Il Nuovo Cimento C **9**(1), 17–26 (1986). doi:10.1007/BF02508049

[44] H. A. Bethe. *Possible Explanation of the Solar Neutrino Puzzle.* Phys. Rev. Lett. **56**, 1305–1308 (1986). doi:10.1103/PhysRevLett.56.1305

[45] M. Maltoni, A. Yu. Smirnov. *Solar neutrinos and neutrino physics.* The European Physical Journal A **52**(4), 87 (2016). doi:10.1140/epja/i2016-16087-0

[46] M. Agostini, *et al. Discovery probability of next-generation neutrinoless double-β decay experiments.* Phys. Rev. D **96**, 053001 (2017). doi:10.1103/PhysRevD.96.053001

[47] K. Abazajian, *et al. Neutrino physics from the cosmic microwave background and large scale structure.* Astroparticle Physics **63**, 66 – 80 (2015). doi:10.1016/j.astropartphys.2014.05.014. Dark Energy and CMB

[48] T. Nakaya, R. K. Plunkett. *Neutrino oscillations with the MINOS, MINOS+, T2K, and NOvA experiments.* New Journal of Physics **18**(1), 015009 (2016)

[49] S. King. *Unified models of neutrinos, flavour and CP Violation.* Progress in Particle and Nuclear Physics **94**, 217 – 256 (2017). doi:10.1016/j.ppnp.2017.01.003

[50] The T2K Collaboration. *Measurement of neutrino and antineutrino oscillations by the T2K experiment including a new additional sample of ν_e interactions at the far detector.* Phys. Rev. D **96**, 092006 (2017). doi:10.1103/PhysRevD.96.092006

[51] The NOvA Collaboration. *Constraints on Oscillation Parameters from ν_e Appearance and ν_μ Disappearance in NOvA.* Phys. Rev. Lett. **118**, 231801 (2017). doi:10.1103/PhysRevLett.118.231801

[52] The DUNE Collaboration. *Long-Baseline Neutrino Facility (LBNF) and Deep Underground Neutrino Experiment (DUNE) Conceptual Design Report Volume 1: The LBNF and DUNE Projects* (2016). `arXiv:1601.05471`

[53] The DUNE Collaboration. *Long-Baseline Neutrino Facility (LBNF) and Deep Underground Neutrino Experiment (DUNE) Conceptual Design Report Volume 2: The Physics Program for DUNE at LBNF* (2015). `arXiv:1512.06148`

[54] The IceCube-PINGU Collaboration. *Letter of Intent: The Precision IceCube Next Generation Upgrade (PINGU)* (2014). `arXiv:1401.2046`

[55] S. Adrián-Martínez, *et al. Letter of intent for KM3NeT 2.0.* Journal of Physics G: Nuclear and Particle Physics **43**(8), 084001 (2016)

[56] K. Abe, *et al. Letter of Intent: The Hyper-Kamiokande Experiment — Detector Design and Physics Potential —* (2011). `arXiv:1109.3262`

[57] *Precision electroweak measurements on the Z resonance.* Physics Reports **427**(5), 257 – 454 (2006). doi:10.1016/j.physrep.2005.12.006

[58] The LSND Collaboration. *Evidence for neutrino oscillations from the observation of $\overline{\nu}_e$ appearance in a $\overline{\nu}_\mu$ beam.* Phys. Rev. D **64**, 112007 (2001). doi:10.1103/PhysRevD.64.112007

[59] The MiniBooNE Collaboration. *Improved Search for $\overline{\nu}_\mu \to \overline{\nu}_e$ Oscillations in the MiniBooNE Experiment.* Phys. Rev. Lett. **110**, 161801 (2013). doi:10.1103/PhysRevLett.110.161801

[60] P. Adamson, *et al. Search for sterile neutrinos in MINOS and MINOS+ using a two-detector fit* (2017). `arXiv:1710.06488`

[61] The IceCube Collaboration. *Searches for Sterile Neutrinos with the IceCube Detector*. Phys. Rev. Lett. **117**, 071801 (2016). doi:10.1103/PhysRevLett.117.071801

[62] C. Giunti, M. Laveder. *Statistical significance of the gallium anomaly*. Phys. Rev. C **83**, 065504 (2011). doi:10.1103/PhysRevC.83.065504

[63] B. Achkar, *et al. Search for neutrino oscillations at 15, 40 and 95 meters from a nuclear power reactor at Bugey*. Nuclear Physics B **434**(3), 503 – 532 (1995). doi:10.1016/0550-3213(94)00513-E

[64] G. Zacek, *et al. Neutrino-oscillation experiments at the Gösgen nuclear power reactor*. Phys. Rev. D **34**, 2621–2636 (1986). doi:10.1103/PhysRevD.34.2621

[65] Y. Kozlov, *et al. Today and future neutrino experiments at Krasnoyarsk nuclear reactor*. Nuclear Physics B - Proceedings Supplements **87**(1), 514 – 516 (2000). doi:10.1016/S0920-5632(00)00738-6. Proceedings of the Sixth International Workshop on Topics in Astroparticle and Underground Physics

[66] A. Kuvshinnikov, *et al. Measuring the $\bar{\nu}_e + p \to n + e^+$ cross-section and beta decay axial constant in a new experiment at Rovno NPP reactor*. JETP Lett. **54**(5), 253 – 257 (1991)

[67] Z. D. Greenwood, *et al. Results of a two-position reactor neutrino-oscillation experiment*. Phys. Rev. D **53**, 6054–6064 (1996). doi:10.1103/PhysRevD.53.6054

[68] K. N. Abazajian, *et al. Light Sterile Neutrinos: A White Paper* (2012). `arXiv:1204.5379`

[69] The Daya Bay Collaboration. *Improved Search for a Light Sterile Neutrino with the Full Configuration of the Daya Bay Experiment*. Phys. Rev. Lett. **117**, 151802 (2016). doi:10.1103/PhysRevLett.117.151802

[70] The Daya Bay Collaboration. *Evolution of the Reactor Antineutrino Flux and Spectrum at Daya Bay*. Phys. Rev. Lett. **118**, 251801 (2017). doi:10.1103/PhysRevLett.118.251801

[71] The NEOS Collaboration. *Sterile Neutrino Search at the NEOS Experiment*. Phys. Rev. Lett. **118**, 121802 (2017). doi:10.1103/PhysRevLett.118.121802

[72] I. Alekseev, *et al. Search for sterile neutrinos at the DANSS experiment* (2018). `arXiv:1804.04046`

[73] I. Esteban, *et al. The fate of hints: updated global analysis of three-flavor neutrino oscillations*. Journal of High Energy Physics **2020**(9), 178 (2020). doi:10.1007/JHEP09(2020)178. `arXiv:2007.14792`

[74] T. Adam, *et al. JUNO Conceptual Design Report* (2015). `arXiv:1508.07166`

[75] F. An, *et al. Neutrino physics with JUNO*. Journal of Physics G: Nuclear and Particle Physics **43**(3), 030401 (2016)

[76] T. Adam, *et al. The OPERA experiment Target Tracker*. Nuclear Instruments and Methods in Physics Research Section A: Accelerators, Spectrometers, Detectors and Associated Equipment **577**(3), 523 – 539 (2007). doi:10.1016/j.nima.2007.04.147

[77] The Double Chooz Collaboration. *Reactor $\overline{\nu}_e$ disappearance in the Double Chooz experiment*. Phys. Rev. D **86**, 052008 (2012). doi:10.1103/PhysRevD.86.052008

[78] D. W. McKee, *et al. A ^{13}C$(\alpha, n)^{16}$O calibration source for KamLAND*. Nuclear Instruments and Methods in Physics Research Section A: Accelerators, Spectrometers, Detectors and Associated Equipment **587**(2), 272 – 276 (2008). doi:10.1016/j.nima.2007.12.002

[79] R. Diehl, *et al. Radioactive ^{26}Al from massive stars in the galaxy*. Nature **439**, 45 EP – (2006). doi:10.1038/nature04364

[80] M. Wurm, *et al. The next-generation liquid-scintillator neutrino observatory LENA*. Astroparticle Physics **35**(11), 685 – 732 (2012). doi:10.1016/j.astropartphys.2012.02.011

[81] P. A. Karam. *Gamma and neutrino radiation dose from gamma ray bursts and nearby supernovae*. Health Physics **82**(4) (2002)

[82] K. Bays, *et al. Supernova relic neutrino search at Super-Kamiokande*. Phys. Rev. D **85**, 052007 (2012). doi:10.1103/PhysRevD.85.052007

[83] R. Mitalas, K. R. Sills. *On the photon diffusion time scale for the Sun* **401** (1992)

[84] M. Fukugita, T. Yanagida. *Physics of Neutrinos: and Application to Astrophysics*. Theoretical and Mathematical Physics, (Springer Berlin Heidelberg2013)

[85] N. Vinyoles, *et al. A New Generation of Standard Solar Models*. The Astrophysical Journal **835**(2), 202 (2017)

[86] V. Takhistov, for the Super-Kamiokande Collaboration. *Review of Nucleon Decay Searches at Super-Kamiokande* (2016). `arXiv:1605.03235`

[87] W. Hampel, *et al. GALLEX solar neutrino observations: results for GALLEX IV*. Physics Letters B **447**(1), 127 – 133 (1999). doi:10.1016/S0370-2693(98)01579-2

[88] J. N. Abdurashitov, *et al. Measurement of the solar neutrino capture rate with gallium metal*. Phys. Rev. C **60**, 055801 (1999). doi:10.1103/PhysRevC.60.055801

[89] F. Halzen. *Astroparticle physics with high energy neutrinos: from AMANDA to IceCube*. The European Physical Journal C - Particles and Fields **46**(3), 669–687 (2006). doi:10.1140/epjc/s2006-02536-4

[90] K. S. Hirata, *et al. Observation in the Kamiokande-II detector of the neutrino burst from supernova SN1987A*. Phys. Rev. D **38**, 448–458 (1988). doi:10.1103/PhysRevD.38.448

[91] J. Boger, *et al. The Sudbury Neutrino Observatory.* Nuclear Instruments and Methods in Physics Research Section A: Accelerators, Spectrometers, Detectors and Associated Equipment **449**(1), 172 – 207 (2000). doi:10.1016/S0168-9002(99)01469-2

[92] G. Bellini, *et al. Final results of Borexino Phase-I on low-energy solar neutrino spectroscopy.* Phys. Rev. D **89**, 112007 (2014). doi:10.1103/PhysRevD.89.112007

[93] F. An, *et al. The detector system of the Daya Bay reactor neutrino experiment.* Nuclear Instruments and Methods in Physics Research Section A: Accelerators, Spectrometers, Detectors and Associated Equipment **811**, 133 – 161 (2016). doi:10.1016/j.nima.2015.11.144

[94] A. Gando, *et al.* ^{7}Be *solar neutrino measurement with KamLAND.* Phys. Rev. C **92**, 055808 (2015). doi:10.1103/PhysRevC.92.055808

[95] L. Aliaga, *et al. Design, calibration, and performance of the MINERvA detector.* Nuclear Instruments and Methods in Physics Research Section A: Accelerators, Spectrometers, Detectors and Associated Equipment **743**, 130 – 159 (2014). doi:10.1016/j.nima.2013.12.053

[96] R. Patterson. *The NOvA experiment: status and outlook.* Nuclear Physics B - Proceedings Supplements **235-236**, 151 – 157 (2013). doi:10.1016/j.nuclphysbps.2013.04.005. The XXV International Conference on Neutrino Physics and Astrophysics

[97] The RENO Collaboration. *RENO: An Experiment for Neutrino Oscillation Parameter θ_{13} Using Reactor Neutrinos at Yonggwang* (2010). `arXiv:1003.1391`

[98] K. P. C. Vollhardt and N. E. Schore. *Organic Chemistry*, (W.H. Freeman, 1994)

[99] W. Depnering. *Scintillation Light Transport in the Large Reactor Antineutrino Detector JUNO (Working Title).* PhD Thesis (Work in Progress). Johannes Gutenberg Universität Mainz

[100] A. Jabłoński. *Über den Mechanismus der Photolumineszenz von Farbstoffphosphoren.* Zeitschrift für Physik **94**(1-2), 38–46 (1935). doi:10.1007/BF01330795

[101] G. Knoll. *Radiation Detection and Measurement*, (John Wiley & Sons, 2010)

[102] M. Kasha. *Characterization of electronic transitions in complex molecules.* Discuss. Faraday Soc. **9**, 14–19 (1950). doi:10.1039/DF9500900014

[103] J. Birks. *The Theory and Practice of Scintillation Counting.* International series of monographs on electronics and instrumentation, (Pergamon Press, 1964)

[104] J. B. Birks. *Scintillation counters*, (McGraw-Hill, Pergamon Press, 1953)

[105] Wikipedia. *File: Franck-Condon-Prinzip.svg (edited).* `http://commons.wikimedia.org/wiki/File:Franck-Condon-Prinzip.svg` (August 12, 2007). Accessed: July 17, 2018

[106] T. Förster. *Zwischenmolekulare Energiewanderung und Fluoreszenz.* Annalen der Physik **437**(1-2), 55–75. doi:10.1002/andp.19484370105

[107] G. Herzberg and K. P. Huber. *Molecular spectra and molecular structure I.* v. 4, (Van Nostrand, 1979)

[108] E. U. Condon. *Nuclear Motions Associated with Electron Transitions in Diatomic Molecules.* Phys. Rev. **32**, 858–872 (1928). doi:10.1103/PhysRev.32.858

[109] European Chemicals Agency (ECHA). *Benzene, C10-13-alkyl derivs.* `https://echa.europa.eu/registration-dossier/-/registered-dossier/15763` (June 26, 2018). Accessed: July 24, 2018

[110] SigmaAldritch. *Material Safety Data Sheet 2,5-Diphenyloxazol.* `http://www.sigmaaldrich.com/catalog/product/aldrich/d210404` (July 05, 2012). Accessed: July 24, 2018

[111] SigmaAldritch. *Material Safety Data Sheet 1,4-Bis(2-methylstyryl)benzene.* `http://www.sigmaaldrich.com/catalog/product/sigma/m7127` (July 09, 2012). Accessed: July 24, 2018

[112] SigmaAldritch. *Material Safety Data Sheet Cyclohexane.* `https://www.sigmaaldrich.com/catalog/product/sial/227048` (June 11, 2018). Accessed: August 17, 2018

[113] L. W. Pickett, *et al. Vacuum Ultraviolet Absorption Spectra of Cyclic Compounds. I. Cyclohexane, Cyclohexene, Cyclopentane, Cyclopentene and Benzene.* Journal of the American Chemical Society **73**(10), 4862–4865 (1951)

[114] F. Hirayama, S. Lipsky. *Fluorescene of Saturated Hydrocarbons.* The Journal of Chemical Physics **51**, 3616–3617 (1969)

[115] The Borexino Collaboration. *Light propagation in a large volume liquid scintillator.* Nuclear Instruments and Methods in Physics Research Section A: Accelerators, Spectrometers, Detectors and Associated Equipment **440**(2,), 360 – 371 (2000)

[116] H.-L. Xiao, *et al. Study of absorption and re-emission processes in a ternary liquid scintillation system.* Chinese Physics C **34**(11), 1724–1728 (2010). doi:10.1088/1674-1137/34/11/011

[117] S. Qian. Published at ICHEP 2018 Seoul, `http://www.ichep2018.org/` (Personal Communication, October 25, 2018)

[118] A. T. Young. *Rayleigh scattering.* Physics Today **35**, 42 (1982)

[119] M. Bass, Optical Society of America. *Handbook of Optics: Fundamentals, techniques, and design.* No. v. 1 in Handbook of Optics, (McGraw-Hill, 1994)

[120] X. Zhou, *et al. Rayleigh scattering of linear alkylbenzene in large liquid scintillator detectors.* Review of Scientific Instruments **86**(7), 073310 (2015). doi:10.1063/1.4927458

[121] M. Kerker, E. Loebl. *The Scattering of Light and Other Electromagnetic Radiation: Physical Chemistry: A Series of Monographs*. Physical chemistry, (Elsevier Science, 2013)

[122] Cabannes, Jean. *Sur la diffusion de la lumière par les molécules des gaz transparents*. Ann. Phys. **9**(15), 5–150 (1921). doi:10.1051/anphys/192109150005

[123] L. V. King, A. S. Eve. *On the complex anisotropic molecule in relation to the dispersion and scattering of light*. Proceedings of the Royal Society of London. Series A, Containing Papers of a Mathematical and Physical Character **104**(726), 333–357 (1923). doi:10.1098/rspa.1923.0113

[124] G. D. Parfitt, J. A. Wood. *Rayleigh ratios of pure liquids; comparison of experiment with theory*. Trans. Faraday Soc. **64**, 805–814 (1968). doi:10.1039/TF9686400805

[125] Hamamatsu. *R9980 Photomultiplier Tube Data Sheet*. `https://www.hamamatsu.com/jp/en/product/type/R9980/index.html` (January 2014). Accessed: May 8, 2019

[126] Oriel Instruments. *APEX2 User's Manual*. `https://www.newport.com/medias/sys_master/images/images/hf4/h80/9367225303070/90077348D-MAPEX2-APEX2-MANUAL.pdf` (2015). Accessed: May 8, 2019

[127] Hamamatsu. *Photomultiplier Tubes - Basics and Applications, Third Edition (Edition 3a)*. `https://www.hamamatsu.com/resources/pdf/etd/PMT_handbook_v3aE.pdf` (2007). Accessed: May 8, 2019

[128] J. P. Harrington. *Scattering of Radiation with Polarization*. `https://www.astro.umd.edu/~jph/notes3.pdf`. Accessed: August 9, 2020

[129] Q. Liu, *et al. Rayleigh scattering and depolarization ratio in linear alkylbenzene*. Nuclear Instruments and Methods in Physics Research Section A: Accelerators, Spectrometers, Detectors and Associated Equipment **795**, 284 – 287 (2015). doi:10.1016/j.nima.2015.05.032

[130] J. Wenzl. *Strukturuntersuchung in Kolloidalen Fluiden*. Diploma Thesis (2010). Johannes Gutenberg Universität Mainz

[131] M. Wurm, *et al. Optical scattering lengths in large liquid-scintillator neutrino detectors*. Review of Scientific Instruments **81**(5), 053301 (2010). doi:10.1063/1.3397322. `arXiv:1004.0811`

[132] The SHiP Collaboration. *A facility to Search for Hidden Particles (SHiP) at the CERN SPS* (2015). `arXiv:1504.04956`

[133] M. Ehlert, *et al. Proof-of-principle measurements with a liquid-scintillator detector using wavelength-shifting optical modules*. Journal of Instrumentation **14**(03), P03021–P03021 (2019). doi:10.1088/1748-0221/14/03/p03021. `arXiv:1812.06460`

[134] A. Kujawa. *Data taken and provided by* (September 16, 2020)

[135] P. Hackspacher. *Studies of Light Quenching Effects in Liquid Scintillators and Parameter Determination of the Buffer and Veto Fluids of the Double Chooz Near Detector*. Master Thesis (2014). Technische Universität München

[136] S. S. Gokhale, *et al. A Spectrometric Approach to Characterize the Rayleigh Scattering Length for Ultrapure Liquid Scintillator Detectors* (2020). `arXiv:2008.08634`

[137] G. Ranucci, E. Meroni. *Counting test facility for the Borexino experiment*. International Journal of Modern Physics A **29**(16), 1442001 (2014). doi:10.1142/S0217751X14420019

[138] G. Alimonti, *et al. A large-scale low-background liquid scintillation detector: the counting test facility at Gran Sasso*. Nuclear Instruments and Methods in Physics Research Section A: Accelerators, Spectrometers, Detectors and Associated Equipment **406**(3), 411 – 426 (1998). doi:10.1016/S0168-9002(98)00018-7

[139] The Borexino Collaboration: G. Bellini, *et al. Lifetime measurements of 214Po and 212Po with the CTF liquid scintillator detector at LNGS* (2012). `arXiv:1212.1332`

[140] `Geant4` 9.6p4. *Software Download*. `https://geant4.web.cern.ch/node/1630` (January 30, 2015). Accessed: November 28, 2018

[141] `CERN root` 5.34/23. *Software Download*. `https://root.cern.ch/content/release-53423` (November 07, 2014). Accessed: November 28, 2018

[142] `Geant4` 10.2p3. *Software Download*. `https://geant4.web.cern.ch/node/1606` (January 27, 2017). Accessed: November 28, 2018

[143] Geant4 Cross Reference. *Novice Examples*. `http://www-geant4.kek.jp/lxr/source/examples/novice/?v=9.6.p4` (February 04, 2015). Accessed: November 21, 2018

[144] R. Möllenberg. *Monte Carlo Study of Solar* ^{8}B *Neutrinos and the Diffuse Supernova Neutrino Background in LENA*. PhD Thesis (2013). Technische Universität München

[145] N. D. S. International Atomic Energy Agency. *Live Chart of Nuclides*. `https://www-nds.iaea.org/relnsd/vcharthtml/VChartHTML.html` (October, 2019). Accessed: October 16, 2020

[146] P. Hackspacher, M. Wurm. *The OSIRIS Pre-Detector* (2017). Whitepaper, Internal JUNO Design Document

[147] W. L. Guo, *et al. Solar, supernova, atmospheric and geo neutrino studies using JUNO detector* (2016). `arXiv:1610.09508`

[148] H. T. J. Steiger. *Development of a low level radioactive liquid scintillator and of the detector monitoring system for the JUNO neutrino experiment*. PhD Thesis (2020). Technische Universität München

[149] O. Pilarczyk. *Development of a prototype for the OSIRIS detector*. Master Thesis (2020). Johannes Gutenberg Universität Mainz

[150] R. Othegraven. *Private communication* (October 19, 2020)

[151] Y. Zhang, *et al. A complete optical model for liquid-scintillator detectors.* Nuclear Instruments and Methods in Physics Research Section A: Accelerators, Spectrometers, Detectors and Associated Equipment **967**, 163860 (2020). doi: 10.1016/j.nima.2020.163860